

Charge Transfer and Chiral Imprinting on Nano Particles

by

Zhendian Zhang

Department of Chemistry
Duke University

Date: _____

Approved:

David N. Beratan, Supervisor

Michael J. Therien

Peng Zhang

Christine K. Payne

Dissertation submitted in partial fulfillment of
the requirements for the degree of Doctor
of Philosophy in the Department of
Chemistry in the Graduate School
of Duke University

2023

ABSTRACT

Charge Transfer and Chiral Imprinting on Nano Particles

by

Zhendian Zhang

Department of Chemistry
Duke University

Date: _____

Approved:

David N. Beratan, Supervisor

Michael J. Therien

Peng Zhang

Christine K. Payne

An abstract of a dissertation submitted in partial
fulfillment of the requirements for the degree
of Doctor of Philosophy in the Department of
Chemistry in the Graduate School of
Duke University

2023

Copyright by
Zhendian Zhang
2023

Abstract

Quantum dots (QDs), being semiconductor particles small enough to exhibit quantum mechanical properties, are leveraged in numerous applications including energy harvesting, quantum computing, and biomedical imaging. Our research theoretically examined two functional QD systems: (1) first one undergoes the electron transfer (ET) between CdSe QDs facilitated by a solvent and linker molecule, and (2) a second performs charge transfer (CT) and triplet energy transfer (TET) between CdSe/CdS core/shell QDs and ligand acceptor. These processes were scrutinized based on the electronic coupling tunneling through the shell, reaction free energy change, and reorganization energy. Furthermore, we explored chiral imprinting mechanism in perovskite nanoplatelet and the ET dynamics of organic molecules with pathway interferences.

We devised a discrete variable representation (DVR) method to simulate ET between CdSe QDs, mediated by a solvent and a linker molecule. Employing the effective mass approximation (EMA), we characterized the QDs, ligand, and solvent, studying the distance dependence of donor-acceptor coupling via the energy splitting method. We found that the ET coupling decreases exponentially with the interdot distance. The decay constant is dictated by the size of the linker and the tunneling barrier through the solvent and ligand. When the donor and acceptor sizes significantly

surpass the diameter of the linker, such as in large QDs with an alkane chain linker, the ET is predominantly regulated by through-solvent tunneling.

The DVR method was also applied to simulate the CdSe/CdS core/shell QD system. Notably, experiments observe a subtle TET rate decay with an increase in shell thickness. Simulating QDs of varying shell thickness, we found a large TET coupling decay constant. Marcus analysis finds that the QD TET operates in a deeply inverted regime, where an increase in shell thickness reduces the driving force, leading to a significant increase of the Franck-Condon factor. This in turn offsets the exponential decrease of the electronic coupling with shell thickness. Further, our findings demonstrated that variations in shell thickness could further decrease the TET rate decay constant.

Applying density functional theory (DFT) calculations and a charge-perturbed-particle-in-box model, we investigated chiral imprinting of perovskite nanoplatelet by chiral ligands. We found that the imprinted CD signal is sensitive to the orientation of the chiral ligand. As the proportion of chiral surface ligands grows, our model calculations find that the intensity of the CD signal from the lowest energy exciton transition saturates.

We also examined the effects of light polarization on the ET yield in the coherent limit, using a model Zinc porphyrin as the ET donor due to its near degenerate excited states and orthogonal transition dipole moments. These two donor excited states, coupling to the acceptor state, produce pathway interference that strongly impact the ET. Introducing dissipation due to system-environment interaction via the Lindblad equation, we found that the ET yield is influenced by the initial light polarization. In the DA system, linearly polarized light (LPL) is predicted to induce an ET yield difference of up to 85% with a 100 fs dephasing time, while the yield difference elicited by R-circularly polarized light (R-CPL) and L-circularly polarized light (L-CPL) was insignificant. The model Hamiltonian was subsequently simulated and the dynamics was predicted by our collaborators with a trapped ion qutrit system.

Dedication

Dedicated to my grandmother, who gave me selfless love, yet I didn't have the chance to reciprocate.

Contents

Abstract	iv
List of Tables	xi
List of Figures	xii
Acknowledgements	xiv
1. Introduction.....	1
1.1 Electron Transfer Theory	1
1.2 Nanoparticles	3
2. Size Determines the balance of Through-bond and Through-solvent Coupling Between Linked Quantum Dots	8
2.1 Introduction.....	8
2.2 Method	11
2.2.1 Model potential.....	11
2.2.2 Discrete variable representation (DVR) method.....	13
2.2.3 DA Interactions and energy splitting	15
2.3 Results and discussion.....	16
2.4 Conclusions	22
3. Electron Transfer, Hole Transfer and Triplet Energy Transfer in CdSe/CdS core/shell QDs.....	24
3.1 Introduction.....	24
3.2 Methods	27
3.3 Result.....	28
3.3.1 Triplet energy kinetics.....	28

3.3.2	Core/shell QDs wave function and excitation energy	30
3.3.3	ET between CdSe/CdS QDs and MV ²⁺	33
3.3.4	HT between CdSe/CdS QDs and PTZ.....	34
3.3.5	TET between CdSe/CdS QDs and ACA.....	35
3.3.6	Broadening of charge transfer coupling by QD shell thickness distribution	37
3.4	Conclusions	41
4.	Chiral Imprinting on Perovskite Nanoplatelet	44
4.1	Introduction.....	44
4.2	Method	48
4.2.1	Particle-in-a-Box model for chiral imprinting.....	48
4.2.2	TD-DFT calculations on perovskite cluster	50
4.2.3	DFT calculations on bulk perovskite.....	51
4.3	Result.....	52
4.3.1	Influence of halide composition on the chiroptical properties of NPLs.....	52
4.3.2	Computed optical transitions and CD response in perovskite NPLs.....	54
4.3.3	Temperature-Dependent Studies of the NPL Ligand Shell and CD Signal..	55
4.3.4	Role of chiral ligand orientation in chiral imprinting.....	59
4.3.5	CD as a function of chiral ligand coverage.....	60
4.4	Conclusion	65
5.	Control of Photoinduced Electron Transfer Yield with Polarized Light.....	67
5.1	Introduction.....	67
5.2	4-state model for polarization-dependent photoinduced electron transfer.....	70

5.3	Results	75
5.3.1	Polarization dependent excited states.....	75
5.3.2	Time evolution of coherently excited states without decoherence	80
5.3.3	Electron transfer driven by polarized light in a dissipative environment....	83
5.3.4	Yield difference dependence on molecular orientation.....	89
5.4	Discussion.....	92
6.	Conclusions	95
	Appendix A.....	100
	Appendix B.....	103
	Appendix C.....	109
	Appendix D.....	118
	References	126
	Biography.....	142

List of Tables

Table 1: effective mass the potential for the CdSe/CdS core/shell DVR calculation	27
Table 2: computed electron 1s state energy, hole 1s state energy and excitation energy of CdSe/CdS QDs.....	31
Table 3: Summary of ET and HT rate for CdSe and CdSe/CdS nano structure.....	32
Table 4: The total electron transfer yield difference for different distributions of donor molecule orientations.....	92

List of Figures

Figure 1: Illustration of 3D, 2D, 1D and 0D nano particles.....	4
Figure 2: Schematic representation of core/shell QDs alignment.....	7
Figure 3: A. Cartoon describing the attachment of the nanoparticles on a microbead.....	10
Figure 4: Schematic representation of the effective potentials for the linked.....	13
Figure 5: Illustrative plot of the states of coupled QDs.....	16
Figure 6: Wave function of first two eigenstate of the coupled QDs.....	17
Figure 7: distance dependence of electronic coupling.....	19
Figure 8: Contour plot of decay constant as a function of bridge radius and bridge potential.....	19
Figure 9: The estimated energetics of the CdSe/CdS QDs	26
Figure 10: XB kinetics at the core $1S_h-1S_e$ transition for QDs (red) and QD-ACA complex.....	29
Figure 11: The radial $1s$ (A) electron and (B) hole wave function of CdSe/CdS QDs at 0, 0.32, 0.48, 1.05 and 1.3 nm shell thickness.....	32
Figure 12: Measured electron transfer, hole transfer and triplet energy transfer rate as the function of shell thickness.....	36
Figure 13: Extracted TET coupling decay constant as a function of total reorganization energy.....	37
Figure 14: Size distributions of the synthesized CdSe QDs and CdSe/CdS core-shell QDs extracted from the TEM images.....	40
Figure 15: The broadening effect of CdSe/CdS core/shell charge transfer.....	41
Figure 16: Schematic representation of the methylammonium lead halide perovskite NPL structure with chiral S-PEA ligands and achiral OA ligands.....	52
Figure 17: Optical properties of NPLs. Circular dichroism (A, B, D, E) and absorption (C, F) spectra for NPLs with different halide and ligand compositions.....	53

Figure 18: Temperature dependence on ligand coverage and CD spectra.....	58
Figure 19: Ligand orientation effect on CD signatures.....	60
Figure 20: Coverage dependence of chiroptical properties.	65
Figure 21: (A) Schematic illustration of the 4-state model	72
Figure 22: Time evolution of the phase and amplitude ratio following excitation of the degenerated donor excited states with CPL.....	80
Figure 23: Electron transfer yield difference as a function of time for circularly polarized excitation.	86
Figure 24: Electron transfer yield differences as a function of linear polarized light orientations θ_1 and θ_2	88

Acknowledgements

I would like to express my profound gratitude to my advisor, Professor David Beratan, for his unwavering support and guidance throughout my PhD study. His extensive knowledge and profound insights have been an invaluable resource. His patient mentorship has significantly shaped this journey. He has not only been an excellent mentor but also an inspiring figure, consistently encouraging me to challenge myself, think critically, and persevere despite any challenges I faced. His generosity in sharing his time and expertise, and his enthusiasm for scientific discovery have made my research experience truly enriching. For all this and more, I am sincerely thankful.

Second, I am sincerely thankful to Prof. Peng Zhang, whose insightful discussions, unwavering support, and brilliant ideas have been instrumental in the successful completion of this thesis. His wisdom, enthusiasm, and keen understanding of the subject matter have enriched my learning experience immeasurably. It has been an honor to work alongside him and learn from his profound expertise.

I would also like to express my gratitude to my additional committee members Prof. Michael J. Therien and Prof. Christine K. Payne. Their in-depth queries and insightful feedback challenged me to explore beyond the surface, thereby expanding the breadth and depth of my knowledge. Each meeting with them was an enlightening experience, ensuring that my research was steered in the right direction.

I also want to thank all the Beratan group members for insightful discussions and fun activities.

1. Introduction

In this section, I briefly review background electron transfer theory and aspects of nano particle electronic structure. In chapters 2 and 3, I focus on the distance dependence of quantum dot charge transfer tunneling through the solvent and quantum dot shell respectively. In chapter 4, I focus on the chiral imprinting behavior on perovskite nano platelet. In chapter 5, I discuss a donor-acceptor system that the coherent electron transfer yield can be tuned by light polarization.

1.1 *Electron Transfer Theory*

Electron transfer theory is central part of physical chemistry and biology that describes how electrons move between different molecular entities. This theory is fundamental to our understanding of a wide variety of important chemical and biological processes, including photosynthesis, cellular respiration, corrosion, the operation of batteries and fuel cells, and many others.¹⁻⁵ In the electron transfer reaction, the electron localizes in a donor (D) initially and transfers to the localized acceptor (A) state. When donor and acceptor are weakly coupled, the transition rate can be described by Fermi's golden rule:

$$k = \frac{2\pi}{\hbar} H_{if}^2 F.C. \quad (1.1)$$

where H_{if}^2 is electronic coupling between donor and acceptor states and $F.C.$ is the Frank-Condon factor is the overlap between the vibrational wavefunctions of the initial and final electronic states. There are several methods to calculate the electronic coupling

strength H_{if}^2 such as the block diagonalization method, the generalized Mulliken-Hush (GMH) method, avoided crossing methods, and the fragment charge difference (FCD) method.⁶⁻⁸

In the high temperature limit, the weakly coupled electron transfer rate can be described by the semi-classical non-adiabatic Marcus equation:⁹

$$k_{ET}^{nonad} = \frac{2\pi}{\hbar} \frac{H_{if}^2}{\sqrt{4\pi\lambda k_B T}} \exp \left[-\frac{(\Delta G^{(o)} + \lambda)^2}{4\lambda k_B T} \right] \quad (1.2)$$

where λ is the reorganization energy and $\Delta G^{(o)}$ is the reaction free energy. During an electron transfer, the donor molecule loses an electron and the acceptor molecule gains an electron, which results in changes to the electronic distribution of both molecules. The driving force is the energy difference between the initial and final states of the electron during the transfer process. This is usually determined by the potential difference between the electron donor and acceptor.

λ describes the changes in the atomic and molecular arrangements that occur when a molecule loses or gains an electron. The reorganization energy can be divided into two components: inner-sphere reorganization energy (λ_i) and outer-sphere reorganization energy (λ_o). The inner sphere reorganization energy is associated with changes directly involving the reactant and product (D and A) molecules. This could involve the rearrangement of bonds within the molecules themselves or with the ligands directly attached to them. The inner sphere reorganization can be estimated

experimentally by fitting the Marcus equation with the electron transfer rate and the driving force, or computationally by calculating the energy difference of the molecule before and after the electron transfer.

The outer-sphere reorganization energy is associated with changes in the solvent or environment (reorientation) around the reactant and product molecules. The outer-sphere reorganization can be estimated by Marcus two sphere continuum model:

$$\lambda_o = \frac{e^2}{4\pi\epsilon_o} \left(\frac{1}{2r_D} - \frac{1}{2r_A} + \frac{1}{r_{DA}} \right) \left(\frac{1}{\epsilon_{op}} - \frac{1}{\epsilon_s} \right) \quad (1.3)$$

where e is the elementary charge, ϵ_0 is the vacuum permittivity, r_D is the donor radius, r_A is the acceptor radius, r_{DA} is the donor-acceptor center-to-center distance, ϵ_{op} is the solvent optical constant and ϵ_s is the solvent dielectric constant.

Depends on the relation between λ and driving force ($-\Delta G^{(o)}$), the electron transfer can be classified as:

- Inverted: $\lambda < -\Delta G^{(o)}$
- Barrierless: $\lambda = -\Delta G^{(o)}$
- Normal: $\lambda > -\Delta G^{(o)}$

1.2 Nanoparticles

Quantum dots (QDs) are semiconductor particles that are small enough to exhibit quantum mechanical properties. QDs have a wide range of applications across

various fields including energy harvesting, quantum computing and biomedical imaging.

The nanoparticles can be made of different shapes including “0D” (sphere, cube and other polyhedral in small size), “1D” (rods) and “2D” (platelet) with unique density of states respectively (Figure 1). The 3D nanoparticle is a bulk semiconductor with “infinite” length in all dimensions, while 2D nano platelet, 1D nano rods, and 0D nano cube have one, two and 3 confined dimensions, respectively. The quantum confined nano cubes show discrete density of states.¹⁰

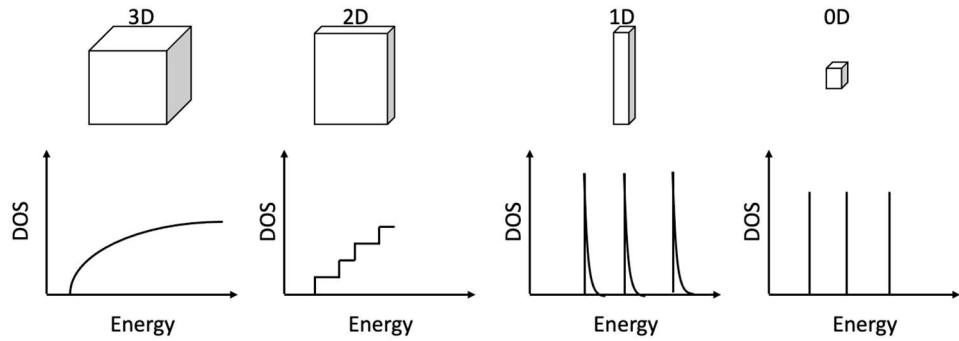


Figure 1: Illustration of 3D, 2D, 1D and 0D nano particles.

Semiconductor nanoparticles are often called artificial atoms because they confine electrons in a space that is comparable to the electrons' de Broglie wavelength, leading to quantized energy levels, much like in individual atoms.¹¹ In the envelop function approximation, the wave function may be written:

$$\Psi(\mathbf{r}) = u(\mathbf{r})F(\mathbf{r}) \quad (1.4)$$

where $u(\mathbf{r})$ is the Bloch function and $F(\mathbf{r})$ is an envelop function. The Bloch function is the rapidly oscillating part of the electron's wavefunction (which is due to the periodic potential of the crystal lattice in the semiconductor), while the envelop function is slowly varying part on the scale of the crystal lattice, and it determines the overall spatial variation of the electron wavefunction in the quantum dot.

In a crystal, the electron potential is periodic due to the repeating of the unit cell, leading to complicated behavior due to interactions with the lattice. This behavior is different from the free motion of electrons typically considered in basic quantum mechanics. The potential of the crystal can be approximated and simplified by assuming the electron behaves as if it were a free electron, but with a different mass, i.e. effective mass. The effective mass can be obtained by taking the second derivative of the energy with respect to momentum (or wave vector k in reciprocal space):¹²

$$m^* = \frac{\hbar^2}{\left(\frac{d^2E}{dk^2}\right)} \quad (1.5)$$

where \hbar is Plank's constant over 2π , E is the energy and k is the wave vector. The Schrödinger equation for the electronic structure of the nanoparticle in the effective mass approximation is:

$$\left(-\frac{\hbar}{2} \nabla \left(\frac{1}{m^*} \nabla + V\right)\right) F(\mathbf{r}) = EF(\mathbf{r}) \quad (1.6)$$

where V is the potential, E is the confinement energy and $F(\mathbf{r})$ is the envelop function. The confinement energy can be found for both the electron in the conduction band and the hole in the valance band. The band gap of nano particles is the sum of the bulk band gap (E_g^0) and confinement energy for both the electron and the hole:

$$E_{gap} = E_g^0 + E_{ele}^{conf} + E_{hol}^{conf} \quad (1.7)$$

The wave function and energy of the nano structure can further be tuned by forming semiconductor hetero-nanostructures. The hetero-nanostructures consists two or more joined materials. A common type of semiconductor hetero-nanostructures is a core/shell quantum dot, where the core and shell are different materials. Depending on the band edge alignment, there are 3 main types of core/shell structure as illustrated in figure 2, type I, semi type II and type II. In the type I regime, the core conduction band edge is lower than the shell conduction band edge, while valance band edge is higher than the shell valance band edge, such that both the electron and hole are confined in the core region. In semi type II regime, the conduction band edge of the core and shell are similar, such that the electron delocalizes in the entire quantum dot while the hole is confined in the shell region. In the type II regime, both the conduction band edge and valance band edge of the core is higher for the shell, causing the electron to localize in the shell and the hole to localize in the core.

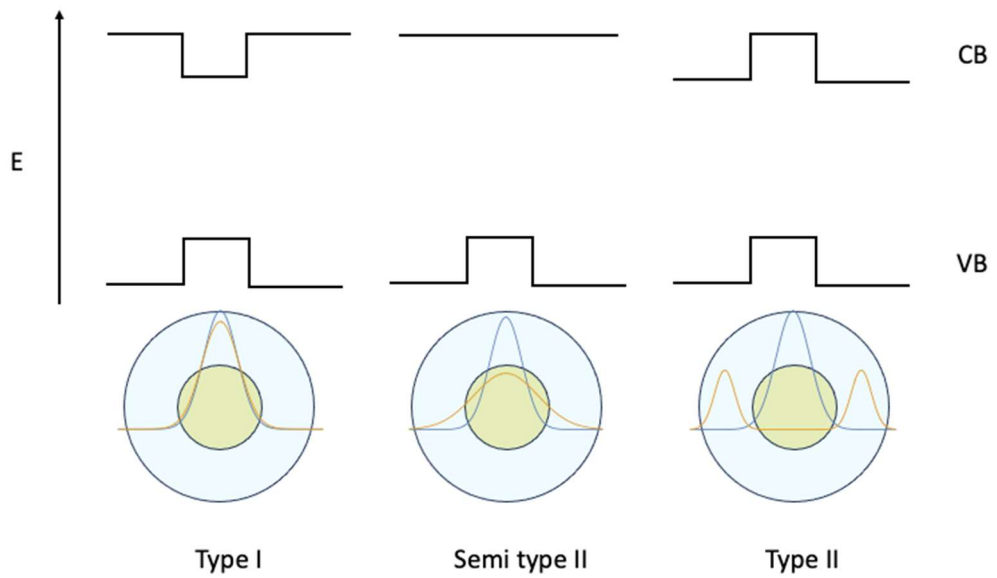


Figure 2: Schematic representation of core/shell QDs alignment. The conduction band and valence band edge are labeled as CB and VB, respectively. The electron and hole wave function (orange and blue line) are shown in lower panel.

2. Size Determines the balance of Through-bond and Through-solvent Coupling Between Linked Quantum Dots

This chapter is adapted from: Zhendian Zhang, Peng Zhang, David H. Waldeck, David N. Beratan. Size Determines the balance of Through-bond and Through-solvent Coupling Between Linked Quantum Dots, manuscript.

2.1 Introduction

Electron transfer (ET) between quantum dots (QDs) is of broad interest in the areas of energy science, photocatalysis and optoelectronics.¹³⁻¹⁹ Electron transfer between colloidal QDs, QDs and metal oxide nanoparticles, and covalently linked QDs is well studied.²⁰⁻²² Electron transfer involving QDs involves a combination of covalent and non-covalent interactions. The aim of this study is to understand the nature of the electronic coupling interactions between QDs given the diversity of through-bond and through-space interactions between interacting QDs in the condensed phase.

Tunneling interactions, of critical importance in charge transport through molecules, are defined by the medium between the donor and acceptor. In macromolecules, for example, the combination of balance of through-bond and through space interactions²³ determine the effective tunneling barrier. As a result, the barrier is larger in alpha helical proteins than in beta barrel proteins since beta strands tend to

form more direct coupling pathways between donors and acceptors than helices. Tunneling between docked protein and through frozen glasses^{24,25} show tunneling barrier effects associated with the structure of the organized solvent. Solvent mediated tunneling is particularly interesting, since through-space contacts are an intrinsic component of the tunneling mediation. Effective tunneling barrier heights through fully covalent saturated linkers tend to be somewhat smaller than the effective barrier heights found in most proteins and solvent glasses²⁵. Unsaturated linkers present even lower tunneling barrier heights and can provide access to resonant or flickering resonance transport regimes.

The richness of bridge-mediated tunneling found in small molecules is mirrored in QD electron transfer systems. Waldeck and co-workers studied electron transfer rates between covalently linked colloidal QDs.²⁶ Their studies find that electron transfer rates decay exponentially with the number of methylene group in the bridge between NPs. The observed decay constant is 0.68 per methylene group (Figure 3). The distance dependence in this system was less than the value of 1.0 per methylene, which is typical for alkane chains. Several reasons are suggested for this, including the presence of an amide linkage, imperfect packing of the ligands, and potential contributions from both “through-bond” and “through-space” superexchange. Wang et al. measured the distance decay of ET rate between QDs and SnO₂ NP for methylene linkers (0.94 per

CH₂) and for phenylene linkers (1.25 per C₆H₄).²⁷ The decay constants for methylene linkers are somewhat smaller than decay constants measured in rigid hydrocarbon linkers between molecular DA pairs.²⁵ This may reflect the flexibility of the linkers used to couple NPs, and the fact that DA distance increase more slowly with linker length than in molecular systems with rigid bridges. Yet, the nature of electron transfer in NPs is qualitatively different from that found in small molecules. In molecular systems, the length scales associated with D, B, and A species is typically the same order of magnitude. However, in linked NPs, the D, B, and A size scales can be qualitatively different. The aim of this study is to understand the consequences of the size scale mismatch in coupled NPs on the mechanisms of tunneling mediation in condensed phase systems. In particular, we will explore how changing NP size can cause a qualitative change in the tunneling mediation mechanism from a through-linker to a through-solvent mechanism, which characteristic changes in tunneling prefactors and decay exponents.

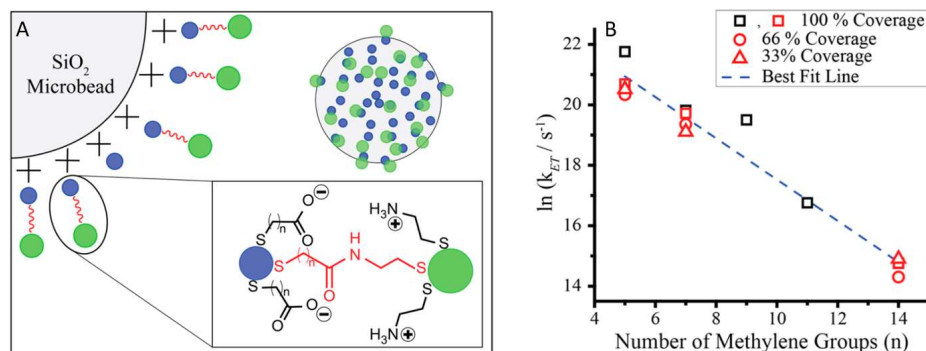


Figure 3: A. Cartoon describing the attachment of the nanoparticles on a microbead. The acceptor nanoparticle (blue) is electrostatically attached to a SiO₂

template and covalently linked (red) to a donor nanoparticle (green) yielding a nanoparticle dyad on the microbead (2NPA). B. Natural log of the electron-transfer rate constant plotted against the number of methylene groups. The blue dashed line shows a best fit, and it has a slope of 0.68 ± 0.04 (error determined via least-squares fitting). The black and red symbols indicate different batches of donor and acceptor nanoparticles. Reprinted with permission from Ref. [30]

2.2 Method

The aim of our studies is to develop a theoretical framework to describe tunneling mediation between coupled NPs as a function of NP diameter. The tunneling can be mediated by a combination of coupling through a covalent linker and by surrounding solvent. Solvent mediated interactions involve mixed through-bond and through-space coupling, while bonded linkers (in an extended geometry) involve mostly through-bond interactions. We aim to develop practical methods to explore the balance between these two kinds of tunneling interactions and to explore how changes in NP diameter may alter the dominance of one tunneling channel over another.

2.2.1 Model potential

We use independent piecewise constant potential electron model potentials to describe mixed through-bond and through-space interactions between QD pairs. Differences between the materials in the four regions of space are characterized by a value of the potential and of the electron mass characteristic of the region. Such model potentials are used widely to study QD systems and their quantum confinement effects.²⁸ Each QD is represented by a three-dimensional constant potential sphere

(Figure. 4); the bridge is represented by a cylindrical constant potential, and a 3D box encloses these two potentials and describes the solvent medium. This simple architecture allows us to describe the tunneling interactions between NPs and to develop simple structure-function relationships.

The electron in the conduction band can be approximated as free electron with different mass. The effective mass is associated with the curvature at band edge. The effective electron mass of CdSe (m_e^*) is $0.13 m_0$ from cyclotron resonance, where m_0 is the free electron mass.^{29,30} The solvent in many of the QD experiments is water, so we take the conduction band edge of water as $-0.05 eV$ vs vacuum.³¹ The reported conduction band edge of bulk CdSe ranges from -4 to $-3.5 eV$,²⁹ We set the potential of the QDs (V_A and V_D) equal to zero, and the potential of the solvent region to $3.45 eV$. The effective through-bridge potential barrier V_B is expected to be lower than the through-solvent barrier V_s , but higher than the QD potential. We would vary V_B from 0 to $3.45 eV$ to examine the influence of the linker electronic structure on the tunneling. The QD radius is set to $15 bohr$, (8 \AA).

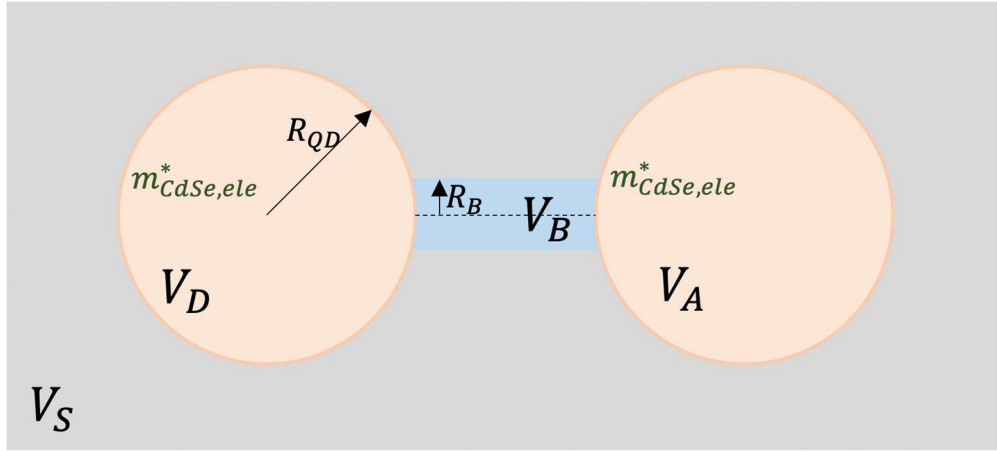


Figure 4: Schematic representation of the effective potentials for the linked. The Orange spheres denote donor and acceptor QDs, respectively. The blue cylinder represents the bridge and the gray region represents the solvent.

We solve the Schrödinger equation numerically on a 3D grid. The grid spacing is fixed to 0.5 bohr, which is sufficiently fine to produce NP-NP couplings that are not mesh size dependent. The distance between the QD edges and the solvent box boundary is 5 Å at the closest point, so the wavefunction amplitude reflection at the boundaries is very small.²⁸

2.2.2 Discrete variable representation (DVR) method

The electronic states of the QD assemblies are described by Schrödinger equation:

$$\left(-\frac{\hbar}{2} \nabla \left(\frac{1}{m^*} \nabla + V \right) \right) \Psi = E \Psi \quad (2.1)$$

where m^* is the effective mass and V is the position-dependent potential. The electron and hole in the semiconducting NP regions have effective masses that do not equal to

the free electron mass. The effective mass depends on the region (left NP, right NP, bridge, solvent). The DVR approach is used to solve the Schrödinger equation on a grid.

The Hamiltonian is

$$H_{i,j,k,i',j',k'} = T_{i,j,k,i',j',k'} + V_{i,j,k,i',j',k'} \quad (2.2)$$

where i, j, k, i', j', k' represent grid points in 3D.

The potential energy matrix is diagonal

$$V_{i,j,k,i',j',k'} = \delta_{i,i'} \delta_{j,j'} \delta_{k,k'} V(x_i, y_j, z_k) \quad (2.3)$$

The kinetic energy operator in 3D is²⁸

$$T_{i,j,k,i',j',k'} = -\frac{\hbar^2}{2} (\delta_{i,i'} \delta_{j,j'} T_{k,k'} + \delta_{i,i'} \delta_{k,k'} T_{j,j'} + \delta_{j,j'} \delta_{k,k'} T_{i,i'}) \quad (2.4)$$

The $T_{i,i'}$ term is

$$T_{i,i'} = -\frac{\hbar^2}{2} \frac{(-1)^{i-i'}}{dx^2} \left(\sum_{k=-1}^{-\infty} \frac{1}{(i-k)(k-i')} + \sum_{k \neq i, i'}^{N_x-1} \frac{1}{m_k^* (i-k)(k-i')} + \sum_{k=N_x}^{\infty} \frac{1}{(i-k)(k-i')} \right)$$

$$= \begin{cases} -\frac{\hbar^2}{2} \frac{(-1)^{i-i'}}{dx^2} \left(\sum_{k \neq i, i'}^{N_x-1} \frac{1}{m_k^* (i-k)(k-i')} + \frac{1}{i-i'} (\psi^{(0)}(N_x-i) - \psi^{(0)}(N_x-i') - \psi^{(0)}(1+i') + \psi^{(0)}(1+i)) \right) & i \neq j \\ -\frac{\hbar^2}{2} \frac{1}{dx^2} \left(\sum_{k \neq i}^{N_x-1} -\frac{1}{m_k^* (i-k)^2} + (\psi^{(1)}(N_x-i) - \psi^{(1)}(1+i)) \right) & i = j \end{cases} \quad (2.5)$$

where $\psi^{(0)}$ and $\psi^{(1)}$ are the digamma and trigamma functions, respectively. N_x is the number of points in the mesh along x direction and dx is the mesh size. The $T_{j,j'}$ and $T_{k,k'}$ can be computed similarly with number of points equals to N_y and N_z . The derivation can be found in appendix A.

Diagonalizing the Hamiltonian gives the energy eigenvalues and eigenstates.

2.2.3 DA Interactions and energy splitting

The D-A interaction is obtained from computing the energy splitting between the HOMO/HOMO-1 or LUMO/LUMO+1 for symmetric model systems. We study the symmetric coupled QDs. As such, the electron's effective mass and the QDs' radii are identical. The ground state S_e in the conduction band of the QDs, are degenerate as shown in Figure. 5. Since the energy difference between S_e state and P_e state is large enough, we can approximately treat the system with the two-state model. The electronic coupling is obtained from the energy gap,

$$|H_{DA}| = \frac{|E_2 - E_1|}{2} \quad (2.6)$$

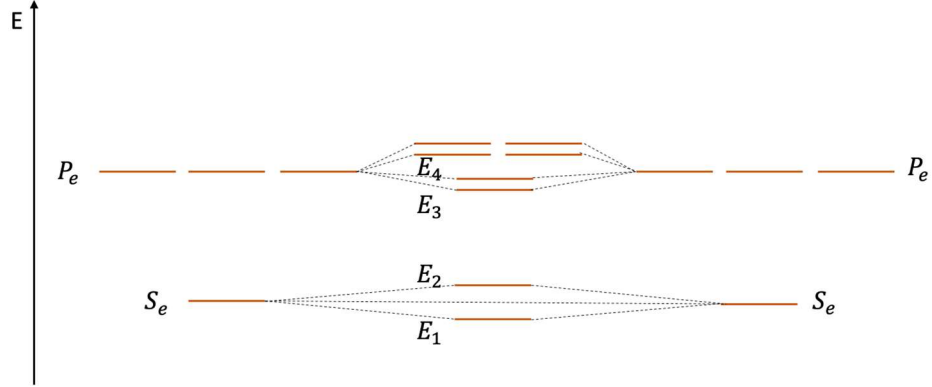


Figure 5: Illustrative plot of the states of coupled QDs. S_e is the conduction band edge of the QDs, P_e are the three degenerate p-orbital like states in conduction band. E_1, E_2, E_3 and E_4 are the lowest eigen-states of conduction band in coupled QDs.

2.3 Results and discussion

In an 1D barrier tunneling model, the DA electronic coupling decays exponentially with distance r ,

$$H_{DA} = H_{DA0} e^{-\beta r} \quad 2.6$$

We investigate the distance dependence of electronic coupling in 3D. An example of wavefunctions of the first two eigenstates of coupled QDs is shown in

Figure. 6. Two degenerate S_e states are mixed to create a bonding and an anti-bonding states.

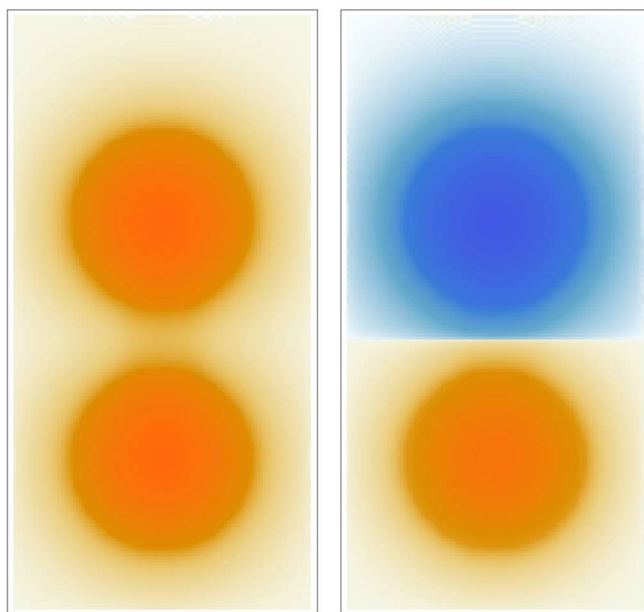


Figure 6: Wave function of first two eigenstate of the coupled QDs.

The electronic coupling through homogeneous solvent without the bridge is first studied to validate our model. The electronic coupling was studied as a function of the edge-to-edge distance between coupled QDs. The edge-to-edge distance was increased from 4 Å to 6.4 Å, which is in the range of experimental condition.²⁶ Figure.7 (A) shows the coupling as the function of distance. The solvent potentials are 1.1, 1.6, 2.4 and 3.45 eV from top to bottom. The coupling decays exponentially as the edge-to-edge distance increases. The pre-factors are almost the same, the relative difference between the pre-

factors is less than 0.5%. The decay constant follows $\sqrt{2m^*(V - E)}/\hbar$. The decay constant through water is reported to range from 0.77 to 0.82 per \AA^{24} . The computed decay constant for 3.45 eV is 0.85 per \AA , which is consistent with the experiment observation.

The TB/TS tunneling are represented by different potentials. Bonds are represented by a cylinder area between QDs with potential lower than the solvent potential but higher than the electron energy eigenstate. Considering a rigid alkane chain as the linker, the largest distance in cross section is 2.8\AA , so the bridge can be regarded as a cylinder with 1.4\AA in. As shown in Figure.7 (B) , we computed coupling where the solvent potential is 3.45 eV to simulate water, the bridge potential is 1.1 eV, and bridge radius varies from 0.5 to 8 \AA . Notice with solvent and bridge barrier, the distance dependence of the coupling is still exponential. There are two limits in Figure.7 (B) : (1) When the bridge radius equals to the QD's radii, the decay constant is 0.34\AA^{-1} which is approximately same as the decay constant 0.4\AA^{-1} when only have 1.1 eV solvent. (2) When the bridge is 0.5 \AA which is negligible compared to the QD radius, the decay constant is same as purely through water decay in our simulation 0.85\AA^{-1} . Depending on the bridge radius, the effective decay constant is between the purely low

barrier decay constant and purely high barrier decay constant.

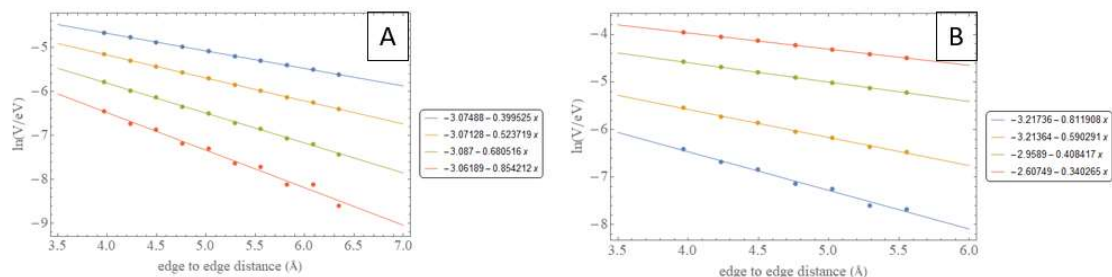


Figure 7: distance dependence of electronic coupling.(A) QDs in solvent only. The solvent potential from top to bottom is 1.1, 1.6, 2.4 and 3.45 eV (B) The solvent potential is 3.45 eV and bridge potential is 1.1 eV. The bridge radius from top to bottom is 0.5, 2.6, 4.8 and 8 \AA .

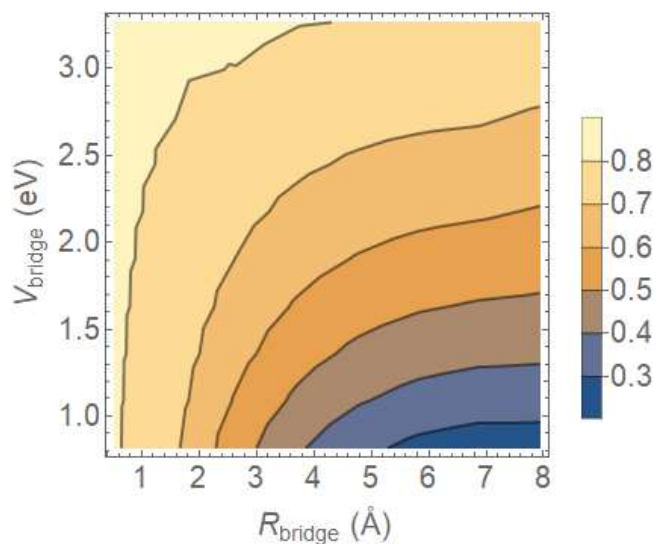


Figure 8: Contour plot of decay constant as a function of bridge radius and bridge potential. The decay constant does not change with bridge potential for small bridge radius. When the bridge radius is close to QDs radii, the decay constant is dominated by through-bridge tunneling.

For a typical rigid alkane linker, the radius of the molecular chain is $\sim 1.4 \text{ \AA}$. Thus, we choose the radius of the cylinder potential (Figure 7 B) is 1.4 \AA . In the calculations, the solvent potential is fixed at 3.45 eV to simulate the effect of water. To demonstrate the difference between through-bridge and through-solvent tunneling, we set the bridge potential to be 1.1 eV . The difference in barrier height is large to have distinct tunneling behavior. We computed the DA coupling by varying the bridge radius from 0.5 to 8 \AA .

The computed distance dependence of the DA couplings shows exponential decay (Figure 7). There are two limits in decay constant (Figure 7 B): (1) When the bridge radius approaches the QD's radii, the computed decay constant is 0.34 \AA^{-1} which is approximately the same as the decay constant of 0.4 \AA^{-1} when DA interaction is entirely mediated by a solvent with a potential of 1.1 eV .

When the bridge radius is 0.5 \AA which is negligible compared to the QD radius of 8 \AA , the decay constant is the same as the purely through-water decay in our simulation, 0.85 \AA^{-1} . Depending on the bridge radius, the effective decay constant is between the purely low barrier decay constant and purely high barrier decay constant.

We investigate the TS and TS contributions to DA coupling using an effective tunneling decay constant. We computed the tunneling decay constants when there is only the bridge potential or solvent potential. The effective tunneling decay constant is derived when both the bridge or solvent potential are present between QDs. If the effective tunneling is close to the one that is derived using only the bridge barrier

potential, the electron transfer between QDs is dominated by the through-bridge tunneling. In contrast, If the effective decay constant is close to the one from solvent barrier potential decay constant, the through-solvent tunneling dominants. We hypothesize that two key factors affect the dominance of through-bridge and through-solvent tunneling: (1) the ratio between the bridge radius and the QDs radii $\frac{R_{bridge}}{R_{QD}}$; (2) the ratio between the through-bridge and through-solvent barrier $\frac{V_{bridge}}{V_{solvent}}$.

As shown in Figure 8, the decay constant changes as the bridge radius varies. When the bridge radius equals to the QD's radii, the effective decay constant is the bridge barrier decay constant, which indicates that the coupling has the signature of through-bridge tunneling. When the bridge radius is 0, then there is effectively no bridge and the electron tunnels through solvent.

The decay constant also depends on the tunneling barrier height. Since the effective decay constant is between decay constant for low potential region and high potential region, we hypothesize that the effective decay constant also depends on the ratio between the potential of two region. Because varying the solvent potential changes the QD energy and varying the bridge potential does not change the energy, we fixed the solvent potential and varied the bridge potential. We assume the bridge is the low potential region and the solvent is the high potential region, so the bridge potential is varied from 0.8 eV to 3.3 eV. The decay constant dependence on bridge radius and bridge potential is shown in Fig. 8. When the radius of the bridge is close to the radii of

the QDs, the decay constant changes as bridge potential. Figure 8 indicates that the decay constant is more sensitive to the radius of the bridge when the bridge radius is small. When $\frac{R_{bridge}}{R_{QD}} < 0.15$, the through-solvent tunneling dominates, so the $\beta_{mixed} \approx \beta_{solvent}$. In this case, we can neglect the bridge in the electron transfer. Consider an alkene chain connecting two QDs. If the alkene chain is rigid and straight, then the radius of the effective bridge is less than 2 Å, the D-A coupling is dominated by solvent. If the bridge is folded, the effective bridge radius will increase, so the bridge makes more contribution.

2.4 Conclusions

Our investigation into quantum tunneling between coupled QDs led us to a better understanding of the factors that influence electronic coupling, including distance, QD size, bridge length and diameter, effective potential depths, and effective mass. Our results demonstrate that decreasing the QD size at a fixed edge-to-edge distance increases the electronic coupling. The electron transfer coupling decay constant was found to arise from a composite of through-bridge and through-solvent interaction.

In the specific case of a cylindrical bridge with a small radius relative to the QD radius (0.1 nm compared to several nm), through-solvent tunneling is shown to predominate. Therefore, when the bridge's size is insignificant in comparison to the QDs (with $\frac{R_{bridge}}{R_{QD}}$ being less than 0.15), the through-bridge electron transfer can be ignored.

However, an exception to this occurs when the bridge is folded or multiple bridging

chains exist between QDs, which leads to an increase in the bridge's contribution.

Therefore, the study underscores the intricate interplay of these factors in modulating quantum tunneling, paving the way for advanced design principles in the development of future quantum electronic devices.

3. Electron Transfer, Hole Transfer and Triplet Energy Transfer in CdSe/CdS core/shell QDs

This chapter is adapted from a collaboration work with Prof. Tianquan Lian's group at Emory University. The Lian group contributed to the synthesis, characterization, and rate measurements of the QD system. Manuscript in preparation.

3.1 Introduction

Quantum dots (QDs), or semiconductor nanocrystals, are garnering significant attention due to their unique properties that make them suitable for various applications, such as solid-state lighting, bio-imaging, and the development of next-generation photovoltaics.³²⁻³⁸ One of their primary characteristics is the tunability of their bandgaps, leading to strong stable emission and low thresholds for multiple exciton generation. This tunability stems from their quantum-confined nature, which allows the modulation of their light absorption properties, making them potential contenders for the role of sensitizers in sensitized solar cells.^{39,40}

Another intriguing feature of QDs is their capacity for efficient triplet energy transfer (TET), a property that can be harnessed for photon upconversion. The efficiency of TET from Cadmium Selenide (CdSe) QDs to molecular acceptors has been established.⁴¹⁻⁴³ This proficiency in TET results from the small energy difference between their singlet and triplet exciton states, underscoring QDs' potential as superb triplet

sensitizers. Optimizing the use of QDs for triplet sensitization, particularly in the infrared spectrum, remains a challenge due to competition with other exciton decay pathways, such as electron or hole transfer and nonradiative recombination within the QD. To overcome this issue, core-shell structures with type I or type II band alignments between the core and shell materials have been employed. These structures can control the spatial distribution of the electron and hole, presenting an additional level of control over the rate of electron and hole transfer.^{42,43}

To augment the effectiveness of TET sensitized by QDs, an in-depth understanding of the underlying mechanism governing this process is indispensable. Techniques with a temporal resolution, such as transient absorption spectroscopy (TA) and time-resolved photoluminescence (TRPL), have been utilized to delve into the dynamics of TET.^{41,44,45} From these studies, most QD-acceptor complexes have proposed the direct Dexter energy transfer (DET) from band edge excitons, while others have identified TET through a charge-separated state and trap state intermediate for systems.^{46,47}

In this study, we aim to test whether TET coupling can be modeled with schemes involving charge transfer virtual states, or whether TET can be considered as simultaneous electron and hole transfer in QD-acceptor. We aim to explore how the reaction free energy influences the TET rate. We also examine the influence of the reaction free energy on the rate of TET. To systematically vary the coupling strength of

TET, we studied CdS shells on CdSe core QDs. Prof. Lian's group measured the dependence of TET coupling on shell thickness, and we compared that with the shell thickness dependence of electron and hole transfer coupling. For this purpose, we used anthracene carboxylic acid (ACA), methyl viologen (MV), and phenothiazine (PTZ) as the TET acceptor, electron transfer acceptor, and hole transfer acceptor, respectively (as depicted in Figure 9).^{48,49} The experimental result and calculations show the weak shell thickness dependence of TET rate originate from the competition of exponential coupling decay and exponential increase of Frank-Condon factor, and the QD shell thickness dispersion effect.

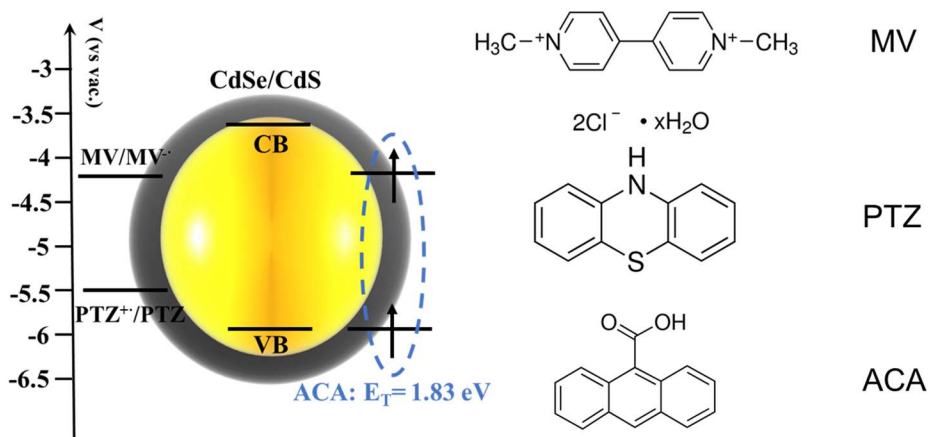


Figure 9: The estimated energetics of the CdSe/CdS QDs , TET acceptor (ACA) and redox potentials of electron transfer acceptor (methyl viologen, MV) and hole transfer acceptor (phenothiazine, PTZ).

3.2 Methods

The experimental methods pursued by the Lian group are provided in Appendix B. Major experimental results are included to facilitate the interpretation of the computational results.

The DVR method described in section 2.2 is used to simulate the CdSe/CdS core/shell QDs confinement energy and wave function. The electron and hole effective mass, conduction band edge, valance band edge of CdSe, CdS and hexane are given in Table 1.⁵⁰

Table 1: effective mass the potential for the CdSe/CdS core/shell DVR calculation

	CdSe	CdS	hexane
m_e^* / m_0	0.13	0.21	1
m_h^* / m_0	0.45	0.80	1
V_e / eV	-4.0	-3.78	0
V_h / eV	-5.7	-6.29	-8.4

3.3 Result

3.3.1 Triplet energy kinetics

Figure 10 illustrates the exciton bleach (XB) kinetics of free QDs and QD-ACA complexes, and the growth of the 3ACA* signal. XB kinetics were acquired from corresponding peak positions, and the 3ACA* signal from averaged kinetics after subtracting the QD signal. The 3ACA* signal in CdSe QD-ACA doesn't rise until 1 ns, contrasting with a notable decrease in XB signal within 1 ns due to electron trapping. 3ACA* signal growth spans tens of nanoseconds. CdSe/CdS QD-ACA complexes display marginal 3ACA* growth within 1 ns, ending largely within 10 ns, indicating quicker TET rates than CdSe QD-ACA. XB decay in CdSe/CdS QD-ACA complexes is faster due to TET, with a decreasing difference as shell thickness increases, implying slower TET rates. These findings align with changes in the 3ACA* signal in TA spectra, suggesting alterations in TET efficiencies in QD-ACA complexes relate to TET rate changes.

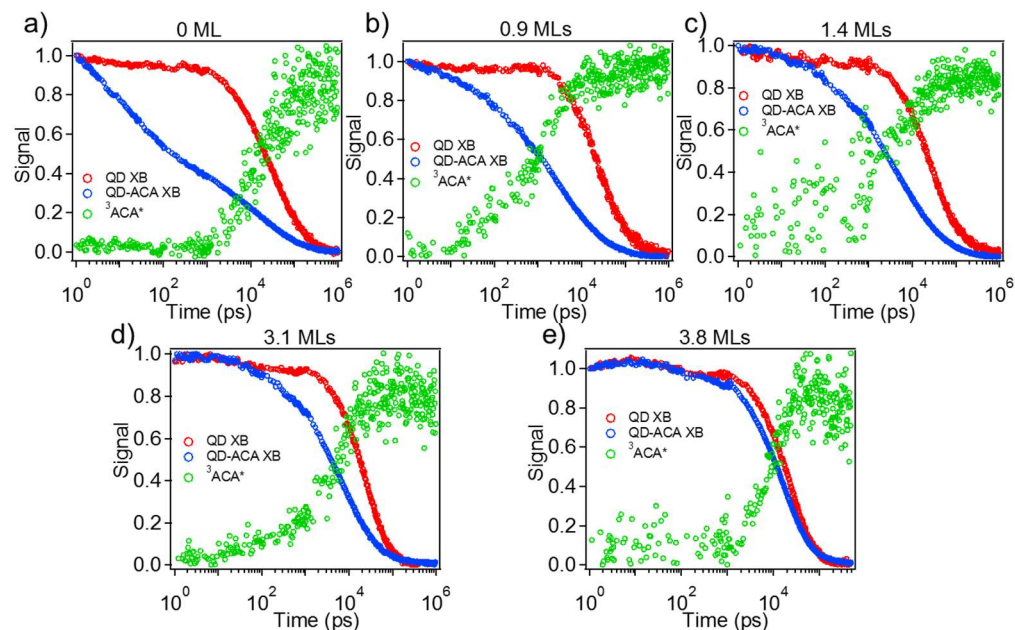


Figure 10: XB kinetics at the core $1S_h-1S_e$ transition for QDs (red) and QD-ACA complex (blue) along with $^3ACA^*$ signal growth kinetics (green) in time range of 1 ps – 1 μ s. a), b), c), d) and e) correspond to CdSe/CdS QDs with 0, 0.9, 1.4, 3.1 and 3.8 monolayers of CdS shell, respectively.

Determining the TET rate from the QD to an acceptor (k), essential for studying TET coupling strength in core-shell QD-ACA complexes, proved challenging for the following reasons: 1. An excess of ACA in the TA experiments complicated accurate quantification of ACA adsorbed on QD surfaces from UV-vis spectra. ACA absorption in these spectra represents both free and QD-attached ACA. 2. XB kinetics in CdSe and CdSe/CdS QDs don't faithfully represent band edge exciton populations due to surface trap states. In CdSe QDs, band edge holes are primarily trapped on the surface, meaning XB kinetics largely show trap exciton dynamics. For CdSe/CdS QDs, the presence of surface trap states and their contribution to XB kinetics can't be ignored given the non-

unity PL quantum yields of the QDs. 3. ACA* growth in TA spectra is credited to TET from both band edge and trap excitons. In the CdSe-ACA complex, deep trap excitons significantly contribute to TET with slower rates. The influence of deep trap excitons on TET in the CdSe/CdS-ACA complex is uncertain and difficult to investigate due to the lack or minimal spectral fingerprints of these excitons.

3.3.2 Core/shell QDs wave function and excitation energy

The CdSe/CdS core/shell QDs are simulated using the discrete variable representation (DVR) method, with effective masses and potentials shown in Table 1. The energy and wave function of the 1s states in conduction band and valence band were determined numerically. The computed excitation energy is consistent with the band edge excitation energy measured from UV-vis spectra (Table 2). The wave function obtained from the DVR calculation is grid based. To obtain analytical expressions of the core/shell QD wave functions, the 1s wave function is first separate into radial and spherical parts $\psi_{1s} = \frac{1}{\sqrt{4\pi}}R(r)$. The radial wave function is fit to a zeroth-order spherical Bessel function $\frac{\sin \kappa r}{\kappa r}$ and spherical Hankel function of the first kind $\frac{\exp \kappa r}{\kappa r}$ with $\kappa = \sqrt{\frac{2m^*|V-E|}{\hbar^2}}$ when the energy is lower than the potential and the energy is higher than the potential, respectively. The coefficient for each region is determined by the continuity at the core/shell and shell/solvent boundaries as well as a normalization condition. The wave functions fitted using the energy and continuity conditionals match the numerical

wave functions obtained in the DVR calculations (Figure 11). Figure 11 shows that the electron delocalizes over the entire core/shell QDs while the hole localizes mainly in the core region. This finding is consistent with the semi-conductor semi-type II alignment of the CdSe/CdS core/shell QDs.

Table 2: computed electron 1s state energy, hole 1s state energy and excitation energy of CdSe/CdS QDs at 0, 0.32, 0.48, 1.05 and 1.3 nm shell thickness with experimental excitation energy.

Shell thickness (nm)	$E_{1s,ele}(eV)$	$E_{1s,hol}(eV)$	$E_{1s,ele-1,hole}(eV)$	$E_{ex,UV-vis}(eV)$
0	-3.42	-5.97	2.54	2.42
0.32	-3.57	-5.91	2.34	2.30
0.48	-3.60	-5.90	2.30	2.25
1.05	-3.68	-5.90	2.22	2.19
1.3	-3.70	-5.90	2.20	2.18

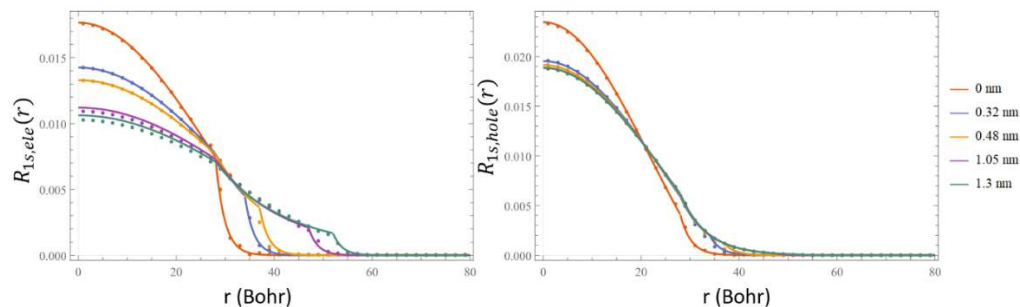


Figure 11: The radial 1s (A) electron and (B) hole wave function of CdSe/CdS QDs at 0, 0.32, 0.48, 1.05 and 1.3 nm shell thickness. Dots represent the numerical wave function computed with DVR method and the solid lines represent the fitted wave function.

Table 3: Summary of ET and HT rate for CdSe and CdSe/CdS nano structure. The ET acceptor and HT acceptor for all experiments are MV and PTZ, respectively.

	k (ns^{-1})	<i>Solvent</i>	β_k
ET, 1.5 nm CdSe (this work)	1500	hexane	0.3
ET, 1.2 nm CdSe + 2.2 nm CdS shell ⁴⁸	5000	chloroform	-
ET, 3nm CdSe + 0.1 nm CdS shell ⁵¹	500	hexane	0.33
ET, 2.4 nm + 0.4 nm CdS shell ⁵²	50	chloroform	0.13
HT, 1.5 nm CdSe (this work)	2.6	hexane	0.1
HT, 1.8 nm CdSe ⁴⁹	0.4	heptane	-
HT, 1.8 nm x 17 nm CdSe nanorod ⁵³	0.7	toluene	0.3

3.3.3 ET between CdSe/CdS QDs and MV²⁺

The measured ET rate between the CdSe/CdS core shell QDs and MV²⁺ decays exponentially from 1460 to 14 ns⁻¹ with shell thickness, with a decay constant 0.3 Å⁻¹ (Figure 12). Wachtveitl reported a β_k value of 0.33 Å⁻¹ while Smith reported a β_k of 0.13 Å⁻¹ (Table 3), despite the differences in core radius and solvent, which affect the reaction free energy and reorganization energy. The ET coupling is extracted using the non-adiabatic Marcus equation (Equation 1.2). The solvent is non-polar hexane, producing a small outer sphere reorganization energy. The QDs also have a small reorganization energy (less than 10 meV)⁵⁴, with the main contribution coming from the inner organization energy of MV²⁺. The reaction free energy for ET is shell thickness dependent, as the CdSe/CdS has semi-type II band alignment with a shallow shell potential barrier, allowing the electron in the conduction band to delocalize into the shell. Using the DVR method, the conduction band 1s orbital energies are -3.79, -3.86, -3.87, -3.91 and -3.91 eV, for 0, 0.32, 0.48, 1.05 and 1.3 nm of CdS shell, respectively. The reduction potential energy for MV²⁺ is reported -4.4 eV vs vacuum. The extracted ET coupling ranges from 0.03 to 0.001 eV depending on the shell thickness and shows exponential decay with decay constant 0.23 Å⁻¹. Using the analytical wave function fitted from the DVR calculations, the distance decay of the ET coupling is computed by assuming that the ET donor and the ET acceptor are weakly coupled, so that the ET coupling is proportional to the surface density of wave function, i.e., $V_{ET} \propto \frac{\int \psi_{1s,ele} d\mathbf{r}^3}{S}$

where S is the QD surface area. The computed decay constant for ET coupling is 0.21 \AA^{-1} , which is consistent with the ET decay constant of the extracted from experiments. Since the band edge difference of the CdS shell and the CdSe core is 0.22 eV , the decay constant of the wave function in the shell is less than 0.1 \AA^{-1} . The decay constant of 0.21 \AA^{-1} arises from the decay of wave function at the surface and the increase of the surface area as the shell thickness increases.

3.3.4 HT between CdSe/CdS QDs and PTZ

The HT rate found in the experiments is much faster than is found in other studies (Table 3). In the experiment, the HT rate for bare CdSe core is 2.6 ns^{-1} , while in Lian's work of 2008 and Kelley's work of 2009, the HT rates are 0.4 and 0.7 ns^{-1} , respectively^{49,53}. In Lian's study in 2008, the HT was fit to a bi-exponential function, and the rate is amplitude weighted. In contrast, the experiment fits the HT to a single exponential function corresponding to the fast component. The measured HT rate shows an exponential decay with decay constant of 0.1 \AA^{-1} (Figure 12). Kelley reported a HT rate decay constant HT of 0.3 \AA^{-1} between CdSe/CdS core/shell nanorod and PTZ in toluene.⁵³ Assuming non-adiabatic HT, similar to ET, using the measured HT rate, the extracted HT coupling decay constant is 0.06 \AA^{-1} , which is much smaller than ET decay constant. Under effective mass approximation, the HT should have a larger decay constant than ET due to a deeper tunneling barrier and larger effective mass through

shell. DVR calculations predicts the decay constant of HT coupling through CdS shell

$$\beta'_{V,HT} = 0.3 \text{ \AA}^{-1}.$$

3.3.5 TET between CdSe/CdS QDs and ACA

The measured TET rate of 0.06 ns^{-1} is found to be independent of the CdS shell thickness. Fitting rates to exponential functions of shell thickness yields a decay constant of 0.02 \AA^{-1} (Figure 12). The QDs $1S_e - 1S_h$ excitation energy depends strongly on the CdS shell thickness. Therefore, the reaction free energy also depends on the shell thickness. For the TET, $-\Delta G > \lambda$, as the shell thickness increases, the TET becomes less inverted. The TET rate and decay constant is sensitive to the reorganization energy (Figure 13). Taking the inner sphere reorganization energy of ACA $\lambda_{ACA^*/ACA} = 0.22 \text{ eV}$ reported by Van Voorhis and assuming the total reorganization energy is approximated by $\lambda_{ACA^*/ACA}$, we extract $\beta'_{V,TET} = 0.19 \text{ \AA}^{-1}$. Although $\beta'_{V,TET}$ is still less than the sum of computed HT and ET decay constant ($0.19 + 0.3 \text{ \AA}^{-1}$), the decay constant for TET, HT and ET are on the same order of magnitude. We propose that due to the DA interaction, the ACA excitation energy and reorganization energy deviate from the value measured and computed in the gas phase. If the reorganization energy or ACA excitation energy is decreased by 0.2 eV , the extracted coupling decay constant from the TET rate will reach 0.5 \AA^{-1} , which is the computed $\beta_{ET} + \beta_{HT}$. The TET rate is observed to be independent of the shell thickness, which may be explained by the fact that as the shell thickness

increases, the TET coupling decreases exponentially, while the Franck-Condon factor increases exponentially with the decay and growth constants being similar in magnitude. The combined effect of these two factors, therefore, results in the TET rate remaining unchanged irrespective of the shell thickness.

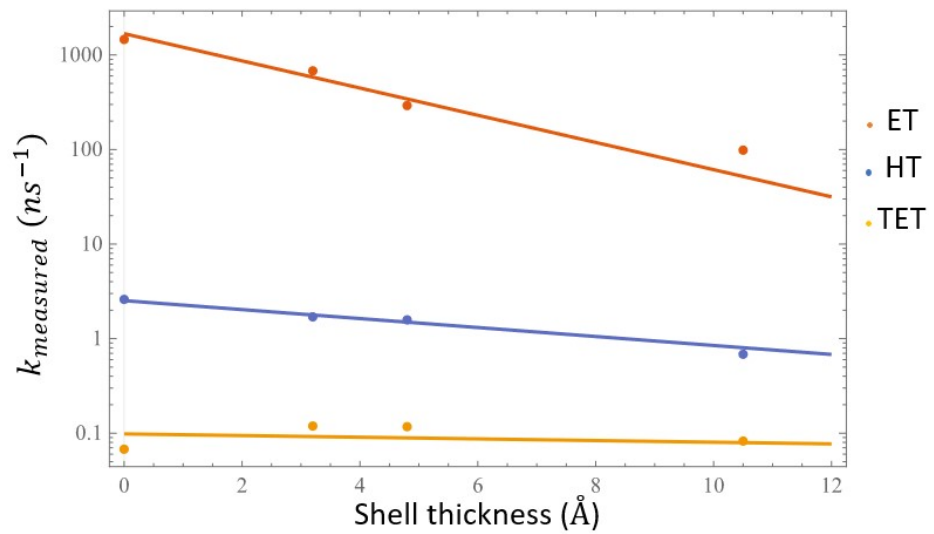


Figure 12: Measured electron transfer, hole transfer and triplet energy transfer rate as the function of shell thickness.

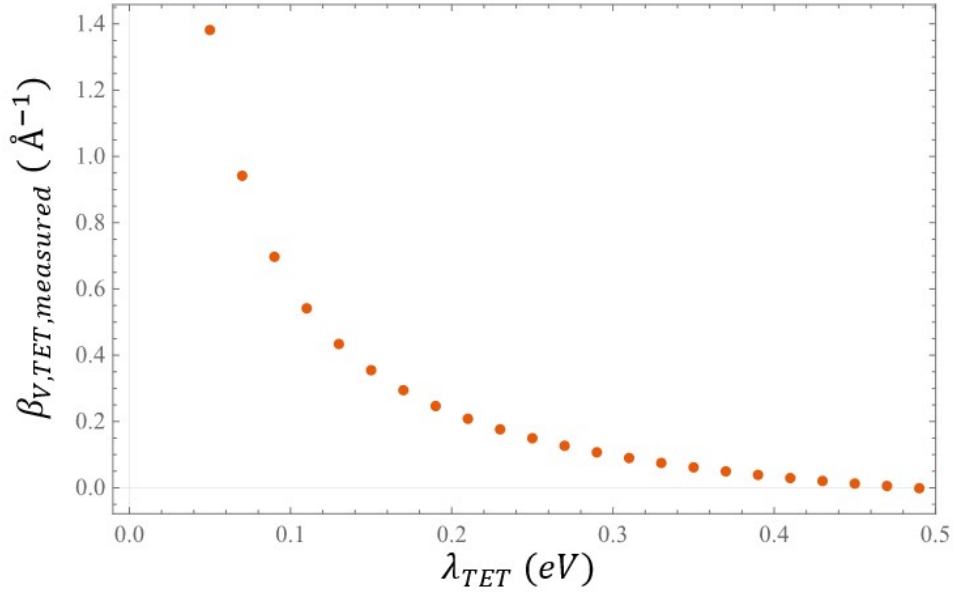


Figure 13: Extracted TET coupling decay constant as a function of total reorganization energy.

3.3.6 Broadening of charge transfer coupling by QD shell thickness distribution

In core/shell quantum dots (QDs), charge transfer coupling between the electron (ET) and hole (HT) states and the dark acceptor (DA) state weakly coupled to the QD shell is determined by the thickness of the shell. For a QD shell that has a potential barrier higher than the electron or hole state energies, the charge transfer coupling decays exponentially with shell thickness. Assuming core/shell QDs are spherical with shell thickness x with the QD donor state energy level changes weakly with shell thickness, the DA coupling is $V_{DA}(x) = Ae^{-\beta x}$, where A is pre-factor and β is the decay constant. Assuming the QD shell thickness is normally distributed with mean thickness μ and standard deviation σ , the expectation value of the coupling is

$$E(V) = \int_{-\infty}^{\infty} \frac{1}{\sigma\sqrt{2\pi}} e^{-\frac{1}{2}\left(\frac{x-\mu}{\sigma}\right)^2} A e^{-\beta x} dx = A e^{-\beta\mu} e^{\frac{\beta^2\sigma^2}{2}} \quad (3.1)$$

The first exponential term suggests that the average DA coupling decays exponentially with the mean shell thickness while the second exponential term indicates that the coupling increases exponentially with the shell thickness variance. This is because thin shells contribute more to the ensemble, and larger variance leads to higher probabilities of QDs with charge transfer through the thin shell. If the variance for all batches of QD with different mean shell thickness are the same, the measured charge transfer would have DA coupling decays exponential in the shell thickness with decay constant β . However, if the variance is a function of the mean shell thickness, the measured decay constant β' will deviate from β .

For CdSe/CdS core/shell QDs, the QD diameter distribution is obtained from TEM images (Figure 14). The average diameters (Full Width Half Maximum) of the QDs are 2.94 (0.49) nm, 3.58 (0.59) nm, 3.90 (0.60) nm, 5.04 (1.00) nm and 5.55 (0.90) nm, corresponding to 0, 0.9, 1.4, 3.1 and 3.8 monolayers of CdS shell, respectively. Since the shell is grown on a CdSe core and the shell thickness is controlled by the amount of Cd and S precursor, we can assume that the size distribution of core is same for all CdSe/CdS core/shell QDs. The mean and standard deviation of shell thickness is extracted from the QDs average diameters and widths. The standard deviation of the core/shell structure radius are 0.251, 0.255, 0.425 and 0.382, suggesting that the standard deviation of the shell thickness increases with the mean. The increase of the shell

thickness will weaken the decay constant of the coupling according to equation 3.1. Interestingly, the softening effect is more significant for larger decay constants because of the β^2 in the second exponential term of Equation 1. For electron transfer with $\beta_{ET} = 0.19 \text{ \AA}^{-1}$ and the hole transfer with $\beta_{hole} = 0.3 \text{ \AA}^{-1}$, substituting the mean and the deviation of the shell thickness above into Equation 3.1 shows that the electron transfer distance dependence is softened slightly with $\beta'_{ET} = 0.17 \text{ \AA}^{-1}$, while the hole transfer decay constant becomes $\beta'_{HT} = 0.25 \text{ \AA}^{-1}$ (see Figure 15).

In conclusion, the increase of the QD shell thickness standard deviation softens the apparent decay of the charge transfer and TET coupling, with a more significant effect for HT than ET. This correction decreases the difference between the HT and ET decay constants for the CdSe/CdS QDs.

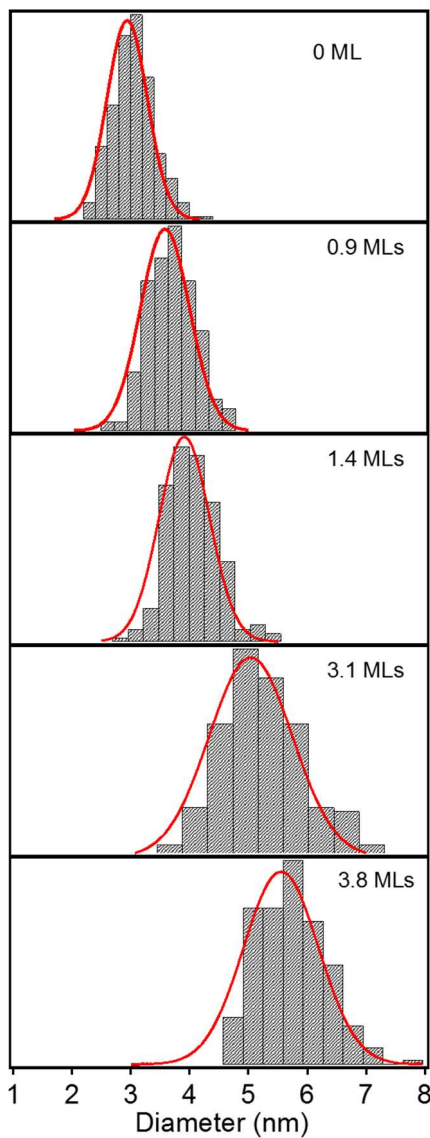


Figure 14: Size distributions of the synthesized CdSe QDs and CdSe/CdS core-shell QDs extracted from the TEM images. The red solid lines are the fitting curves of the diameter histograms. The average diameters (widths) of the QDs to be 2.94 (0.49) nm, 3.58 (0.59) nm, 3.90 (0.60) nm, 5.04 (1.00) nm and 5.55 (0.90) nm.

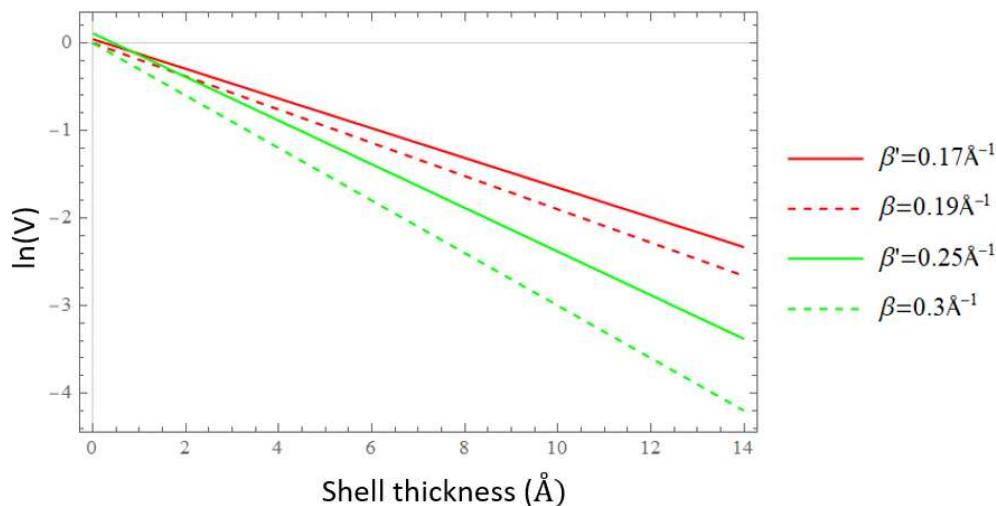


Figure 15: The broadening effect of CdSe/CdS core/shell charge transfer. Red and green represent ET and HT respectively. The dashed lines represent the uncorrected coupling, and the solid lines represent the fitting of shell thickness distribution corrected coupling. The dots represent the corrected coupling at given mean of shell thickness.

3.4 Conclusions

We analyzed the measured ET, HT and TET rates in CdSe/CdS core/shell QDs. While the exponential distance decay of charge transfer tunneling through solvent or ligands, creating exponential decay of the coupling²⁶, the increase of shell thickness decreases both the coupling and the QD excitation energy. The change of QDs energy level affects the charge transfer and TET transfer rate through changes to the Franck-Condon factor. The confinement energy of core/shell QD structure with low shell barriers is more sensitive to the shell thickness. For example, in the inverted regime $\Delta G^{(o)} + \lambda < 0$, assuming the core/shell QD is the ET donor, $-\Delta G^{(o)}$ decreases as the

conduction band edge energy decreases (due to the increase of shell thickness), producing an exponential increase in the Franck-Condon factor. In addition, the reorganization energy and temperature are key contributors to the charge and energy transfer rate dependence on the shell thickness decay, through the $\frac{1}{4\lambda k_B T}$ Marcus factor in the activation energy. By tuning the alignment of the band edge and the effective masses of the QDs, core and shell thicknesses, and the reorganization energy, the shell thickness dependence of the rate could show non-exponential behavior. We predict that a low shell barrier potential and donor with small reorganization energy in the inverted regime, the transfer rate would increase exponentially with shell thickness. If the increase of shell thickness continues such that the $\Delta G + \lambda > 0$, the transfer rate would then decrease exponentially with a large decay constant (faster than the decay of V^2).

We explored the effects of QD shell thickness dispersion on the ensemble average distance decay of the coupling. Assuming that the QD shell thickness has a Gaussian distribution, for a given mean shell thickness, the QDs with smaller shell thickness make greater contribution to the measured rate. If the increase of standard deviation is accomplished by an increase of the mean shell thickness, the measured rate decay will be smaller than the rate for a single DA pair at the mean shell thickness. The shell thickness dispersion effect may not be obvious in adsorption spectra since the excitation energy is less sensitive to the shell thickness. However, the dispersion effect

would vary the measurement that changes rapidly with respect to the shell thickness, such as charge transfer that tunnel through the shell.

4. Chiral Imprinting on Perovskite Nanoplatelet

This chapter is adapted from: Georgieva, Z. N., Zhang, Z., Zhang, P., Bloom, B. P., Beratan, D. N., & Waldeck, D. H. (2022). Ligand Coverage and Exciton Delocalization Control Chiral Imprinting in Perovskite Nanoplatelets. *The Journal of Physical Chemistry C*, 126(37), 15986-15995. Zheni Georgieva contributed to the synthesis and characterization of perovskite nanoplatelets.

4.1 Introduction

Hybrid perovskite materials show promise for next-generation optoelectronic and energy capture/conversion materials because of their color tunability,^{55,56} long carrier lifetimes and diffusion lengths,⁵⁷⁻⁶⁰ and large electron/hole mobilities.^{58,61} These factors indicate a promising future for photovoltaic applications of perovskites, which have a light conversion efficiency as large as 25.5% for a single-junction cell,⁶² and other applications relevant to LEDs,^{63,64} lasing,⁶⁵⁻⁶⁷ and sensing.^{68,69} Chirality was recently introduced to perovskite nanostructures,⁷⁰⁻⁸⁰ further expanding their potential applications as circularly polarized emitters^{78,81,82} and sensors.^{74,83} While methods for generating chiral perovskites have been reported,^{70-72,76,84} little is known about the underlying mechanisms of chiral imprinting and the features that give rise to large chiroptical responses. Control over the intensity of chiroptical features is essential, as CD intensity has been shown to be a good predictor of certain electronic properties of chiral

materials.⁸⁵ Chiral imprinting is the transfer of chirality from a chiral species to an achiral partner, resulting in chiroptical signals from the previously achiral object. Signatures of chiral imprinting in optical rotatory dispersion (ORD) and CD spectra have even appeared in studies of chiral species dissolved in achiral solvents. For example, chiral imprinting was predicted and found to induce ORD and CD originating from the solvent when (S)-methyloxirane was dissolved in benzene,⁸⁶ and chiral imprinting was predicted for nano particles as well.⁸⁷ Indeed, the CD and ORD signatures of small molecules can change qualitatively as chiral species selfassemble.⁸⁸ It was also found that the ORD signals of chiral species in solution can change sign as a result of chiral imprinting on the solvent.^{86,89} Theory has been used to assess the physical origins of chiral imprinting at nanoparticle surfaces, and computational tools enable dissection of the molecular origins for experimentally observed chiroptical signatures.⁸⁹⁻

⁹¹ Since the seminal work of Gun'ko and co-workers on the synthesis of chiral CdS nanoparticles,⁹² considerable effort has focused on understanding the origins of chiroptical properties in semiconductor nanoparticles (NPs). One of the following strategies is typically invoked to induce chiroptical properties in NPs: (i) chiral materials may be produced from a stereogenic unit or a chiral crystal structure,^{93,94} (ii) ligands may induce chiral surface features^{95,96} derived from ligand–NP interactions,⁹⁷ and (iii) chiral supramolecular structures may be formed through self-assembly, or within a chiral matrix.⁹⁸ The size, shape, composition, and ligand structure of a NP can contribute to the

observed chiroptical signature.^{99,100} In most cases, the chiroptical features in a CD spectrum can be approximated by computing the derivative of a Gaussian line shape for each exciton transition of the nanoparticle's absorbance spectrum, and this characteristic CD spectrum is associated with the interaction between the NP electronic states and those of the ligand.^{101,102} These chiral imprinting interactions were later framed within the context of a nondegenerate coupled oscillator model⁹⁹ and may explain many of the remarkable properties of chiral NPs. For example, NPs with the same ligand shell, but different crystal structures, show CD signals with the opposite signs.^{102,103} NPs coated with ligands of the same handedness, and similar chemical structure show inverted NP CD spectra,¹⁰⁴ and nonlinear changes in CD intensities are produced as a function of ligand coverage.¹⁰⁵ As well as enhancing our understanding of chiral imprinting, extensive studies of chiral semiconductor NPs have created a foundation that motivates the exploration of new chiral nanomaterials, namely chiral perovskites. Chiral molecules were first incorporated in hybrid organic–inorganic perovskites in 2006 by Billing and Lemmerer;⁷⁰ however, studies of the chiroptical properties of perovskites did not begin until 2017 with the studies of Ahn and co-workers.⁷¹ They reported the synthesis of layered lead iodide perovskite thin films with chiral organic cation spacers, which generated structural chirality within the perovskite crystal lattice and produced mirror-image circular dichroism spectra for cations of opposite handedness.⁷¹ Other chiral imprinting methods for perovskite materials have been reported since, including the use

of chiral ligands to synthesize materials with a noncentrosymmetric space group,⁷³⁻⁷⁷ sol-gel techniques using chiral gelators, and nanoparticle-ligand electronic interactions.^{72,79,80} While recent studies suggest that a combination of structural and electronic interactions is responsible for the generation of chiroptical signatures,¹⁰⁶ identifying the mechanisms of chirality transfer in perovskite materials is an open challenge. Our study aims to further advance the understanding of how the chiroptical properties of colloidal nanomaterials arise from surface passivation with chiral adsorbates. In this study, imprinting of chirality onto the electronic states of methylammonium lead halide perovskite nanoplatelets (NPLs) is realized by encapsulating the NPLs with a mixed layer of achiral and chiral ammonium ligands. A nonlinear relationship was found between the fraction of chiral versus achiral adsorbed ligands and the CD signal. That is, the intensity of the CD signal from the lowest energy exciton transition saturates as the fraction of chiral surface ligands grows. We use a charge perturbed particle-in-a-box model to describe the chiral imprinting and to understand the observed saturation of the experimental CD intensity as a function of the chiral-to-achiral adsorbate ratio. Chiral ligands can imprint chirality onto nanomaterials by inducing electrostatic or structural changes. In our analysis, we assume that the perovskite atomic positions are unperturbed by adsorption. In this approximation, the mechanism for electronic imprinting depends on the size of the NPL exciton and the density of the chiral ligands, as well as the ligand orientation on the NPL surface.

4.2 Method

The experimental methods are provided in Appendix C. Major experimental results are included to facilitate the interpretation of the computational results.

4.2.1 Particle-in-a-Box model for chiral imprinting

We modeled the wave functions and CD spectrum of perovskite NPLs using an infinite 3D particle-in-box model.³³ This model was successfully used to study chiral imprinting on gold clusters. In this model, the electron and hole wavefunctions are treated separately with their own effective mass, $m_e^* = 0.24m_0$, $m_h^* = 0.17m_0$, where m_0 is free electron mass. The effective mass was obtained by taking the second derivative of the energy dispersion relation $E(\mathbf{k})$ at band edge from the band structure calculation, and the computed effective mass is consistent with other calculations.^{53, 54}

We assume that surface ligand induced NPL chirality arises from the electrostatic perturbation of the surface ligand to the wave function of the NPL. We approximate the surface ligand as a set of point charges arranged according to the stereochemistry. The partial charge of R-PEA is modeled from the ground state DFT calculation using Gaussian⁵⁵ with b3lyp⁵⁶ functional and 6-31g** basis set. All hydrogen charges except from one bonded to the chiral center are absorbed in heavy atoms to make a coarse-grained charge model. Only the four atoms (2 C, 1 N and 1 H) connected to the chiral center and the chiral center itself were used to perturb the box wavefunction. The charge perturbation is detailed in equation 1,

$$\hat{V}_{charge} = \sum_i \frac{q_i q_j}{\sqrt{(x - x_i)^2 + (y - y_i)^2 + (z - z_i)^2}} \quad (4.1)$$

where q_i is the point charge for the adsorbates, q_j is 1 or -1 for hole and electron, (x_i, y_i, z_i) is the cartesian coordinate of the point charge.

The perturbation matrix element is $V_{mn} = \langle \phi_m | \hat{V}_{charge} | \phi_n \rangle$ where ϕ_m and ϕ_n are the unperturbed wavefunctions of the electron or hole state. The perturbed wavefunctions ψ' are obtained by diagonalizing the Hamiltonian $H = H_0 + V$, where H_0 is the unperturbed Hamiltonian with eigen energy on its diagonal.

We chose the nodeless $(n_x, n_y, n_z) = (1, 1, 1)$ state to represent the valance band and the double degenerate 1 node states $(2, 1, 1)$ and $(1, 2, 1)$ for conduction band to compute the optical properties, to reflect the s and p orbital composition of valance band edge and conduction band edge. The electric transition dipole moment μ and magnetic transition dipole moment m were computed between the valance band and conduction band

$$\mu = \iiint \psi'_{val} \hat{\mu} \psi'_{con} dx dy dz \quad (4.2)$$

$$m = \iiint \psi'_{val} \hat{m} \psi'_{con} dx dy dz \quad (4.3)$$

where $\hat{\mu} = e(\hat{x} + \hat{y} + \hat{z})$ and $\hat{m} = \hat{r} \times \hat{p}$.

The oscillator strength f and rotatory strength R are

$$f = \frac{2}{3} \Delta E \mu \cdot \mu \quad (4.4)$$

$$R = Im(\mu \cdot m) \quad (4.5)$$

The NPL is modelled by a N-by-N grid where each grid point is a unit cell. We assume the exciton size is much smaller than the size of NPL, and the chiral adsorbates outside of

exciton have no contribution to the CD signal. The rotatory strength is computed between hole ground state (1,1,1) and electron second and third excited states (2,1,1) and (1,2,1). The computed rotatory strength shows mirror image for $\phi_{h,(1,1,1)} \rightarrow \phi_{e,(2,1,1)}$ and $\phi_{h,(1,1,1)} \rightarrow \phi_{e,(1,2,1)}$, which is consistent with the bisignate CD signals for chiral imprinted perovskite. We explored different exciton sizes, from 3 by 3 to 5 by 5 unit cell, i.e. 1.8 nm to 3 nm. We assume the PEA ligands have very little interaction between themselves and thus all have same binding mode. The rotatory strength is sensitive to the configuration of chiral PEA on the surface, as predicted by TD-DFT calculations. For m PEA on an n-by-n grid exciton, there are $\binom{n^2}{m} = \frac{n^2!}{m!(n^2-m)!}$ unique configurations. The rotatory strength of certain number of PEA m on the exciton rot_m is averaged over all configurations. For PEA:OA ratio x, there are $\frac{x}{1+x}N^2$ PEA on a NPL of N^2 grid, thus the probability of m PEA on the exciton is $p_m(x) = \binom{n^2}{m} \binom{N^2 - n^2}{x/(1+x)N^2 - m} / \binom{N^2}{x/(1+x)N^2}$. The overall rotatory strength is the sum over all possible number of PEA on the exciton $rot(x) = \sum_{m=0}^{n^2} rot_m p_m(x)$. When the NPL size N is much larger than the exciton size, increasing the NPL size N has no influence on the averaged rotatory strength. We take N=100, i.e. 60 nm for our calculations.

4.2.2 TD-DFT calculations on perovskite cluster

The halide terminated $3 \times 2 \times 1$ unit cell ($2.4nm \times 1.7nm \times 1.2nm$) $CsPbBr_3$ perovskite clusters are built from the optimized unit cell. Hydrogen atoms are used to cap

surface halide. We used the simplified Tamm-Dancoff approximated (sTDA)⁵⁷ to compute the absorption and CD spectra. The ground state wavefunctions were obtained from the Gaussian package with CAM-b3lyp⁵⁸ density functional and def2-SVP⁵⁹ basis set. The sTDA method is tested and compared with TD-DFT method on a $2 \times 1 \times 1$ cluster with chiral ligands. The computed results show that TDDFT computed absorption spectrum and rotatory strength can be well reproduced by the sTDA method.

4.2.3 DFT calculations on bulk perovskite

We build MAPbBr₃ unit cell with lattice parameter $a=5.9\text{\AA}$.⁶⁰⁻⁶² We performed density functional theory (DFT) calculation using the Vienna ab initio simulation package (VASP)⁶³ to investigate the geometry, band structure, and the density of states of bulk perovskite and nanoplatelets. We used the linearized augmented-plane-wave (LPAW) method^{64, 65} with the Perdew-Burke-Ernzerhof revised for solids (PBEsol)⁶⁶ exchange-correlation functional. The plane-waves were expanded with kinetic energy cut-off of 300 eV. A k-point mesh of $11 \times 11 \times 11$ was used for the sampling of the Brillouin zones.

4.3 Result

4.3.1 Influence of halide composition on the chiroptical properties of NPLs.

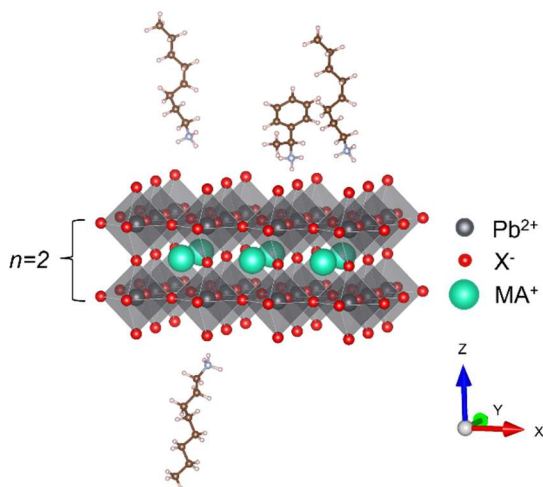


Figure 16: Schematic representation of the methylammonium lead halide perovskite NPL structure with chiral S-PEA ligands and achiral OA ligands. X^- denotes Cl^- or Br^- anions, shown in red. The gray spheres denote the position of Pb^{2+} anions and methylammonium cations are shown as teal spheres. The lead halide octahedra are shown in gray.

Methylammonium lead halide ($\text{X}=\text{Br}$ or Cl) perovskite NPLs with a thickness of $n = 2$, where n is the number of lead halide layers in the structure, were synthesized using previously reported procedures.²⁴ The ligand shell comprises a mixture of achiral octylamine (OA) and chiral ligands, either S-/R-phenylethylammonium (S- or R-PEA), S-/R-naphthylethylammonium (S- or R-NEA), or S-/R-2-octylammonium (S- or R-OA). The structures are represented in Figure 16.

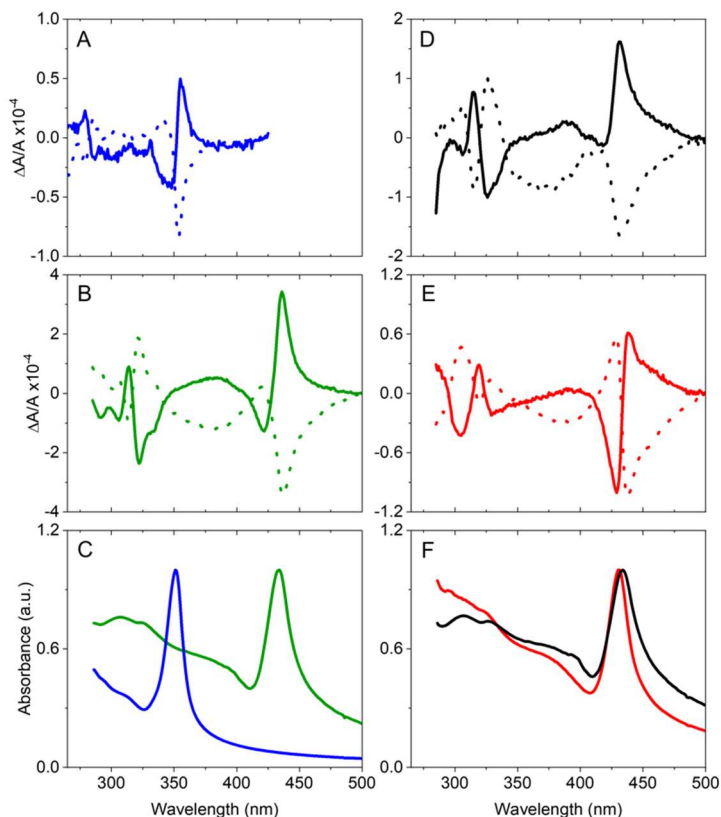


Figure 17: Optical properties of NPLs. Circular dichroism (A, B, D, E) and absorption (C, F) spectra for NPLs with different halide and ligand compositions. Panels A-C show circular dichroism (A, B) and absorbance (C) spectra of methylammonium lead chloride (blue) and bromide (green) NPLs coated with PEA ligands. Panels D-F show circular dichroism (D, E) and absorbance (F) spectra of methylammonium lead bromide NPLs capped with chiral OA (black) and NEA ligands (red). The solid lines in the circular dichroism spectra denote S- chirality and the dotted lines denote R- chirality. The spectra in panel A were collected on quartz slides to avoid solvent interference; all other spectra were collected in toluene solutions.

Figure 17 shows experimental absorption and CD spectra of hybrid organic-inorganic NPLs with the structure $\text{CH}_3\text{NH}_3\text{Pb}_2\text{X}_7$ ($\text{X}=\text{Cl}, \text{Br}$). Panels A ($\text{X}=\text{Cl}$) and B ($\text{X}=\text{Br}$) show CD spectra for NPLs with S- or R-PEA ligands. Figure 17C shows the

corresponding absorbance spectra for the X=Cl and X=Br NPLs. Figure C1 (appendix C) shows absorption and CD spectra for NPLs prepared with a mixture of chloride and bromide, which allows additional tunability of the chiro-optical features. The systematic shift of the exciton transition from 433 nm to 351 nm as the halide composition is changed from 100% Br to 100 Cl is consistent with findings of previous studies and demonstrates that this optical transition arises from the perovskite rather than from the adsorbed ligands. The CD spectra for each of the different types of nanoplatelets show a bisignate line shape (with positive and negative lobes). The CD transitions occur at the frequency of the lowest energy NPL electronic transition. Moreover, the signs of the CD transitions are determined by the handedness of the PEA used during synthesis, the CD transition change sign as the R- and S- adsorbates are interchanged.

4.3.2 Computed optical transitions and CD response in perovskite NPLs.

DFT analysis of bulk MAPbX_3 (Figure C2) indicate that the conduction band minimum (CBM) comprises mainly Pb *p* atomic orbitals and that the valence band maximum (VBM) comprises mainly Pb *s* and halide *p* orbitals, consistent with earlier studies.^{67, 68} The perovskite electronic structure produces a direct bandgap and strong optical transitions.^{67, 68} The energy separation between the two lowest-energy optical transitions in the absorbance spectra for Br NPLs (Figure 17C) is consistent with the computed absorption coefficients of the model perovskite NPL in vacuum (see Figure C3). For the Br NPLs, our computed absorption coefficients show a lowest energy absorption at 534 nm, which is a

longer wavelength than is measured for the NPLs. This difference may arise from solvent effects that are neglected, or from errors introduced by the DFT functional.

CD spectra simulated with a cluster model for a single R- or S- PEA adsorbate are shown in Figure C4, and they exhibit CD spectra with mirror image symmetry and a bisignate line shape. This shape is characteristic of coupled chromophore CD transitions, as a single chromophore (i.e., the chiral ligand alone) does not show bisignate CD features.⁶⁹ A second feature is observed in the experimental CD spectra at a higher energy (~320 nm) and it is weaker than the 433 nm transition (Figure 17A,B). TD-DFT analysis predicts that the oscillator strength of the first exciton transition is ~10 times larger than the higher-energy transition oscillator strength, so the corresponding transition dipole moment is larger while the magnitude of magnetic dipole moments are similar for first exciton transition and higher-energy transitions. Because the CD signal is proportional to the inner product of the electric dipole and magnetic dipole transition moments, the high energy transitions, which have smaller magnitudes of the electric transition dipole moments, also have smaller CD rotational strengths.

4.3.3 Temperature-Dependent Studies of the NPL Ligand Shell and CD Signal.

Temperature-dependent CD and ¹H NMR studies were performed on the chiral perovskite NPLs to determine how the dissociation of chiral ligands from the NPL influences the chiral imprinting. Figure 18A–C shows CD and ¹H NMR spectra, collected for the same chiral NPL samples, at temperatures ranging from 20 to 80 °C.

Significant changes in the CD spectra for X = Br NPLs arise upon heating. The CD intensity at 20 °C is 10 times larger than at 80 °C, and the sign of the exciton's bisignate peak reverses at 50 °C; this inversion persists up to 80 °C. Upon cooling the sample back to 20 °C, the CD intensity and bisignate shapes return nearly to those found initially. Similar behavior, including the change in intensity and sign inversion, was also observed for X = Cl NPLs (Figure C5). Previous studies examining temperature-dependent CD signals for chiral perovskites did not report a sign inversion; however, these studies were performed within a smaller temperature range, and in the presence of excess ligand in the solution, which can significantly affect the ligand coverage on the NPL. To explore the temperature-induced changes in the NPL ligand shell, variable temperature ¹H NMR experiments were conducted in deuterated toluene (Figure 18B,C). The NPLs are intact in these studies, and most of the ligands (OA and PEA) are expected to remain anchored to the NPL surface.^{107,108} As such, the proton signals arising from the ligands manifest in the spectra as weak and broadened peaks (blue, green, red, and purple traces). For comparison, spectra of NPLs digested in DMSO-d₆ (black), in which the NPL structure is destroyed and the ligands are free in solution, exhibit sharp, narrow peaks. Figure 18B shows NMR resonances attributed to OA protons, namely those on the terminal -CH₃ group observed at 0.9 ppm and the 14 protons on the alkyl chain at 1.4 ppm. As the temperature increases to 50 and then 80 °C, the peak intensities grow gradually for both OA resonances, suggesting that OA ligands

detach from the NPL surface upon heating. This structural hypothesis is further supported by the appearance of a new peak at 0.9 ppm with sharp features at 80 °C. This new feature corresponds to a similar feature that is found in the digested NPL samples; that is, the OA ligands in the system behave increasingly like free ligands as the temperature is elevated. Upon cooling, resonances from OA become weak in intensity and broadened once again, indicating that achiral ligand desorption is reversible. In contrast, PEA proton resonances that arise from the protons adjacent to the ammonium group (see Figure 18B) are relatively unchanged over the temperature range. Thus, we postulate that the diminished CD signal strength and the sign inversion at higher temperatures arise from orientational changes of the PEA ligands, rather than from any significant detachment of PEA species from the surface. The temperature-dependent NMR data suggest that the NPL ligand shell is less dense at elevated temperatures, caused by a reversible shift in the equilibrium between free and NPLanchored OA molecules. Although the absorbance of the samples does not change significantly, the CD spectra show considerable weakening in their strength at elevated temperatures (see Figure C6). The difference in temperaturedependent behavior between the achiral and chiral ligands suggests that OA desorbs from the surface upon heating, whereas PEA remains anchored, which is consistent with the difference of the linker group, ammonium versus amines. Earlier theoretical studies indicated that cationic organic ammonium adsorbates, such as PEA, form ionic bonds to the perovskite surface with a

binding energy of ~ 1 eV,^{107,108} while OA binds only half as strongly at 0.5 eV.¹⁰⁹ The strong binding affinity of the PEA cations, as compared to OA molecules, suggests that PEA ligands are less likely to detach from the surface at elevated temperatures. The decrease in neighboring adsorbed molecules may allow the PEA ligands to take on geometries where the aromatic ring becomes more nearly cofacial with respect to the NPL surface. Indeed, temperature-dependent reorientation of nanoparticle ligand shells is reported in the literature, and it is understood to strongly influence a material's optical properties.^{110,111}

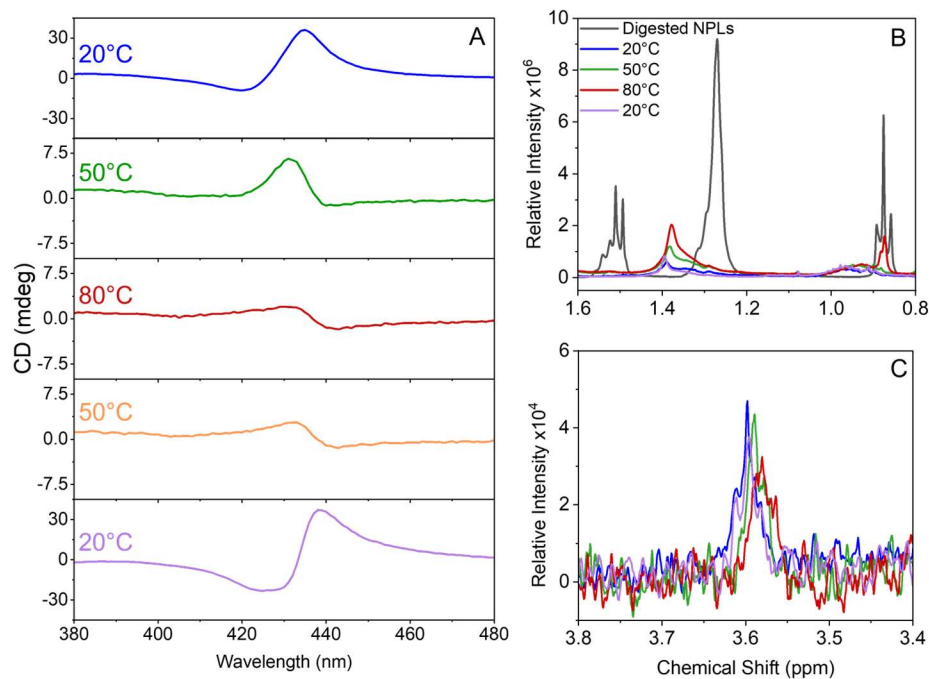


Figure 18: Temperature dependence on ligand coverage and CD spectra. Panel A shows CD spectra at the first exciton transition as a function of temperature. The plots from top to bottom show the process of heating a sample of S-PEA-NPLs to 80°C and then cooling it back down to 20°C. Panel (B) and (C) show 1H-NMR peaks associated with OA and S-PEA ligands, respectively, from a NPL sample dissolved in

toluene-d8 over the same temperature cycle: 20 (blue) 50 (green) and 80 (red) and 20°C (purple). A ¹H-NMR spectrum of digested S-PEA-NPLs in DMSO-d6 is shown in black in panel B.

4.3.4 Role of chiral ligand orientation in chiral imprinting

TD-DFT calculations were performed to explore how ligand reorientation may give rise to an inversion of the CD response. The effect of phenyl ring geometry on the CD response of the chiral NPL system was modeled by varying the angles between a perovskite cluster and a chiral PEA ligand. Ligands with a 120° orientation yielded a computed rotatory strength of -10×10^{-40} cgs, while a 180° orientation gave $+11.8 \times 10^{-40}$ cgs, suggesting that ligand orientation can influence not only the strength of the chiro-optical transition, but its sign as well. Figures 19A and 19B illustrate how the rotatory strength can invert with different chiral ligand orientations. That is, the transition electric dipole and transition magnetic dipole moments rotate with ligand orientation, causing their dot products to change signs. Thus, the imprinted CD signal of the perovskite is sensitive to the orientation of the chiral ligands on the surface. These computational findings are consistent with the observed experimental behavior of the NPLs, further suggesting that changes in ligand orientation, triggered by differences in the ligand shell composition, may result in sign inversions of the CD signal.

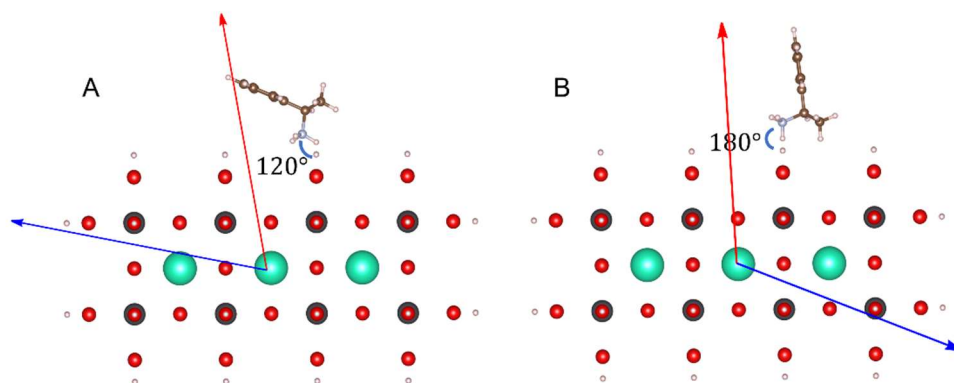


Figure 19: Ligand orientation effect on CD signatures. Panel A and B show unit vectors of electric transition dipole moments (red) and magnetic transition dipole moments (blue) for a CsPbBr₃ cluster with one R-PEA ligand at the band edge transition. Side view of the CsPbBr₃ cluster, angle between H-Br and H-N is 120° (A) and 180°(B).

4.3.5 CD as a function of chiral ligand coverage.

The dependence of NPL chiroptical properties on the surface concentration of chiral ligands was studied by synthesizing NPLs with varied S-PEA:OA ratios, ranging from 1:1 to 7:1, then collecting CD and ¹H-NMR spectra for each sample. The CD intensity was determined by subtracting the trough value (bisignate minimum) from the peak value (bisignate maximum) at the exciton; these values are reported in the unitless quantity $\Delta A/A$ (see Figure 20A). To determine the PEA:OA ligand ratio on the surface of the perovskites, the NPLs were purified to remove excess ligand, then digested in DMSO-d₆ and studied via proton NMR. Representative data and peak assignments are shown in Figure C7. The surface ligand ratios were calculated using equation 4.6,

$$\text{Molar ratio} = \frac{\left[\frac{I_{PEA}}{nH_{PEA}} \right]}{\left[\frac{I_{OA}}{nH_{OA}} \right]} \quad (4.6)$$

where I_{PEA} and I_{OA} are the integrated peak areas of the PEA and OA resonances, and nH_{PEA} and nH_{OA} are the number of protons associated with each peak.

Representative CD and normalized absorbance spectra of S-PEA-capped X=Br NPL samples synthesized with different PEA:OA ratios are shown in Figures 20A and 20B. Ratios of PEA:OA as measured by $^1\text{H-NMR}$ are indicated with a color map; low ratios (as low as 0.05 PEA:OA) are shown in dark green, and high ratios (up to 0.35 PEA:OA) in light green. The upper limit for the PEA:OA ratios was chosen to prevent changes in the NPL thickness distribution triggered by large amounts of PEA, which manifest as a red-shift of the exciton and absorbance peak broadening (see Figure C8); the X=Cl NPLs show a greater tolerance for high chiral ligand concentrations, allowing for larger amounts of PEA to be used in the synthesis before changes in the sample composition are observed. The NPLs' linear absorption properties remain constant within the selected PEA:OA range, based on their normalized absorbance spectra (Figure 20B). The CD intensity (Figure 20A) increases with an increase in the PEA:OA ratio, except for a slight observed decrease for samples with ratios approaching 0.35. Samples with the lowest accessible PEA:OA ratios (Figure 20A, dark green) can exhibit a CD signal inversion at the exciton energy, with the bisignate trough appearing at higher

wavelengths than the peak. CD inversion was not found for X=Cl NPLs in the accessible PEA:OA range.

CD intensities are shown as a function of molar ratio data for X=Br and X=Cl NPLs in Figure 20C. Both the chloride and bromide NPLs show a similar relationship between CD intensity and PEA:OA ratio, with three distinct regions: small slope. (0-0.1 PEA:OA), large slope (0.1-0.25 PEA:OA for Br and 0.1-0.3 PEA:OA for Cl), and a plateau region (above 0.3). These data indicate that the strength of chiral imprinting manifesting in the CD intensity, while proportional to the PEA:OA ratio, is not directly proportional to the fraction of chiral ligands in the shell. That is, a linear dependence of the CD intensity on the ratio of chiral ligands is not observed. A nonlinear relationship between the chiral ligand concentration and the CD intensity was reported previously for cysteine-capped CdSe/CdS QDs and attributed to a change in the cysteine binding motif at different ligand concentrations.⁵¹ Unlike cysteine, PEA has only one moiety available to bind to the NPL surface. Thus, we posit that the nonlinear nature of the CD-PEA:OA relationship arises from the averaging of the CD signal that is produced from NPLs with different PEA configurations.

A chirally imprinted particle-in-a-box model⁸⁷ was used to explore the spectroscopic signatures of chiral imprinting on nanoparticles from a theoretical perspective (see details in Section 4.2.1). We computed the dependence of the rotatory strengths on the PEA:OA ratio using this model and the results are plotted in Figure 20D for three different exciton sizes which are approximated by the number of unit cells over

which the excitons can delocalize. Specifically, grid sizes of 3×3 , 4×4 , and 5×5 unit cells (corresponding to 1.8, 2.4, and 3.0 nm lengths) in the x,y plane of the NPL are considered. The exciton sizes employed in the computations are somewhat smaller than the experimentally measured exciton size (ranging from 2 to 7.1 nm),^{112,113} due to the large computational cost of large exciton. The absolute value of the rotatory strength for the 1.8 nm exciton, see dotted line of Figure 20D, increases rapidly for small PEA:OA ratios; the rotatory strength is 1×10^{-4} atomic units (a.u.) when PEA:OA = 0.1. At higher PEA:OA ratios, the rotatory strength increases steadily and reaches 4.5×10^{-4} a.u. for PEA:OA = 1. The 4×4 and 5×5 cases show a similar shape as a function of PEA:OA ratio. For the 4×4 exciton (2.4 nm, dashed line), the rotatory strength variation has a large slope at low PEA:OA ratios and then reaches a plateau when PEA:OA > 0.4. The maximum rotatory strength of the 4×4 exciton is 5.4×10^{-4} a.u. at PEA:OA = 1. The rotatory strength of the 5×5 (3.0 nm, solid line) exciton increases more slowly than the 4×4 exciton at low PEA:OA ratios. As the PEA:OA ratio increases, the rotatory strength reaches a plateau with a rotatory strength of 4.6×10^{-4} a.u. The slope of the rotatory strength vs. PEA:OA plot decreases for all three exciton sizes, with the two larger exciton sizes showing the largest slope decrease (Figure C9). The rotatory strength reaches a plateau at ratios greater than 0.5 for the 2.4 and 3.0 nm excitons.

While a difference in the position of the rotatory strength plateau is observed in Figure 20D, all three exciton sizes produce similar computed rotatory strength

magnitudes, suggesting that the size of the exciton does not dictate the magnitude of the rotatory strength of the chiral imprint. Larger excitons can be perturbed by more PEA at fixed PEA:OA ratios, but the exciton wavefunction is more spatially delocalized in a larger potential well. Therefore, the magnitude of the rotatory strength is similar for the three exciton sizes. The two larger excitons (2.4 nm and 3 nm) show a clear saturation of rotatory strength as the PEA:OA ratio approaches 1, while the position of the saturation point for the 1.8 nm exciton is less clear. When the exciton size is small (i.e., comparable to the size of the chiral ligand), the asymmetric charges associated with the stereogenic center are similar in size to the wavefunction of the confined exciton. The induced rotatory strengths are large (compared to that from a large size exciton) and are strongly dependent on the placement of chiral ligand asymmetric charges. Therefore, the rotatory strengths produced by placing chiral ligands symmetrically with respect to the exciton wavefunction inversion center, cannot be canceled. In contrast, for large excitons, the induced rotatory strengths are relatively weak and less dependent on the chiral ligand position with respect to the exciton wavefunction inversion center. Therefore, the asymmetric environment created by ligand placement is more likely to be averaged out as the size of the stereogenic center of the chiral ligand is small compared to the spatial extent of the wavefunction, and the rotatory strength quickly reaches a plateau at the high PEA:OA ratio, consistent with the computed rotatory strength for large exciton sizes (2.4 and 3 nm).

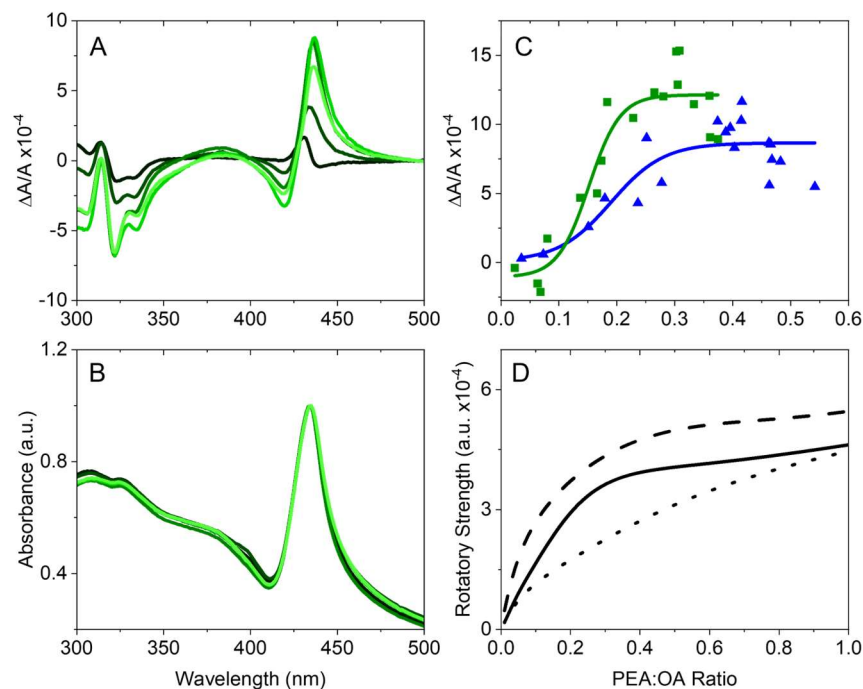


Figure 20: Coverage dependence of chiroptical properties. Panel A shows CD spectra and panel B shows absorbance spectra for toluene solutions of X=Br NPLs synthesized with S-PEA:OA ratios between 0.05 (dark green) and 0.35 (light green). Panel C shows the CD at the first exciton transition as a function of PEA:OA ligand ratio for X=Br (green) and X=Cl (blue) NPLs fit by a Boltzmann function to guide the eye. Panel D shows computational results for the dependence of rotatory strength on the PEA:OA ratio and exciton edge length (dot - 1.8 nm, dash - 2.4 nm, and solid - 3.0 nm).

4.4 Conclusion

Chirally imprinted perovskite nanoplatelets were synthesized with different halide and ligand compositions. The effect of the ligand shell's composition on the chiroptical signatures was investigated by using experimental and theoretical methods. We establish a relationship between the CD spectra and the surface ligand's orientation as well as on the density of the chiral ligands on the NPL. A nonlinear dependence was

found between the fraction of the chiral ligands and the measured CD intensity, suggesting that chiral imprinting saturates at high chiral ligand concentrations. Computational studies indicate that the point of saturation is determined by averaging of ligand configurations on the NPL surface. We find that the CD intensity is dictated by the perovskite exciton's spatial extent in the NPL plane, as the number of possible ligand binding orientations increases with exciton size. This study advances our understanding of chiral imprinting in perovskite nanostructures and establishes a model to describe ligand-induced chirality that can be applied to other ligand-capped NPL and NP systems. An expanded understanding of the underlying mechanisms for chiral imprinting should contribute to the continued development of novel chiral nanomaterials and their applications.

5. Control of Photoinduced Electron Transfer Yield with Polarized Light

This chapter is adapted from: Zhendian Zhang, Ye Jin, Peng Zhang, David N. Beratan. Control of Photoinduced Electron Transfer Yield with Polarized Light, in preparation,

Sun, K., Fang, C., Kang, M., Zhang, Z., Zhang, P., Beratan, D. N., ... & Kim, J. (2023). Quantum simulation of polarized light-induced electron transfer with a trapped-ion qutrit system. *arXiv preprint arXiv:2304.12247*. Sun, Fang and Kang contributed to the quantum simulation of the donor-acceptor model.

5.1 Introduction

Electron transfer reactions underpin energy conversion,¹¹⁴ signaling,¹¹⁵⁻¹¹⁸ and catalysis in living and non-living systems,¹¹⁹ and these reactions access a diversity of mechanisms.^{23,120} Bridge mediated superexchange,¹²¹ flickering resonance,^{122,123} adiabatic electron transfer, and incoherent hopping are accessible electron transfer mechanisms,¹²⁴ and new mechanisms continue to be uncovered in novel structures. For example, interferences between cavity-mediated and superexchange coupling pathways for electron transfer were recently predicted in polaritonic structures.¹²⁵ The “elementary” electron transfer steps in these reactions typically involve the coherent propagation of an

electron from one site to another in an activated complex. As such, quantum interferences among through-bond and through space electronic coupling pathways¹²⁶ are the norm: both chemical structure and fluctuations influence the interferences among the coupling routes.^{127–129} Earlier theoretical studies explored how the phase relationships among orbital amplitudes in the initially prepared state may influence electron transfer dynamics and yields, and how these phase relationships might be conveyed on the nanoscale.^{130,131} The nature of the initial electronic state can also influence electron transport mechanisms as its energy becomes nearly resonant with bridge localized excited states.¹³²

The effects of initial state preparation that we explore here arise from preparing a superposition of two nearly degenerate electronic states, ϕ_A and ϕ_B , to form the diabatic donor state $\Psi_D(t) = c_A(t)\phi_A + c_B(t)\phi_B$. The electronic state evolution from donor to acceptor may involve constructive or destructive coupling-pathway interference, depending on the mixing coefficients determined by the initial superposition determined by the light polarization ($c_A(0)$ and $c_B(0)$) and the coupling interactions between donor and acceptor. Here, we will explore how the initial state polarization, determined by polarization of the excitation pulse, may alter electronic dynamics.

Earlier studies have explored how electron transfer yield differences depend upon the phase relationships for the initially prepared state. The electronic dynamics

and yields were computed for a tight-binding analogue of a particle-in-a-ring state.¹³¹

The phase relationship among tight-binding sites in the ring influences the yield of electron transfer products. Further studies found that initial states with quantized linear or angular momentum could convey the momentum to the product state.¹³⁰

Here, we build multi-state quantum dynamical models that include a ground state, two orthogonally polarized donor excited states, and a charge-transfer product state with energy above the ground state but below the donor excited states. We examine the electronic dynamics following linearly or circularly polarized excitation. The electron transfer yield is found to be sensitive to the light polarization, molecular orientation and decoherence dynamics. We found that the yield of electron transfer can be controlled by the donor initial state prepared by LPL and CPL through the interference between two coupling pathways. The interference is found to be sensitive to the light polarization, molecular orientation and decoherence dynamics.

Directing electronic dynamics by selecting the polarization of the initial excitation is appealing for manipulating photoinduced electron transfer dynamics,^{133–136} plasmonic chemistry,¹³⁷ and artificial photosynthesis.^{138–140} Circularly polarized excitation has been found to influence electron transfer product yields in theoretical and experimental studies,^{131,141–144} and opportunities to use polarized excitation to direct charge and spin at the nanoscale, especially in chiral structures, is particularly compelling.^{20,85,141,145–147}

5.2 4-state model for polarization-dependent photoinduced electron transfer

We model the photoinduced ET using a 4-state effective Hamiltonian that includes a ground state (D_g), two near-degenerate donor localized excited states (D_1 and D_2), and an acceptor state (A). The light field couples the ground and the donor localized excited states; the donor excited states are coupled to the acceptor, and electron density is drained from the acceptor as described by eq. 5.1 and shown schematically in Figure. 21A.

$$H = \begin{pmatrix} E_{D_g} & \mu_1(t) & \mu_2(t) & 0 \\ \mu_1(t) & E_{D_1^*} & 0 & V_{D_1^*A} \\ \mu_2(t) & 0 & E_{D_2^*} & V_{D_2^*A} \\ 0 & V_{D_1^*A} & V_{D_2^*A} & E_A - \frac{i\Gamma}{2} \end{pmatrix}. \quad (5.1)$$

The electric transition dipole operator that couples the ground and electronic excited states is $\mu(t) = e \mathbf{r} \cdot \mathbf{E}(t)$, where $\mathbf{E}(t)$ is the time-dependent electric field and $e\mathbf{r}$ is the electric dipole operator. The excited state population is polarization dependent, and their contributions may depend on the molecular orientation and polarization of the electric field. As such, the system's time evolution will depend upon the light polarization and molecular orientation. Irreversible electronic dynamics is introduced by introducing an imaginary diagonal term on the acceptor, $-i\Gamma/2$, which drains density from the acceptor on the time scale of \hbar/Γ . Assuming the light propagates along the z-axis, and the electric field vector is in the xy-plane, the electric fields associated with circularly polarized light (CPL) and linearly polarized light (LPL) are:

$$\mathbf{E}_{CPL}(t) = E_0(\cos \omega t, \pm \sin \omega t, 0) \quad (5.2)$$

$$\mathbf{E}_{LPL}(\theta, t) = E_0(\cos \omega t \cos \theta, \cos \omega t \sin \theta, 0) \quad (5.3)$$

E_0 is the field strength, ω is the field's angular frequency, and θ defines the orientation of the linearly polarized light, measured with respect to the x-axis.

The model Hamiltonian of eq. 5.1 resembles photoinduced electron transfer between a metalloporphyrin donor (D) and a perylene-diimide acceptor (A). The 3D structure of a noncovalent porphyrin-PDI co-crystal structure was used to compute the electronic parameters of the DA assembly (see Appendix D) by time dependent density functional theory (TD-DFT) analysis. Non-covalent assemblies that weakly break the degeneracy of the porphyrin excited states are favorable for our studies. The computed excitation energies are robust with respect to changing the density functionals (results found with the ω B97X-D3 and cam-b3lyp functionals produce excitation energies that differ by 0.06 eV). The ω B97X-D3 functional was used with the def2-SVP basis set, and the computations were carried out using the Q-Chem program package¹⁴⁸. The computed transition dipole moments are $\mathbf{r}_1 = (4.58, 0, 0)$ *a.u.* and $\mathbf{r}_2 = (-0.61, 4.54, 0)$ *a.u.* for the zinc tetraphenyl porphyrin and PDI pair. The ground state energy E_{D_g} was set to 0, and the energies of the three other states are found in the TD-DFT analysis are $E_{D_1^*} = 3.89$ eV, $E_{D_2^*} = 3.93$ eV and $E_A = 3.01$ eV, based on the structure of an isolated DA pair taken from the crystal structure. Generalized Mulliken-Hush analysis^{149,150} was used to compute porphyrin excited state-PDI couplings of $V_{D_1^*A} =$

0.074 eV and $V_{D_2^*A} = 0.020$ eV which will be used in the simulation of ET dynamics unless specified. Figure. 21 shows the DA structure and a schematic energy-level diagram. Assuming a 8 μ J Gaussian line shape laser focused in a 1 mm area for 50 fs, the field strength (E_0) is 4×10^8 V/m, corresponding to peak donor ground state and excited state coupling of 0.1 eV. We use a Gaussian line shape for the exciting polarized light with pulse of 50 fs duration and 3.91 eV energy (the average of the two donor excited state energies). Γ was set to 0.5 eV, much larger than the DA coupling, so little electron returns to the donor after arrival on the acceptor.

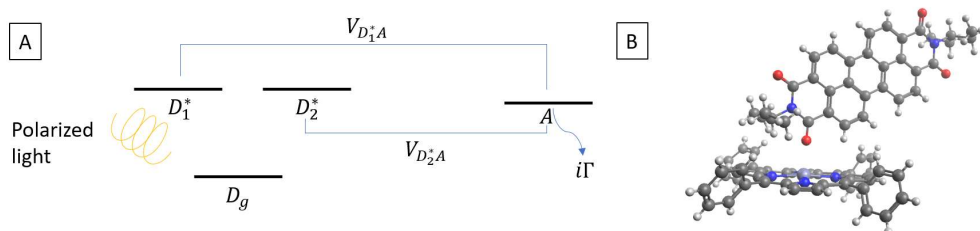


Figure 21: (A) Schematic illustration of the 4-state model for photoexcited electron transfer between two near-degenerate porphyrin excited state donor states and the PDI acceptor species. The donor is photoexcited by circularly or linearly polarized light, creating a superposition of the D_1^* and D_2^* states. The two diabatic donor photo-excited states are coupled electronically to the acceptor. An imaginary term on the acceptor irreversibility removes electron density from the system. (B). The structure of a porphyrin - perylene-diamide co-crystal determined by X-ray diffraction was used to compute the relevant electronic state energies and couplings.

When the porphyrin excited state consists of an incoherent mixture of the D_1^* and D_2^* states (the D_1 and D_2 interaction is much smaller than D-A coupling because their wave functions are polarized in almost orthogonal directions), the time evolution is a

simple sum of the two (independent) excited state time evolutions. The time evolution of a coherently excited donor superposition state, however, can manifest quantum interference effects as the wave function amplitude moved from the porphyrin to the PDI species. The time dependent electron transfer yield is defined as the integrated electron density that exits the system through the acceptor¹³¹:

$$Y(t) = \Gamma \int_0^t \rho_A(s) ds = 1 - \sum_i^4 \rho_i(t) \quad (5.4)$$

This yield corresponds, conceptually, to electron density that is trapped irreversibly on the acceptor, or is moved irreversibly from the PDI. $\rho_A(s)$ in eq. 2 is the acceptor's time dependent electron density, and is computed by solving the quantum Liouville equation using the Hamiltonian of eq. 5.1:

$$i\hbar \frac{\partial \rho}{\partial t} = [H, \rho] \quad (5.5)$$

The ultrafast electron transfer yield depends on initial light polarization, because the electron transfer yield is controlled by DA pathway interference which is determined by donor state wave functions prepared by light polarization. The difference in the time-dependent yields ($Y_1(t)$ and $Y_2(t)$) produced by two different light excitation polarizations is:

$$Y_D(t) = \frac{Y_1(t) - Y_2(t)}{Y_1(t) + Y_2(t)} \quad (5.6)$$

$Y_D(t)$ can vary from -1 to 1, reaching these limiting values when one of the yields is zero and the other yield is equal to one. We compute $Y_D(t)$ for left (L) and right (R)

circularly polarized excitation (L-CPL vs R-CPL) in the porphyrin plane, and for LPL with different polarization direction in the porphyrin plane.

We launched the quantum system from an initial excited state constructed from a superposition of the two near-degenerate porphyrin electronic excited states. The coherent superposition state of porphyrin locally excited states evolves into an incoherent mixture of porphyrin-localized excited states because of the interactions between the molecule and its surrounding (condensed phase) environment. The dissipation mainly includes relaxation and pure dephasing. The pure dephasing is the leading term^{151,152} that dampens the relative phase between excited state, we approximate the effects of the decoherence by introducing pure dephasing with the Lindblad operator to the quantum Liouville equation^{153,154}:

$$\dot{\rho} = -\frac{i}{\hbar}[H, \rho] + \sum_{j=1}^3 \gamma_j \left(W_j \rho W_j^\dagger - \frac{1}{2} \{W_j^\dagger W_j, \rho\} \right) \quad (5.7)$$

γ_j is the dephasing rate, and we assume these rates are the same for all three excited basis states (corresponding to an electron on D_1^* , D_2^* , or A). $W_1 = 1/$

$$\sqrt{2} \begin{pmatrix} 0 & 0 & 0 & 0 \\ 0 & 1 & 0 & 0 \\ 0 & 0 & 0 & 0 \\ 0 & 0 & 0 & 0 \end{pmatrix}, W_2 = 1/\sqrt{2} \begin{pmatrix} 0 & 0 & 0 & 0 \\ 0 & 0 & 0 & 0 \\ 0 & 0 & 1 & 0 \\ 0 & 0 & 0 & 0 \end{pmatrix} \text{ and } W_3 = 1/\sqrt{2} \begin{pmatrix} 0 & 0 & 0 & 0 \\ 0 & 0 & 0 & 0 \\ 0 & 0 & 0 & 0 \\ 0 & 0 & 0 & 1 \end{pmatrix}.^{155}$$

The quantum Liouville equation is numerically solved using the differential equation solver NDSolve implemented in *Mathematica* 13¹⁵⁶ for the zinc porphyrin-PDI assembly.

5.3 Results

5.3.1 Polarization dependent excited states

The donor-to-acceptor electronic dynamics from the photoexcited state (described in next section) depends on the relative phase and amplitude of the D_1^* and D_2^* components. We first examine the influence of the excitation light polarization on initially prepared donor states, while considering only the excitation process in isolation from electron transfer processes. As such, we define metrics to characterize the relative phase and amplitudes of the two donor-localized states. The excited state wave function after excitation, but prior to evolution onto the acceptor, is $(A_{D_g} e^{-i\phi_{D_g}}, A_{D_1^*} e^{-i\phi_{D_1^*}}, A_{D_2^*} e^{-i\phi_{D_2^*}}, 0)$, where $A_{D_g}, A_{D_1^*}, A_{D_2^*}$ are wave function amplitudes of the ground state and of the two donor excited states. $\phi_{D_g}, \phi_{D_1^*}$ and $\phi_{D_2^*}$ are the phases of the wave functions. The relative phase of the degenerate excited states is $\phi = \phi_{D_1^*} - \phi_{D_2^*}$, and the electron amplitude ratio $\lambda = A_{D_1^*}/A_{D_2^*}$. For simplicity, we use the above TD-DFT results but assume that the two diabatic excited states are degenerate and have orthogonal transition dipole moments with $E_{D_1^*} = E_{D_2^*} = 3.89 \text{ eV}$, $\mathbf{r}_1 = (4.58, 0, 0) \text{ a.u.}$, $\mathbf{r}_2 = (0, 4.58, 0) \text{ a.u.}$ That is, the zinc porphyrin diabatic state is not perturbed by the surrounding crystal. Numerical simulations with full TD-DFT obtained parameters in this paper will be discussed later.

When the acceptor and the sink are not at present, the electron density oscillates between the ground state and two excited states driven by the light. For circularly polarized excitation, ϕ and λ between two excited states oscillate with time (see Figure. 22A and 22B), depending on the handedness of the circularly polarized excitation. The relative phase of the two excited states is centered at $\pi/2$ and oscillates between 0 and π , and the phase differences (ϕ) for L-CPL and R-CPL are mirror images with respect to the line $\phi = \pi/2$. That is, there is a phase difference of π between the relative phase of the excited state wave functions for L-CPL and R-CPL, i.e., $\phi_R = \phi_L + \pi$ where ϕ_R is the relative phase excited by R-CPL and ϕ_L is the relative phase excited by L-CPL. This is anticipated from the sign difference of the perturbing fields (eq. 5.2). The handedness of the circularly polarized light has no effect on the electron amplitude ratio λ , since λ evolves identically for right and left circularly polarized light, namely $\lambda_R = \lambda_L$ (i.e., the blue and orange curves overlap in Figure. 22B). In the non-covalent zinc porphyrin – PDI structure, the donor excited state degeneracy is lifted somewhat by the environment of the crystal. As such, the transition dipole moments are not orthogonal, their magnitudes are not equal, and the relative phase ϕ and electron amplitude ratio λ differs from the degenerate case. To study the influence of non-degeneracy of donor excited states on the wave function, the excitation energies for two excited states are taken from the ZnP (in the ZnP – PDI pair) as 3.89 and 3.93 eV. Numerical simulations indicate that the choice of light frequency near the excitation energy has no influence on ϕ for the

ZnP-PDI for circularly polarized excitation (see Figure. D1). Therefore, we use the average excitation energy (3.91 eV) in our simulations and drive excitation of ZnP excited states. R- and L-CPL excitation establishes the relative phases and amplitudes $\cos\phi_R = -\cos\phi_L$ and $\lambda_R = \lambda_L$ (Figure. D1), as in the case of degenerate excited states.

We now examine how differences in the values of the transition dipole moments to the near degenerate donor excited states influence the electronic dynamics following photoexcitation. Our numerical simulations find that when the transition moments are different in magnitude ($|\mathbf{r}_1| \neq |\mathbf{r}_2|$), the phase relations between the two excited states are the same as when the length of transition moments are equal (Figure. D3), i.e, $\cos\phi_R = -\cos\phi_L$ for circularly polarized excitation. Since the light-matter Hamiltonian operator is the dot product of the electric field and the transition dipole moment, when $|\mathbf{r}_1| \neq |\mathbf{r}_2|$ the influence of circular polarized light on the system is equivalent to the influence of elliptically polarized light on a system with degenerate transitions. That is, more amplitude flows to the excited state with the larger transition dipole moment, but $\lambda_R = \lambda_L$ relation remains (Figure. D3 B). Finally, we explore the values of λ and ϕ when the transition dipole moments associated with the two excited states are not orthogonal. Defining the angle between the transition dipoles as η , circularly polarized light produces the phase relation $(\phi_R + \phi_L)/2 = \eta$ from numerical simulations (Figure. D4 A) for the orthogonally polarized transition dipoles is the special case where $\eta = \frac{\pi}{2}$.

However, when the transition dipoles are not orthogonal, the λ values for right and left circularly polarized light are not equal (Figure. D4 B).

The porphyrin has x- and y- polarized electronic transitions, and we consider excitation with linearly polarized light (LPL) oriented along one of these two directions. As such, the two transition dipole moments are: $\mu_1 = e|\mathbf{r}_1|E_0 \cos \theta \cos \omega t$ and $\mu_2 = e|\mathbf{r}_2|E_0 \cos \theta \cos \omega t$ (see eq. 5.3). The transition moment ratio is $\frac{|\mathbf{r}_1|}{|\mathbf{r}_2|} \cot \theta$, and is time independent. This transition moment ratio suggests that the phase difference for the excited states, ϕ , and the electron amplitude ratio, λ , is time independent for the two donor excited states. Linearly polarized excitation oriented as described populates either x- and y-polarized excited states. When $\vec{E}(t) \cdot \mathbf{r}_1$ and $\vec{E}(t) \cdot \mathbf{r}_2$ have the same sign, the two electronic excited states enter the wave function with the same sign, that is $\cos \phi = 1$. When $\vec{E}(t) \cdot \vec{\mu}_1$ and $\vec{E}(t) \cdot \vec{\mu}_2$ have opposite signs, the excited state components have opposite signs, that is $\cos \phi = -1$. When the donor excited states are not degenerate, LPL creates relative phase and electron amplitude ratios λ that are both time dependent (Figure. D2), and the values and oscillate around the values found when the donor excited states are degenerate. Larger excited state energy mismatches cause ϕ and λ to deviate further from the degenerate case, making control of the relative phase and amplitude ratios more challenging. The angle between the two transition dipole moments η and the magnitude of two transition dipole moments determine the electron amplitude ratio λ , where $\lambda = \frac{\cos \theta}{\cos(\eta-\theta)} \frac{|\mathbf{r}_1|}{|\mathbf{r}_2|}$. Due to the flexibility of choosing the LPL

polarization direction, the effect of donor transition dipole moments on electron transfer yield difference produced by LPL can be canceled by tuning the LPL polarization direction. In contrast, the angle between the transition dipole moments influences ϕ , which can alter the electron transfer yield for CPL excitation.

In summary, The CPL and LPL show the ability to tune the relative phase and amplitude ratio between donor excited states. In the next section, we explore how to maximize or minimize the electron transfer yield difference with the relative phase and amplitude ratio. For degenerate donor excited states with equal transition dipoles and orthogonal transition moments, circularly polarized light establishes excited states with $\phi_R + \phi_L = \pi$ and $\lambda_R = \lambda_L$. For degenerate excited states with equal transition dipoles, LPL establishes a time-independent relative phase and amplitude differences, depending on the light polarization. The relative phase and amplitude ratio relations is independent of the transition dipole magnitudes. If the angle between the donor transition dipole moments (η) is not equal to $\pi/2$, CPL creates donor excited states with $(\phi_R + \phi_L)/2 = \eta$ and $\lambda_R \neq \lambda_L$, while the relative phase and amplitude ratio relations is independent of η for linearly polarized light.

Breaking the degeneracy of the donor excitation energies does not change the phase relation among the two states for CPL excitation. However, the relative phase and amplitude ratio established by LPL is not time independent for non-degenerate excited states. In general, for linearly polarized excitation, the relative phase and amplitude ratio

can be tuned by changing the light polarization, which makes linearly polarized light an appealing tool to tune the electron transfer product yield.

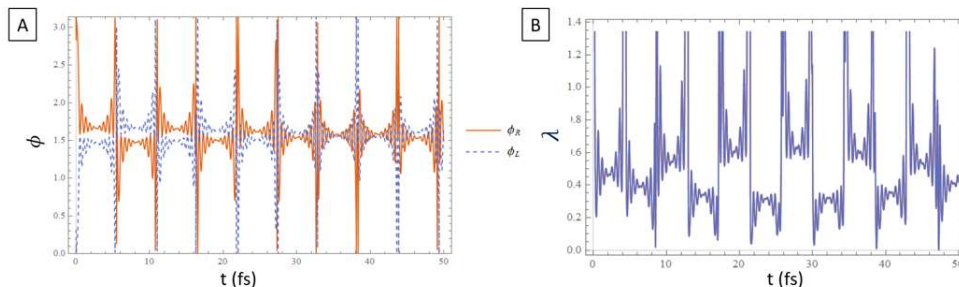


Figure 22: Time evolution of the phase and amplitude ratio following excitation of the degenerated donor excited states with CPL , at times prior to donor-to-acceptor propagation.(A) The relative ϕ is shown as function of time for circularly polarized excitation. Right and left circularly polarized light produce an excited states with opposite values of $\cos\phi$. (B) The electronic amplitude ratio r for the donor excited states following circularly polarized excitation is identical for L- and R-CPL.

5.3.2 Time evolution of coherently excited states without decoherence

Polarized excitation prepares and maintains the phase and amplitude ratios among the near degenerate excited states, as described above. We now explore how these superpositions influence donor-to-acceptor electronic propagation and electron through pathway interference in coherent limit by computing analytically electron transfer yields in the absence of decoherence (see Appendix D for detailed derivation). We assume the photoexcitation is much faster than electron transfer and no electron density left on the ground state, the initial wave function prepared by polarized light

excitation is $\psi(t = 0) = (0, 1, \lambda e^{i\phi}, 0)/\sqrt{1 + \lambda^2}$, where the vector show the element in the ground state, the two donor excited states, and the acceptor at time zero. We assume that the donor excited states are degenerate for simplicity. We define λ_1, ϕ_1 and λ_2, ϕ_2 as the electron amplitude ratio and phase for two independent sets of dynamics (for example, for λ_1, ϕ_1 may represent an excited state created R-CPL excitation and λ_2, ϕ_2 an excited state created by L-CPL excitation, or λ_1, ϕ_1 and λ_2, ϕ_2 may represent states created by two LPL excitations with different polarizations). The yield difference between these two sets of dynamics in the coherent limit is

$$Y_D(t) = \frac{-(\lambda_2 - \lambda_1)(\lambda_2 + \lambda_1)(x^2 - 1) - 2(1 + \lambda_1^2)\lambda_2 x \cos \phi_2 + 2(1 + \lambda_2^2)\lambda_1 x \cos \phi_1}{2 + \lambda_2^2 + \lambda_1^2 + (\lambda_2^2 + \lambda_1^2 + 2\lambda_1^2\lambda_2^2)x^2 + 2(1 + \lambda_1^2)\lambda_2 x \cos \phi_2 + 2(1 + \lambda_2^2)\lambda_1 x \cos \phi_1} \quad (5.8)$$

The coupling ratio for the two donor-to-acceptor interactions is $x = V_{D_2^*A}/V_{D_1^*A}$.

Eq. 8 indicates that the yield difference is independent of the acceptor state energy, donor-acceptor coupling strength and the rate of electron removal from the acceptor (Γ). The yield difference depends on the phases (ϕ_1 and ϕ_2), electronic amplitudes (λ_1 and λ_2), and coupling ratio (x) for the two degenerate donor excited states. When the relative phase equals 0 or π and the electron amplitude ratio (λ) is $1/x$ for one of the dynamics, the yield is zero because of destructive interference between the two coupling pathways, leading to $|Y_D| = 1$ when compared with dynamics with any other initial relative phase and the electron amplitude ratio.

As discussed above, circularly polarized excitation of degenerate donor excited states that have $\cos \phi_R = -\cos \phi_L$ and $\lambda_R = \lambda_L$. This produces the yields Y_{R-CPL} and Y_{L-CPL} , and eq. 5.9 gives

$$Y_D(CPL) = \frac{2 \cos \phi_R}{\frac{1}{x\lambda_R} + x\lambda_R}. \quad (5.9)$$

When $x\lambda_R = 1$, Y_D is the cosine of the phase angle, and Y_D reaches its maximum and minimum values of ± 1 when $\phi_R = 0$ and π , respectively. Although CPL has the potential to produce excited states with any phase and amplitude ratio, Figure. 2 shows, however, that the relative phase oscillates around the value $\pi/2$ and rarely reach 0 and π for CPL excitation such that the yield difference predicted with eq. 9 is small. Producing the maximum yield difference with circularly polarized light requires precise control of the laser pulse duration, such that when the laser is turned off, the resulting phase factor maximizes the electron transfer yield difference. If x is too large or too small ($x \gg 1$ or $x \ll 1$), suggesting that one of the DA pathway is much faster than the other one and two donor excited states are equally populated by CPL, i.e., $\lambda_R \approx 1$, the yield difference becomes zero as only one pathway dominates the ET and the pathway interference is negligible.

The time-independent ϕ and λ values produced by LPL depend strongly on the light polarization (θ), in contrast to the case for circularly polarized light. Therefore, Eq. 8 cannot be simplified for LPL excitation. Tuning the light polarization provides fine

control of the superposition created, i.e. any real value of λ and $\phi = 0$ or π . Eq. 5.8 indicates that Y_D varies from -1 to 1 for LPL excitation, depending on θ .

In the fully coherent regime, where the phase relationship between D_1^* and D_2^* is sustained, the largest possible value for the yield difference is 1 for both circularly and linearly polarized excitation. However, destructive interference for specific polarization direction can lead to no electron density arriving at the acceptor, thus halting electron transfer. In practice, such dramatic destructive interference effects are likely to be weakened by system-bath decoherence of the excited state superposition. In addition, instead of sequential processes of excitation and electron transfer assumed in this section, for the real molecule, the electron transfer starts when there is electron density on the donor excited states, i.e., electron transfer and excitation happens simultaneously. As the phase and amplitude ratio may vary during the excitation, especially for CPL, electron transfer during the excitation process is likely to weaken the overall yield difference. Breaking the degeneracy of donor excited states also affects the yield difference. We next explore decoherence, non-degenerate donor excited states, and simultaneous excitation and electron transfer effects on the dynamics.

5.3.3 Electron transfer driven by polarized light in a dissipative environment

Our analysis finds that the relative phase and the electron amplitude ratio of the prepared excited state largely determine the electron-transfer yield difference. We use

the 4-state model for the ZnP-PDI system described above. We study the influence of the dephasing rate, donor-acceptor coupling, and light polarization on the yield difference for both CPL and LPL excitation. The absolute value of yield difference decays to 0 at long time (all electron density eventually flows to the sink such that ET yield is 1 for any excitation), we analyze the yield difference at 1 ps, which is accessible in transient absorption experiments while remains considerable yield difference.¹⁵⁷ (The quantum superposition of the donor states will survive for a relatively short time, therefore this quantum effect impact the ET at short time and we short time ET.) We set the dephasing times $\tau = 1/\gamma$ 20 fs and 100 fs, to compare fast and slow donor excited state dephasing. For low temperature and in the crystal condition, these dephasing times are accessible. Donor-acceptor couplings of 0.074 and 0.02 eV were computed from GMH analysis as discussed above. We also computed the electron transfer yield differences for DA couplings that were 10% of and 5-fold more than these values to explore the DA coupling effect on the yield difference.

The electron transfer yield difference as a function of time for circularly polarized excitation is shown in Figure. 23. When the dephasing time is 100 fs (20 fs), the electron transfer yield difference is -1% (-0.56%) at 1 ps, which may not be detectable in experiment (for example TA). The negative yield difference suggests that the L-CPL excited electron transfer is slightly faster than R-CPL excited electron transfer. The yield oscillates with time, while for short dephasing time, the oscillation of yield difference is

dampened. Also, the yield difference is smaller with fast dephasing because of the dephasing reduced two pathway inference.

With 100 fs dephasing time, when the donor-acceptor coupling decreases to 10% of the computed value, the yield difference becomes -0.8% at 1 ps, which is 80% to the yield difference with the original coupling strength. This small decrease of yield difference as the donor-acceptor coupling is reduced in the limit where the electron transfer is slow compared to excitation is qualitatively consistent with the analytical analysis in eq.9 that the yield difference depends on the ratio of two donor-acceptor coupling instead of the absolute coupling strength. The reason that the yield difference has weak dependency on coupling strength in the numerical simulation is that the donor excited states are not degenerate in the simulation while they are assumed degenerate when deriving eq. 5.9. Also, the excitation and the electron transfer start simultaneously in the simulation while the electron transfer is decoupled from the excitation in eq. 5.9. When the donor-acceptor coupling grows by 5-fold stronger than the computed values (i.e., $V_{D_1^*A} = 0.37 eV$ and $V_{D_2^*A} = 0.1 eV$), the electron transfer yield difference shrinks to 0.014% at 1 ps, which is only 1% of yield difference with the original DA coupling. The reason that the yield difference drops quickly with 5-fold increased DA is that most electron density enters the sink during the excitation process when the DA coupling is too large. When the donor-acceptor couplings $V_{D_1^*A} = 0.074 eV$ and $V_{D_2^*A} = 0.02 eV$, electron density enters sink throughout 1ps, and when the DA coupling is reduced to

10%, the electron transfer is slow such that less than 2% electron density enters the sink at 1 ps. In contrast, when the DA coupling is increased by 5-fold, the electron transfer is finished and the electron is removed to the sink before excitation ends, such that the electron transfer yield excited by L-CPL and R-CPL has no difference.

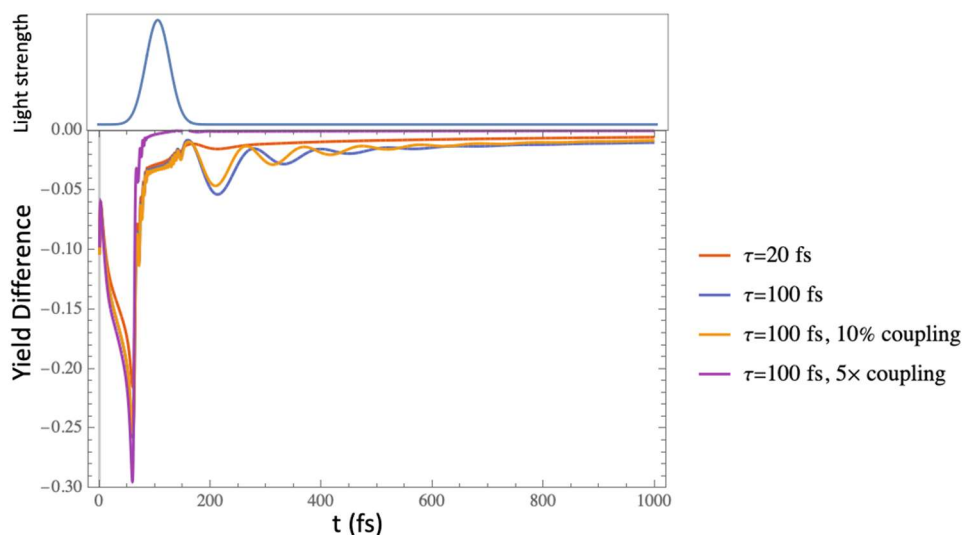


Figure 23: Electron transfer yield difference as a function of time for circularly polarized excitation. Orange, blue, yellow, and purple represent dephasing time of 20 fs, 100 fs, 100 fs and 100 fs, with DA couplings (0.074 and 0.02 eV) multiplied by 1, 1, 0.1 and 5, respectively.

The yield difference arising from LPL can be computed as a function of polarization. Figure. 24 shows the yield difference at 1 ps for two different LPL excitation orientations, with polarization directions θ_1 and θ_2 with respect to the x axis of the Zinc porphyrin ranging from 0 to π . When the dephasing time is 20 fs, the absolute value of yield difference reaches a maximum of 0.68 near $\theta_1 = 1.65$ or $\theta_2 = 1.65$

(approximately $\pi/2$). When the dephasing time increases to 100 fs, the yield difference maximum is 85%. The dependence of the yield difference on θ_1 and θ_2 is similar to what is found for short dephasing times, but the overall yield difference is larger. In the weak donor-acceptor coupling regime, the maximum yield difference is 95%, while in the large donor-acceptor coupling regime (5-fold larger than ZnP-PDI), the electron transfer yield difference decreases compared to the values reported in Figure. 24. Except θ_1 or θ_2 equal to 1.9, the yield difference at all other combinations of θ_1 and θ_2 is much smaller than weak donor-acceptor coupling regime because the electron transfer is almost finished during excitation. However, the maximum electron transfer yield difference is 75% when one of the LPL polarization direction $\theta = 1.9$, which is 88% of the yield difference found for the ZnP-DPI donor-acceptor couplings. A large yield difference is observed because when one of LPL has $\theta = 1.9$, due to the interference of two pathways, a large portion of electron density (70%) remains on the ground states until 1 ps such that the yield is small, while with all other θ values, the electron flows to the acceptor and the sink within excitation resulting electron transfer yield nearly 1. (see Figure. D5). Therefore, when comparing the yield between $\theta = 1.9$ and all other θ , a large yield difference is observed. Note that this specific θ value (1.9) that stops excitation depends on the donor excited states transition dipoles and donor-acceptor coupling ratio, and can be determined by scanning LPL polarization direction through numerical simulations or experiments.

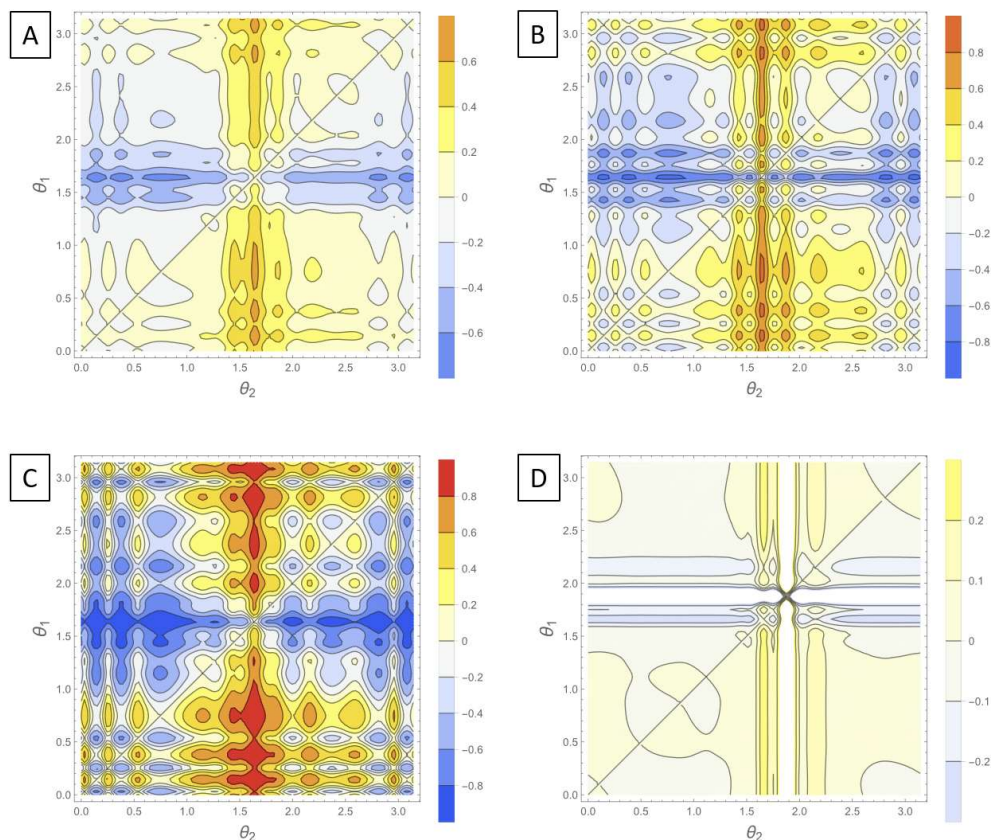


Figure 24: Electron transfer yield differences as a function of linear polarized light orientations θ_1 and θ_2 .(A). 20 fs dephasing time (B). 100 fs dephasing time (C). the DA coupling multiplied by 0.1, i.e., $V_{D_1^*A} = 0.0074$ eV and $V_{D_2^*A} = 0.0020$ eV and 100 fs dephasing time (D). the DA coupling multiplied by 5, i.e., $V_{D_1^*A} = 0.37$ eV and $V_{D_2^*A} = 0.1$ eV and 100 fs dephasing time. This figure shows the ability to achieve high yield difference under strong dephasing environment and control yield difference with LPL.

We computed the electron transfer yield differences for CPL and LPL excitation using energy and coupling parameters for the ZnP-PDI systems, including the effect of dephasing. Both LPL and CPL can produce electron transfer yield differences, but the magnitude of the yield differences produced by LPL is more than 70-fold larger than is

calculated for CPL due to the fine control of relative phase and amplitude difference of LPL by polarization direction. LPL also produces quantum dynamics that is more resistance to system-bath decoherence effect than is the case for circularly polarized light. When the dephasing time is decreased from 100 fs to 20 fs, the maximum yield difference of LPL is reduced from 85% to 68% which should be large enough to be observed in the experiment. Large donor-acceptor coupling leads to fast electron transfer during the excitation process, such that the yield of electron transfer for L-CPL and R-CPL, or LPL nearly 1 at 1 ps results in a small yield difference. However, even with large donor-acceptor couplings, there exists an LPL polarization direction that causes the electron to remain on the donor ground state as the result of interference, such that when compared with other polarization direction, the yield difference is still significant. Overall, large donor-acceptor coupling does not favor the yield difference.

5.3.4 Yield difference dependence on molecular orientation

We assumed that the CPL and LPL electric field vectors and the donor transition dipole moments are coplanar (in the xy plane) for the model system. Other relative polarizations are accessible. We next examine the dependence of electron transfer yield for CPL and LPL excitation as a function of the molecule-field orientation. We also explore the effects of orientation averaging of this orientation on the yield difference. The donor species orientation is described by an in-plane angle α and an out-of-plane

angle β . Assuming the light propagates along the z-axis, and the electric field vector is in the xy-plane, the in-plane angle rotates the ZnP with respect to the z-axis, and out-of-plane angle rotates ZnP with respect to the x-axis. When $\alpha = \beta = 0$, the electric field and transition dipole moment vectors are colinear. We varied α and β varied from 0 to π , and the computed yield differences for CPL or LPL excitation, assuming a 20 fs dephasing time (see Figure. D6). The electron transfer yield differences vary periodically as a function of α and β , and the results are even functions of α and β .

Orientation averaged yield differences under CPL and LPL illumination are shown in Table 4, assuming that α and β are Gaussian distributed with zero mean and standard deviation σ . The standard deviation represents the randomness of molecule orientation. The yield difference is independent of the in-plane distribution (angle α) for CPL excitation, and the yield difference is the same for all 3 standard deviation values studied. For CPL driven electron transfer, the yield difference decreases as the standard deviation of the out-of-plane angle (β) distribution grows. For LPL driven electron transfer, however, the yield difference decreases as the standard deviation for both of α and β grow. This finding indicates that the yield difference created by CPL illumination is independent to disorder of the in-plane light polarization, but is sensitive to the out of molecular plane orientation distribution. The yield difference initiated by LPL depends on both the in-plane and out-of-plane angle distribution functions as the in-plane and out-of-plane angles affect the relative phase and electron amplitude ratio of donor

excited states through the electric transition dipole operator in eq. 5.1. To achieve higher yield difference, aligning the chromophoric species to narrow molecular orientation distribution will be advantageous. Perfectly aligned molecules like in crystal would have same performance as single DA pair with up to 80% yield difference, while for DA pairs with Gaussian distributed orientation with 0.2 standard deviation, for example, DA molecules on a film with some constrains aligning the molecules, the yield difference would be less than 1%.

Table 4: The total electron transfer yield difference for different distributions of donor molecule orientations. $E_{D_1^*} = E_{D_2^*} = 3.89 \text{ eV}$, $E_A = 3.01 \text{ eV}$, $V_{D_1^*A} = 0.074 \text{ eV}$, $V_{D_2^*A} = 0.02 \text{ eV}$, $\Gamma = 0.5 \text{ eV}$, $\tau = 20 \text{ fs}$. σ is the standard deviation for a Gaussian distribution. The yield difference is averaged over the in-plane angle α and the out-of-plane angle β respectively for circularly (CPL) and linearly (LPL) polarized light.

<i>Yield Difference</i>				
σ	CPL (α)	CPL (β)	LPL (α)	LPL (β)
0.2	0.11%	1.1%	0.10%	0.78%
0.4	0.12%	0.6%	0.072%	0.31%
0.6	0.12%	0.073%	0.038%	0.18%

5.4 Discussion

We have explored the influence of polarized excitation on the electron transfer dynamics in coupled donor-acceptor electron transfer systems. The analysis focuses on donor structures with two near-degenerate donor excited electronic states. Interference between amplitude propagating from the superposition of the two near-degenerate excited depends on the polarization of the exciting light, its orientation with respect to the molecular chromophore, the ratio of the donor-acceptor couplings for the two near-degenerate excited states, and the dephasing rate. Left- and right-circularly polarized excitation prepares complex conjugate excited states, while the linearly polarized light prepares donor excited states with the same relative phase and time independent

amplitude ratio between excited states. In the coherent regime, a specific combination of relative phase (π) and electron amplitude ratio (the inverse of the DA couplings ratio), accessible by LPL or CPL donor excitation can produce full destructive interference among the electronic amplitude propagating from the two donor excited states, giving zero electron transfer yield.

Since the relative phase and electron amplitude ratio of the two excited states created by CPL oscillate with time, while the relative phase and amplitude ratio created by LPL do not depend on laser duration and can be fine tuned by LPL polarization direction, it is more challenging to employ CPL to lock the relative phase and electron amplitude ratio that maximize yield difference, and our and numerical results find that LPL is predicted to produce more than 70-fold larger yield differences compared to circularly polarized excitation with left- or right-circularly polarized light in the case of the Zn-PDI example. Dephasing relaxation destroys the phase relationship established between the two donor excited states over time, thus weakening the coupling pathway interference. The maximum of yield difference for the ZnP-PDI system with 100 fs dephasing is 85% for LPL excitation, which is much larger than the yield difference predicted for the electron transmission through chiral chains¹³¹ (up to 10%).

Orientation averaging the DA system is found to decrease electron transfer yield difference for both LPL and CPL significantly, so large yield differences are expected to be observed experimentally for well aligned DA ensembles. The largest electron transfer

yield differences arise from: (1) degenerate donor excited states (for both CPL and LPL excitation), (2) small dephasing rates (for both CPL and LPL), (3) weak donor-acceptor couplings, (4) oriented DA structures (for both CPL and LPL excitation) (5) proper choice of LPL polarization direction. Low temperature experiments are likely to reduce dephasing rates so that the coherent pathway interference effects persist over time. Our findings indicate the possibility of directing photoinduced electron transfer by manipulating the incident exciting light polarization, rather than by altering molecular structure.

We also utilized a trapped-ion qutrit to mimic the dynamics of electron transfer in a model molecular system. Our objective was to observe how the driving light's polarization affected these dynamics. By employing a qutrit, we were able to simulate the behavior of this three-level system using only single-qutrit operations on a single ion. This approach eliminated the need for multiple two-qubit operations on multiple ions, which would have been necessary with conventional qubits. Consequently, qutrit simulations yielded greater accuracy in our simulations. Through the qutrit simulation, we discovered that the process of photoexcitation and the population difference between the two degenerate states were influenced by the polarization of the exciting light. Additionally, we investigated the impact of phase differences between the two coupling pathways of electron transfer on its efficiency. We observed that destructive interference only occurred when the energy level difference was very small ($\leq 0.73\%$).

6. Conclusions

This dissertation presents theoretical studies on charge transfer and triplet energy transfer of QDs system through different medium, chiral imprinting on perovskite nano platelets and light polarization controlled coherent electron transfer.

In chapter 2, we built a discrete variable representation (DVR) method to numerically simulate the semiconductor nano particles. Using the DVR method, we examined the electron transfer between two CdSe quantum dots linked by a molecular linker. We constructed a model of quantum tunneling across interconnected quantum dots (QDs) by taking into account various parameters, including distance between QDs, QD size, the length and diameter of the bridge, the effective depths of potential, and effective mass. Our findings revealed that electronic coupling elevates as the QD size diminishes, given a constant edge-to-edge distance. The decay constant associated with electron transfer (ET) coupling originates from a combination of decay coupling occurring through the bridge and through the solvent. When it comes to a cylindrical bridge, its radius compared to the QD is significantly smaller (0.1nm versus several nm), leading to the dominance of through-solvent tunneling. The electron transfer occurring through the bridge can be overlooked when the bridge's size is significantly smaller than the QDs (where the ratio $R_{\text{bridge}}/R_{\text{QD}}$ is less than 0.15). However, if the bridge is

folded or multiple bridging chains exist between QDs, the contribution from the bridge would increase.

In chapter 3, we examined the distance dependence of charge transfer and triplet energy transfer. Different from chapter 2, that the QDs energy is independent on the QD-QD distance, varying the shell thickness perturbs the QD energy as the wave function has a non-negligible portion in the shell region (especially conduction band energy because of semi type II alignment of CdSe/CdS core/shell QDs). The effect on the reaction free energy should be considered. The experimental and computational results are consistent for ET, while the experimentally measured HT shows a much softer decay than calculated. The softness of measured HT rate may originate from the measurement and analysis quality. The TET rate shows a non-exponential behavior. Fitting to exponential resulted in a decay constant of 0.02 \AA^{-1} . Our calculations shown that the TET coupling decay constant is 0.5 \AA^{-1} . Using Marcus equation for TET, we found that with reorganization energy of 0.14 eV , the Frank-Condon factor exponentially increases as the shell thickness increases due to the decay of activation energy, which canceled the decrease of coupling. We also explored the dispersion effect of QD shell thickness. We found that in the experiment the deviation of QD shell thickness increases as the mean of shell thickness increases. For properties like electronic coupling that changes exponentially with the shell thickness, this change in the deviation of shell thickness will effectively soften the distance dependence of the coupling.

In chapter 4, we modeled the chiral imprinting of perovskite nanoplatelets. The influence of the composition of the ligand shell on chiroptical signatures was scrutinized using both experimental procedures and theoretical methodologies. We identified a correlation between the circular dichroism (CD) spectra and the orientation of the surface ligand, as well as the density of chiral ligands on the nanoplatelet (NPL). We observed a nonlinear association between the proportion of chiral ligands and the measured CD intensity, which indicates that chiral imprinting reaches saturation at elevated concentrations of chiral ligands. Computational examinations suggest that this saturation point is defined by the average of ligand arrangements on the NPL surface. We discovered that the intensity of the CD is regulated by the spatial extent of the perovskite exciton in the NPL plane, given that the count of potential ligand binding orientations escalates with exciton size. This research promotes our comprehension of chiral imprinting in perovskite nanostructures and sets up a model to illustrate ligand-induced chirality that can be extended to other ligand-encapsulated NPL and nanoparticle (NP) systems. A broader understanding of the fundamental processes behind chiral imprinting should benefit the ongoing development of innovative chiral nanomaterials and their uses.

In chapter 5, We've examined how polarized excitation impacts electron transfer dynamics in connected donor-acceptor electron transfer systems, with a particular emphasis on donor structures featuring two nearly identical donor excited electronic

states. The interference between amplitudes stemming from the superposition of the two closely aligned excited states is influenced by the polarization of the light used for excitation, its alignment with the molecular chromophore, the comparative donor-acceptor couplings for the two excited states, and the dephasing rate. Considering that the relative phase and electron amplitude ratio of the excited states produced by circularly polarized light vary over time, whereas those produced by linearly polarized light do not rely on laser duration and can be finely adjusted by changing its polarization direction, using circularly polarized light to stabilize the relative phase and electron amplitude ratio to maximize yield difference is more complex. According to our numerical results, linearly polarized light is anticipated to generate more than a 70-fold larger yield difference compared to circularly polarized excitation with left- or right-circularly polarized light in the case of the Zn-PDI example. Dephasing relaxation and orientation averaging the donor-acceptor system leads to a significant decrease in electron transfer yield difference for both linearly and circularly polarized light, hence large yield differences are likely to be experimentally observed for well-aligned donor-acceptor ensembles, with minimal dephasing rate. Our numerical simulations show that the yield difference produced by LPL is more resistant to dephasing than CPL. The most substantial electron transfer yield differences result from: degenerate donor excited states, minimal dephasing rates, weak donor-acceptor couplings, oriented donor-acceptor structures, and appropriate selection of linearly polarized light polarization

direction. Low temperature experiments are anticipated to reduce dephasing rates, thereby enabling coherent pathway interference effects to persist over time.

Appendix A

The effective mass changes across the heterojunction, so the boundary condition of the envelop function is both $\psi(r)$ and $\frac{1}{m^*} \frac{\partial}{\partial r} \psi(r)$ are continuous^{158,159}. The kinetic operator becomes

$$T = -\frac{\hbar^2}{2} \frac{\partial}{\partial r} \left(\frac{1}{m^*(r)} \frac{\partial}{\partial r} \right) \quad \text{A.1}$$

First, we consider $2N + 1$ grid points equally spaced in the range from a to b in 1D

$$x_i = a + i dx, \quad i = 1, \dots, 2N + 1 \quad \text{A.2}$$

where $dx = (b - a)/(2N + 1)$. A set of plane wave function is chosen as the basis

$$\phi_n(x) = \frac{1}{\sqrt{b-a}} e^{2\pi n \frac{x-a}{b-a}}, \quad n = 1, \dots, 2N + 1 \quad \text{A.3}$$

The kinetic energy matrix element for DVR is

$$\begin{aligned} T_{i,j} &= \left\langle i \left| -\frac{\hbar^2}{2} \frac{\partial}{\partial x} \left(\frac{1}{m^*(x)} \frac{\partial}{\partial x} \right) \right| j \right\rangle \\ &= -\frac{\hbar^2}{2} \sum_{k,k'} \left\langle i \left| \frac{\partial}{\partial x} \right| k \right\rangle \left\langle k \left| \frac{1}{m^*(x)} \right| k' \right\rangle \left\langle k' \left| \frac{\partial}{\partial x} \right| j \right\rangle \\ &= -\frac{\hbar^2}{2} \sum_k \frac{1}{m_k^*} \left\langle i \left| \frac{\partial}{\partial x} \right| k \right\rangle \left\langle k \left| \frac{\partial}{\partial x} \right| j \right\rangle \end{aligned} \quad \text{A.4}$$

The first derivative is calculated by plugging the plane waves

$$\left\langle i \left| \frac{\partial}{\partial x} \right| k \right\rangle = \frac{dx}{b-a} \sum_{n=-N}^N e^{2\pi n i \frac{x_i-a}{b-a}} \left(\frac{\partial}{\partial x} e^{2\pi n i \frac{x-a}{b-a}} \right)_{x=x_k}$$

$$= \begin{cases} -\frac{\pi}{b-a} \frac{(-1)^{i-k}}{\sin \frac{i-k}{2N+1} \pi} & i \neq k \\ 0 & i = k \end{cases} \quad \text{A.5}$$

Substituting eq. 5 into eq. 4 leads to

$$T_{i,j} = -\frac{\hbar^2}{2} (-1)^{i-j} \frac{\pi^2}{(b-a)^2} \sum_{k \neq i,j}^{2N+1} \frac{1}{m_k^*} \frac{1}{\sin \frac{i-k}{2N+1} \pi \sin \frac{k-j}{2N+1} \pi} \quad \text{A.6}$$

Here, $b \rightarrow \infty$ and $a \rightarrow -\infty$, so that $2N+1 = \frac{b-a}{dx} \rightarrow \infty$, but $i-j$ and dx are finite.

Eq. 6 becomes

$$\begin{aligned} T_{i,j} &= \lim_{N \rightarrow \infty} -\frac{\hbar^2}{2} (-1)^{i-j} \frac{\pi^2}{(b-a)^2} \sum_{k \neq i,j}^{2N+1} \frac{1}{m_k^*} \frac{1}{\sin \frac{i-k}{2N+1} \pi \sin \frac{k-j}{2N+1} \pi} \\ &= \lim_{N \rightarrow \infty} -\frac{\hbar^2}{2} (-1)^{i-j} \frac{\pi^2}{dx^2 (2N+1)^2} \sum_{k \neq i,j}^{2N+1} \frac{1}{m_k^*} \frac{(2N+1)^2}{(i-k)(k-j)\pi^2} \\ &= \lim_{N \rightarrow \infty} -\frac{\hbar^2}{2} \frac{(-1)^{i-j}}{dx^2} \sum_{k \neq i,j}^{2N+1} \frac{1}{m_k^* (i-k)(k-j)} \end{aligned} \quad \text{A.7}$$

The number of grid points is truncated to N_x , which contains the system we are interested in and the effective mass may vary in this region. The effective mass outside of the region $(0, (N_x - 1) dx)$ is assumed to be constant, this will correspond solvent with a free electron mass or surrounding semiconductor with its own effective mass.

$$T_{i,j} = -\frac{\hbar^2}{2} \frac{(-1)^{i-j}}{dx^2} \left(\sum_{k=-1}^{-\infty} \frac{1}{(i-k)(k-j)} + \sum_{k \neq i,j}^{N_x-1} \frac{1}{m_k^* (i-k)(k-j)} + \sum_{k=N_x}^{\infty} \frac{1}{(i-k)(k-j)} \right)$$

$$= \begin{cases} -\frac{\hbar^2 (-1)^{i-j}}{2 dx^2} \left(\sum_{k \neq i, j}^{N_x-1} \frac{1}{m_k^*} \frac{1}{(i-k)(k-j)} + \frac{1}{i-j} (\psi^{(0)}(N_x-i) - \psi^{(0)}(N_x-j) - \psi^{(0)}(1+i) + \psi^{(0)}(1+j)) \right) & i \neq j \\ -\frac{\hbar^2}{2 dx^2} \left(\sum_{k \neq i}^{N_x-1} -\frac{1}{m_k^* (i-k)^2} + (\psi^{(1)}(N_x-i) - \psi^{(1)}(1+i)) \right) & i = j \end{cases} \quad A.8$$

Appendix B

Synthesis of CdSe/CdS QDs and Preparation of CdSe/CdS QD-ACA, CdSe/CdS QD-MV and CdSe/CdS QD-PTZ Complexes

Cadmium oxide (CdO, 99.5%), selenium powder (Se, 100 mesh, 99.99%), Sulfur powder (S, 99.98%), 9-anthracenecarboxylic acid (ACA, 99%), tri-n-octylphosphine oxide (TOPO, 99%), tri-n-octylphosphine (TOP, 97%), oleic acid (OA, 90%), 1-octadecene (ODE, 90%), 1-octanethiol (OctSH, 99%), methyl viologen dichloride hydrate (MV²⁺, 98%) and phenothiazine (PTZ, 98%) and all other solvents were purchased from Sigma-Aldrich. N-octadecylphosphonic acid (ODPA, 99%) was purchased from PCI Synthesis. These chemicals were used without any further purification.

The synthesis of CdSe QDs was performed following the procedure reported in previous literature. 60 mg CdO, 3 g TOPO and 280 mg ODPA were mixed in a 25 mL three-neck bottle. After being vacuumed at 60 °C for 20 minutes, the mixture was heated to 360 °C under Argon flow. 1 mL TOP was injected into the system after the mixture became colorless solution. The temperature was raised back to 360 °C, and 0.5 mL Se TOP solution with 60 mg Se was quickly injected into the Cd solution. Once the color of the solution turned to orange, the reaction was quenched by intense cool air flow. After the temperature was decreased to 100 °C, methyl acetate was added to precipitate the CdSe QDs. The QDs were further washed with hexane and methyl acetate for once and

were finally dissolved in hexane with the concentration of 9.3×10^{-5} M. The CdSe QD solution was stored in a glove box with argon atmosphere for further use.

CdS shell was grown on CdSe QDs by the method reported in previous literature. 0.2 M cadmium oleate ($\text{Cd}(\text{OA})_2$) in ODE was prepared as Cd precursor solution. 257 mg CdO, 6.31 mL OA and 3.66 mL ODE were added to a 25-mL three-neck bottle. The mixture was placed in vacuum at 60 °C for 20 minutes and then in Argon flow for 10 minutes, after which the temperature was raised to 230 °C. After the solution turned colorless, the temperature was decreased to and maintained at 110 °C. 0.2 M OctSH in ODE was prepared as S precursor solution by dissolving 0.347 mL OctSH in 9.653 mL ODE through ultrasonication. For the growth of CdS shell, 100 nanomoles CdSe QDs solution was added to a 25-mL three-neck bottle with 5 mL ODE. Hexane and oxygen in the mixture were removed by vacuum, after which the temperature of the solution was raised to 240 °C. Desired amount of Cd and S precursor solutions in two separate syringes were then slowly injected into the CdSe QDs solution at a rate of 3 mL per hour by two syringe pumps. The amount of Cd and S precursor solutions used to achieve growth of certain shell thickness was calculated by estimated CdSe QD core size and the CdS shell lattice constant. After injection of Cd and S solutions, the temperature was further increased to and maintained at 310 °C for 10 minutes. Then the temperature of the solution was decreased to 100 °C with cool air flow, and excess methyl acetate was added to precipitate the CdSe/CdS QDs. The core-shell QDs were further washed

with hexane and methyl acetate and finally dispersed in 10 mL hexane with concentration of $\sim 1 \times 10^{-5}$ M. The core-shell QDs were stored in the glove box for further use.

The CdSe/CdS QD-ACA, CdSe/CdS QD-MV²⁺ and CdSe/CdS QD-PTZ complexes for TA experiment were prepared by adding 1 mg ACA/MV²⁺/PTZ powder into 1 mL CdSe/CdS QDs so that the amount of acceptor was much larger than that of QDs. The mixture was ultrasonicated for 2 hours, and excess undissolved powders were filtered out. The solvents in the solutions were then removed by air flow, and the complexes were re-dispersed in hexane in the glove box for experiments. For preparation of CdSe/CdS QD-ACA, CdSe/CdS QD-MV²⁺ and CdSe/CdS QD-PTZ complexes for determination of energy/electron/hole transfer rates with varying acceptor concentrations, varying amount of ACA/MV/PTZ in toluene solutions (1×10^{-3} M) was added to 1 mL CdSe/CdS QDs solutions. Specifically, the concentration ratios of ACA/PTZ to QDs were determined from UV-vis spectra of the solution, and the concentration ratios of MV²⁺ to QDs were determined from the calculation of amount of MV²⁺ added to the QDs solution and amount of QDs in solution, considering that the UV-vis spectra of MV²⁺ cannot be well resolved in the spectra window. The solutions were ultrasonicated for 2 hours, and the solvents were removed by air flow. Finally, the complexes along with free acceptors were re-dispersed in hexane in the glove box for TA/TRPL experiments.

Transient Absorption Spectroscopy Setups

The femtosecond transient absorption (TA) setup was based on a regenerative amplified Ti: Sapphire femtosecond laser system (Coherent Legend), which generates 800 nm fundamental pulse with pulse duration of 150 fs, repetition rate of 1 kHz and pulse energy of 2 mJ/pulse. The 800 nm pulse was directed through a 90:10 beam splitter. The 10% was focused onto a 2 mm thick sapphire crystal or a 3 mm thick CaF₂ crystal to generate the white light continuum as femtosecond TA probe. The spectra windows of the probe were 380-650 nm for CaF₂ crystal and 440-900 nm for sapphire crystal. The probe pulse was directed through a 70:30 beam splitter to generate the signal and reference probe. 1 W of 800 nm fundamental pulse was directed to an optical parametric amplifier (OPA). The signal output from the OPA was aligned with the remaining 800 nm fundamental at a BBO crystal to generate the 520 nm pump pulse through sum frequency generation. The remaining signal pulse and fundamental pulse after the BBO crystal were filtered out with a band pass filter. The pump went through a 500 Hz chopper as a modulation to provide the sample signals with and without the pump pulse excitation. A delay stage was applied for the pump pulse to adjust the time delay between the pump and the probe pulse. The pump and probe pulses were focused onto the sample with diameters of 400 μm and 100 μm , respectively. The power density of the pump pulse on the sample was 160 $\mu\text{J}/\text{cm}^2/\text{pulse}$. The probe beams were finally focused into optical fibers coupled with a visible spectrometer and a CMOS camera with

1024 elements. The data was collected with the Helios system from Ultrafast Systems, Inc. Instrument response function was fit to be a Gaussian function from the solvent response. The time window of the femtosecond TA is up to 1.6 ns with 200 fs time resolution.

For nanosecond TA experiments, the pump pulse from the femtosecond TA setups was directed and focused onto the sample without going through the 500 Hz chopper. The probe pulse was generated by a white light continuum laser (STM-2-UV, Leukos) with pulse duration of 0.5 ns and repetition rate of 2kHz. The data was collected by the EOS system from Ultrafast Systems, Inc.

The samples for the experiments were added to 1 mm thick quartz cuvettes (Starna) and were constantly stirred during TA experiment.

Steady State Photoluminescence Setups

Steady state photoluminescence experiments were performed on a Fluoromax fluorometer (Horiba Scientific). The excitation wavelength was set to be 400 nm for CdSe core QDs and 510 nm for CdSe/CdS core-shell QDs. The photoluminescence quantum yields of CdSe and CdSe/CdS QDs were determined with the method reported in previous literature with Coumarin 153 and Rhodamine 6G as standards, respectively. 1 cm cuvettes were applied for measurements.

Time-resolved Photoluminescence (TRPL) Setups

TRPL experiments were based on a mode-locked Ti:Sapphire laser (Tsunami oscillator, Spectra Physics). The wavelength of the output pulse was tuned to be 920 nm. The time duration of the pulse was 100 fs and the repetition rate was 80 MHz. The repetition rate was reduced by a pulse picker (Conoptics) to 20 MHz, 10 MHz and 1.43 MHz for the detection time windows of 50 ns, 100 ns and 700 ns, respectively. The pulse going through the pulse picker was directed to a BBO crystal to generate the 460 nm excitation pulse through second harmonic generation. The remaining 920 nm pulse was filtered out by band pass filters. The 460 nm pulse was directed to the sample, and the emission was collected into a monochromator (Acton Series, Princeton Instruments), by which the band edge exciton emission of the QDs was selected out. The emission going through the monochromator was collected and amplified by a microchannel-plate-photomultiplier tube (Hamamatsu R3809U-51) and analyzed by a time-correlated single photon counting (TCSPC) board (Becker & Hickel SPC 600). The instrument response function was measured to be a Gaussian function with FWHMs of 62 ps, 110 ps and 626 ps for 50 ns, 100 ns and 700 ns detection time windows, respectively. The absorption at 460 nm, the data collection time and the excitation pulse intensity were controlled to be the same for QDs with and without the acceptors.

Appendix C

Experimental Methods

Materials

Toluene anhydrous 99.8%, N,N-Dimethylformamide anhydrous 99.8%, Lead (II) Bromide 99.999%, Lead (II) Chloride 99.999%, Methylammonium Bromide >99%, and Methylamine Hydrochloride >98%, (*R*)-(+)- α -Methylbenzylamine 99%+, (*S*)-(-)- α -Methylbenzylamine 99%+, (*R*)-(+)-1-(1-Naphthyl)ethylamine 99%+, (*S*)-(-)-1-(1-Naphthyl)ethylamine 99%+ were purchased from Sigma-Aldrich. *S*-(+)-2-aminooctane 99%+ and *R*-(-)-2-aminooctane 99%+ were purchased from Thermo Scientific.

Synthesis of Precursor Salts

Chiral phenylethylammonium halide salts were synthesized by mixing equimolar amounts of the desired chiral amine and HBr or HCl in 15 mL of absolute ethanol. The reaction was stirred in an ice bath for 2 hours, then the solvent was removed via rotary evaporation until crystals were formed. The crystals were collected, recrystallized with chlorobenzene, and then vacuum filtered and washed several times with toluene. The product was kept in a desiccator overnight, then transferred into an Ar glove box.

Synthesis of Chiral NPLs

NPL synthesis was performed in an Ar glove box at room temperature. Solutions of each precursor were prepared in anhydrous DMF. The concentrations were chosen to reflect the desired ratio of reagents in the overall synthesis, for example 0.08M PbCl₂, 0.04M MAcl, 0.36M S- or R-PEACl (octylamine was used as a neat liquid). Equal volumes of PbX₂ and MAX solutions were added into a glass vial and mixed well. Octylamine was added in an equimolar amount to the PbX₂ added into the precursor mixture. The amount of PEAX solution in the precursor mixture was varied for the ligand concentrations studies, with PEA:OA molar ratios ranging from 1.6:1 to 6.75:1. For a single batch, 20 μ L of the precursor mixture were injected into 10 mL of anhydrous toluene while agitating with a vortex stirrer for 30 seconds. The NPLs were purified *via* centrifugation and resuspended in fresh anhydrous toluene to an optical density of approximately one.

Characterization

The spectral data were collected in a 1-cm quartz cuvette, which was pretreated with dimethyldichlorosilane to prevent adsorption of the perovskites onto the walls of the cuvette. To study optical transitions occurring beyond the spectral window of toluene, NPL suspensions in toluene were drop-cast onto clean quartz slides and dried under a gentle Ar flow. The material was layered until the desired optical density was achieved.

Absorption spectroscopy was performed using a Model 8453 Agilent spectrometer. CD spectra were measured using an Olis DSM 17 CD spectrometer with an integration time of 3 s and a bandwidth of 1 nm. Toluene was used as the background for all measurements.

For $^1\text{H-NMR}$ measurements NPLs were centrifuged into a pellet, then dried in a vacuum desiccator for 1 hour. The dry pellet was redispersed in toluene-d8 or dissolved in DMSO-d6, depending on the experiment. Spectra were taken on a Bruker Avance 400 spectrometer at 400 MHz with chemical shifts reported in parts per million (ppm) on the delta (δ) scale. Solvent peaks were used as a reference value at 2.50 ppm and 2.30 ppm for DMSO-d6 and toluene-d8 respectively.

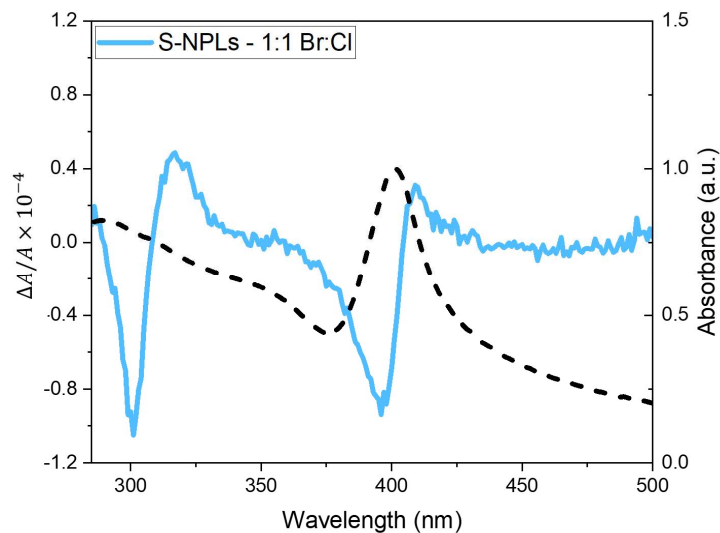


Figure C1. Absorbance (dashed line) and CD (solid line) of S-PEA-capped perovskite NPLs synthesized with a 1:1 ratio of Br an Cl anions.

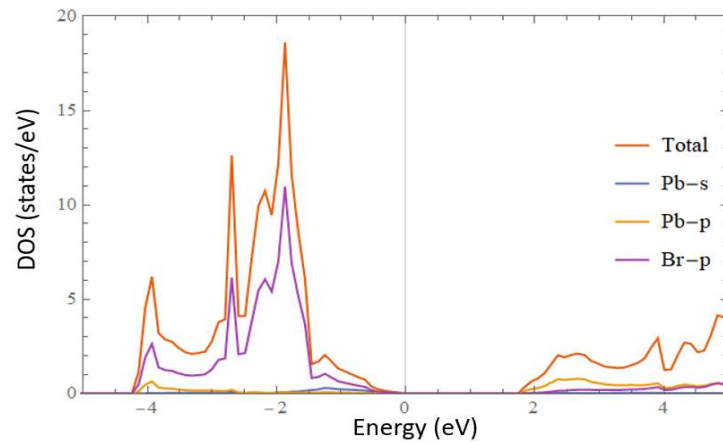


Figure C2. Total density of states (TDOS) and Partial density of states (PDOS) of bulk *MAPbBr₃* perovskite structure

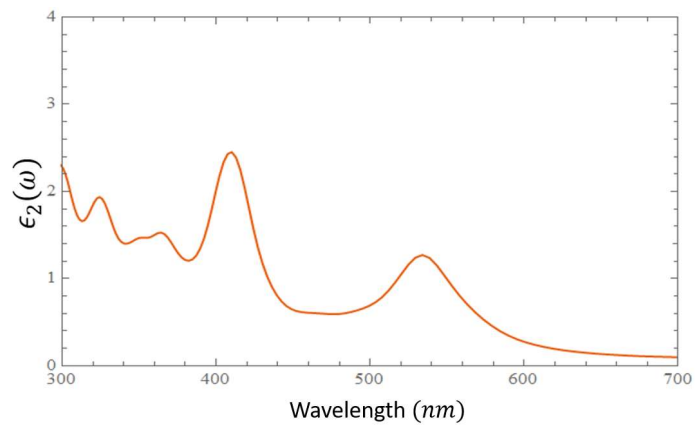


Figure C3. Imaginary $\epsilon_2(\omega)$ for *MAPbBr₃* NPL in vacuum.

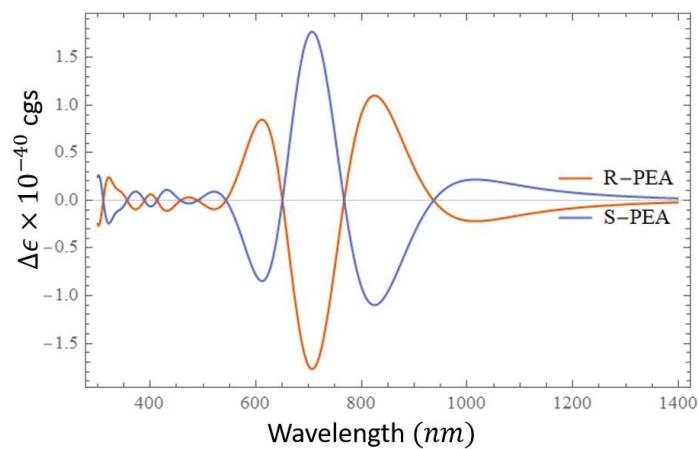


Figure C4. Simulated CD spectra using a $CsPbBr_3$ cluster model for single R- and S-PEA adsorbate imprinting.

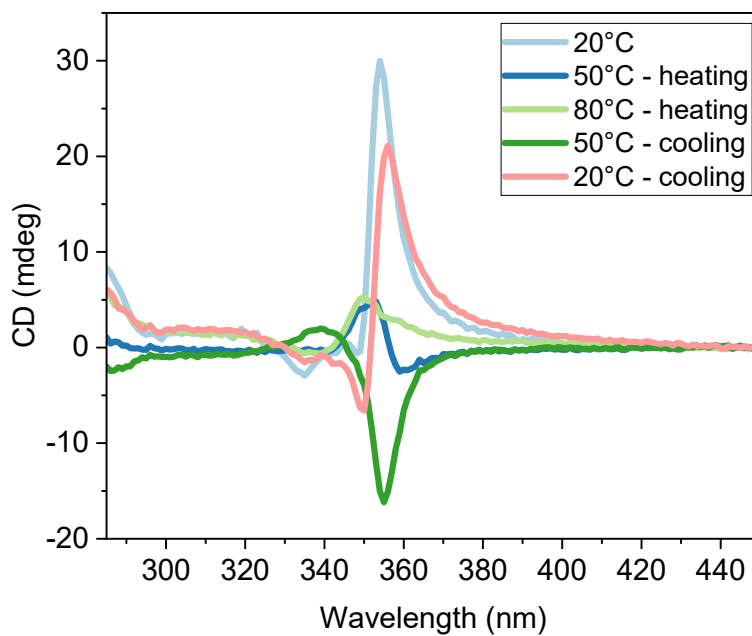


Figure C5. Temperature-dependent CD spectra of X=Cl NPLs with S-PEA ligands.

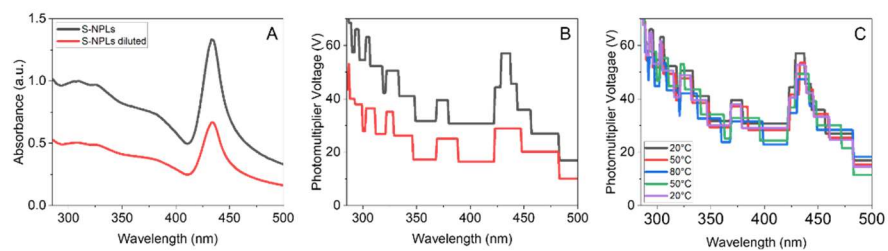
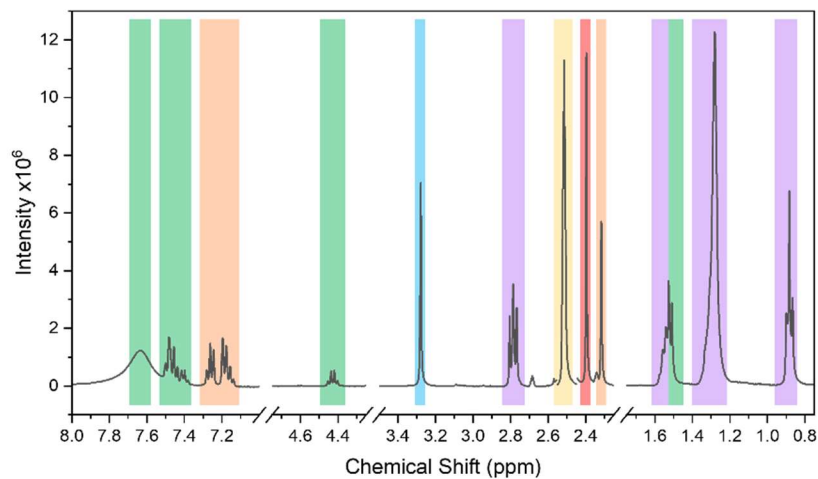


Figure C6. (A) Absorbance spectra of S-PEA capped X=Br NPLs with different concentrations. (B) Photomultiplier (PMT) voltage measurements for the same samples as panel A measured in a CD spectrometer. (C) PMT voltages for heated S-PEA capped X=Br NPLs.



Species	Peak position	Assignment
Octylamine	0.88	<i>a</i>
Octylamine	1.28	<i>b</i>
Octylamine	1.54	<i>c</i>
Octylamine	2.78	<i>d</i>
S-PEABr	1.52	<i>a</i>
S-PEABr	4.43	<i>b</i>
S-PEABr	7.46	<i>c</i>
S-PEABr	7.64	<i>d</i>
Toluene	2.32	<i>a</i>
Toluene	7.22	<i>b</i>
DMSO-d ₆	2.50	
MABr	2.40	
Water	3.28	

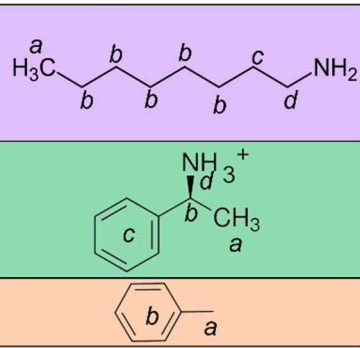


Figure C7. Assignment of ¹H-NMR peaks in a digested chiral NPL spectrum in DMSO-d₆.

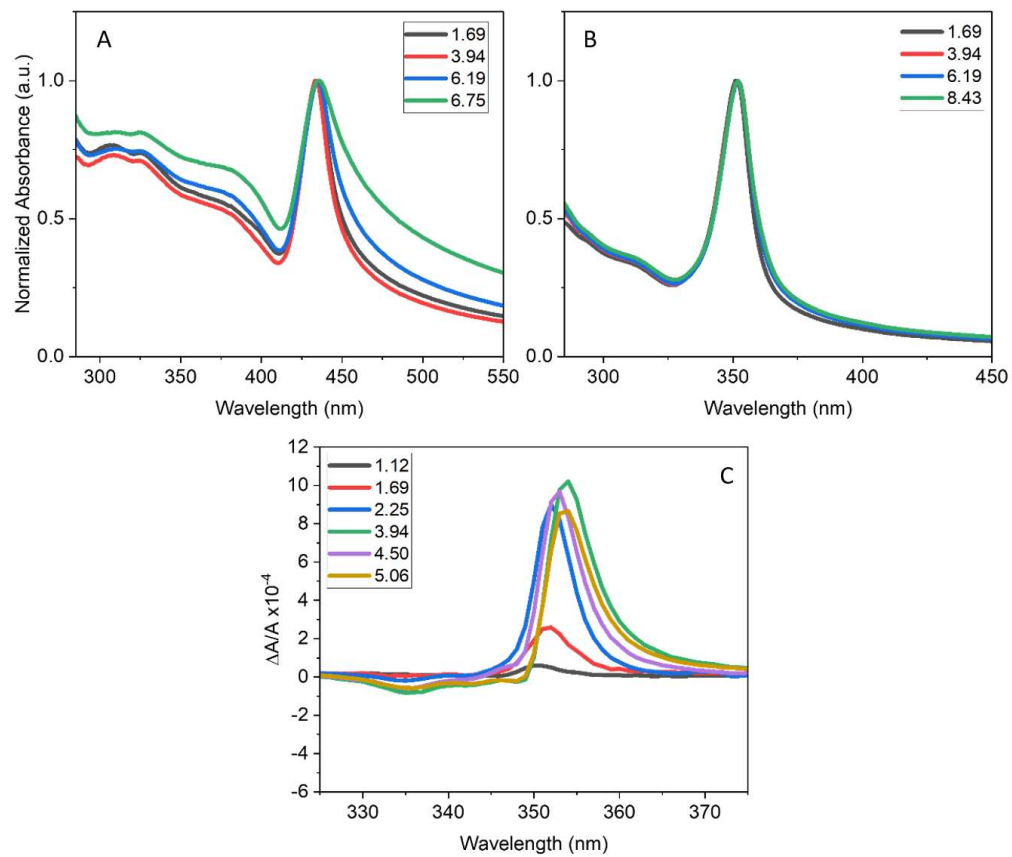


Figure C8. Absorbance of Br (a) and Cl (b) samples with high PEA content. CD of Cl PEA:OA variation experiment (c). Legends indicate the synthetic PEA:OA ratio.

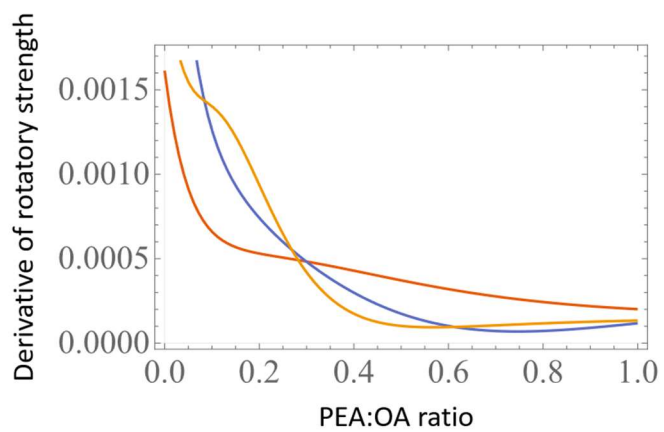


Figure C9. The derivative of rotational strength as a function of PEA:OA ratio for 3 exciton sizes: 3 by 3 (orange), 4 by 4 (blue) and 5 by 5 (yellow)

Appendix D

3-state model for light-polarization dependent electron transfer (D_1^* , D_2^* and A)

The Hamiltonian H (eq. 1) can be rewritten as

$$H = \begin{pmatrix} 0 & 0 & V_{D_1^*A} \\ 0 & 0 & V_{D_2^*A} \\ V_{D_1^*A} & V_{D_2^*A} & A - \frac{i\Gamma}{2} \end{pmatrix} \quad D.1$$

where $D_1^* = D_2^* = 0$. The quantum Liouville equation (eq. 7) describing the time evolution of the system has the solution (eq.8). Define a general initial wave function, $\psi(0) = (1, re^{i\phi}, 0)/\sqrt{1+r^2}$, the initial density matrix $\rho(0)$ is

$$\rho(0) = \begin{pmatrix} \frac{1}{r^2+1} & \frac{re^{i\phi}}{r^2+1} & 0 \\ \frac{re^{-i\phi}}{r^2+1} & \frac{r^2}{r^2+1} & 0 \\ 0 & 0 & 0 \end{pmatrix} \quad D.2$$

The time evolution operator is

$$U = e^{-\frac{iHt}{\hbar}} = \begin{pmatrix} U_{11} & U_{12} & U_{13} \\ U_{21} & U_{22} & U_{23} \\ U_{31} & U_{32} & U_{33} \end{pmatrix} \quad D.3$$

where the matrix elements are:

$$U_{11} = \frac{V_{D_2^*A}^2}{P} + 8V_{D_1^*A}^2 \left(\frac{e^{-\frac{1}{4}it(\sqrt{16P+Q^2}+Q)}}{Q(\sqrt{16P+Q^2}+Q) + 16P} - \frac{e^{\frac{1}{4}it(\sqrt{16P+Q^2}-Q)}}{Q(\sqrt{16P+Q^2}-Q) - 16P} \right) \quad D.4$$

$$U_{12} = U_{21} = V_{D_1^*A} V_{D_2^*A} \left(-\frac{8e^{\frac{1}{4}it(\sqrt{16P+Q^2}-Q)}}{Q(\sqrt{16P+Q^2}-Q)-16P} + \frac{8e^{-\frac{1}{4}it(\sqrt{16P+Q^2}+Q)}}{Q(\sqrt{16P+Q^2}+Q)+16P} - \frac{1}{P} \right) \quad D.5$$

$$U_{13} = U_{31} = -\frac{4iV_{D_1^*A}e^{-\frac{1}{4}itQ}\sin\left(\frac{1}{4}t\sqrt{16P+Q^2}\right)}{\sqrt{16P+Q^2}} \quad D.6$$

$$U_{22} = \frac{V_{D_1^*A}^2}{P} + 8V_{D_2^*A}^2 \left(\frac{e^{-\frac{1}{4}it(\sqrt{16P+Q^2}+Q)}}{Q(\sqrt{16P+Q^2}+Q)+16P} - \frac{e^{\frac{1}{4}it(\sqrt{16P+Q^2}-Q)}}{Q(\sqrt{16P+Q^2}-Q)-16P} \right) \quad D.7$$

$$U_{23} = U_{32} = -\frac{4iV_{D_2^*A}e^{-\frac{1}{4}itQ}\sin\left(\frac{1}{4}t\sqrt{16P+Q^2}\right)}{\sqrt{16P+Q^2}} \quad D.8$$

$$U_{33} = e^{-\frac{1}{4}itQ} \left(\cos\left(\frac{1}{4}t\sqrt{16P+Q^2}\right) + \frac{(-\gamma - 2ia)\sin\left(\frac{1}{4}t\sqrt{16P+Q^2}\right)}{\sqrt{16P+Q^2}} \right) \quad D.9$$

where $P = V_{D_1^*A}^2 + V_{D_2^*A}^2$, $Q = 2A - i\Gamma$ and we assume $\hbar = 1$ in atomic unit.

Plugging e^{-iHt} , we can get the electron density on the acceptor

$$p_A(t) = \frac{4\sqrt{16P+Q^2}\sqrt{16P+Q^2} \left(-1 + e^{\frac{1}{2}i\sqrt{16P+Q^2}t} \right) \left(-1 + e^{\frac{1}{2}i\sqrt{16P+Q^2}t} \right) (V_{D_2^2A} + V_{D_1A}e^{i\phi}) (V_{D_1A} + rV_{D_2^2A}e^{i\phi}) \exp\left(-\frac{1}{2} - \frac{1}{4}i\left(t\left(\sqrt{16P+Q^2} + \sqrt{16P+Q^2}\right) + 4\phi\right)\right)}{(r^2 + 1)(8a^2(r^2 + 16P) + 16a^4 + (r^2 - 16P)^2)} \quad D.10$$

The yield defined in the main text is thus

Lindblad equation for pure dephasing

We use the Lindblad equation to account for the pure dephasing effect due to the interaction with the environment. The Lindblad equation can be vectorized and solved numerically using differential equation solver:

$$\dot{\mathbf{x}} = A \cdot \mathbf{x} \tag{D.12}$$

where $A = -\frac{i}{\hbar}(H \otimes I_3 - I_3 \otimes H^\dagger) + \sum_{j=1}^3 \gamma_j (W \otimes W^\dagger - \frac{1}{2}(W_j^\dagger W \otimes I_3 + I_3 \otimes W_j^\dagger W))$, \otimes

is the Kronecker product, I_3 is 3 by 3 identity matrix, and \mathbf{x} is the vectorized density

matrix $\mathbf{x} = (\rho_{11}, \rho_{12}, \rho_{13}, \rho_{21}, \rho_{22}, \rho_{23}, \rho_{31}, \rho_{32}, \rho_{33})$

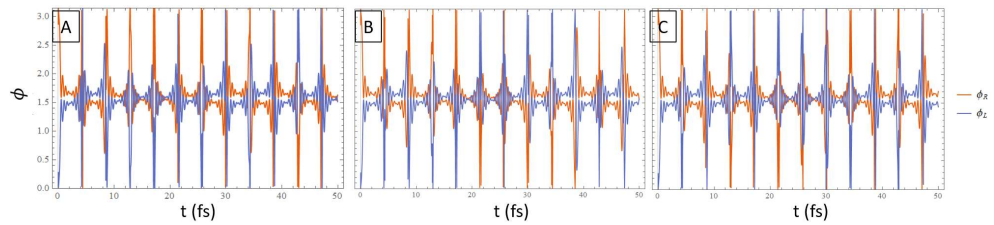


Figure D1 relative phase under CPL excitation with non-degenerate donor excited states $E_{D_1^*} = 3.89 \text{ eV}$, $E_{D_2^*} = 3.93 \text{ eV}$. Donor excitation transition dipoles are $(4.58, 0, 0) \text{ a.u.}$ and $(0, 4.58, 0) \text{ a.u.}$ (A) light frequency $\omega = 3.89 \text{ eV}$, (B) $\omega = 3.91 \text{ eV}$ (C) $\omega = 3.93 \text{ eV}$

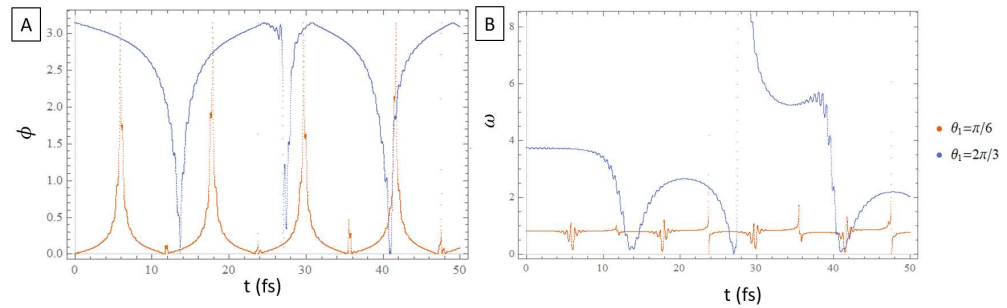


Figure D2 (A) phase and (B) electron density ratio under LPL excitation with non-degenerate donor excited states $E_{D_1^*} = 3.89 \text{ eV}$, $E_{D_2^*} = 3.93 \text{ eV}$, and $\omega = 3.91 \text{ eV}$. Donor excitation transition dipoles are $(4.58, 0, 0) \text{ a.u.}$ and $(0, 4.58, 0) \text{ a.u.}$

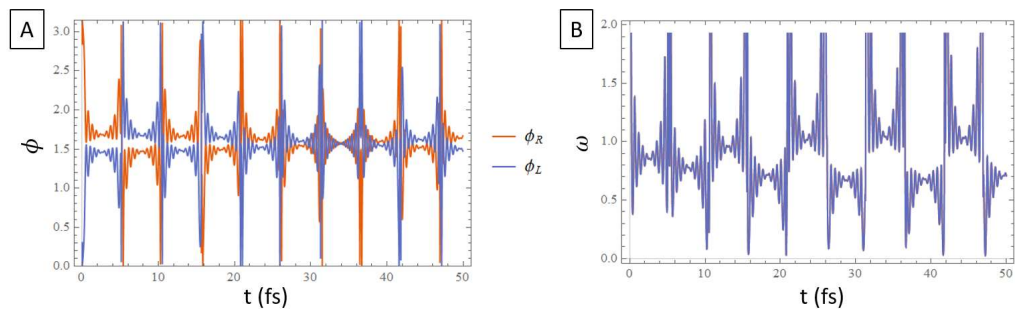


Figure D3 (A) phase and (B) electron density ratio under CPL excitation with degenerate donor excited states, the excitation transition dipoles are $(4.58, 0, 0)$ a.u. and $(0,5,0)$ a.u.

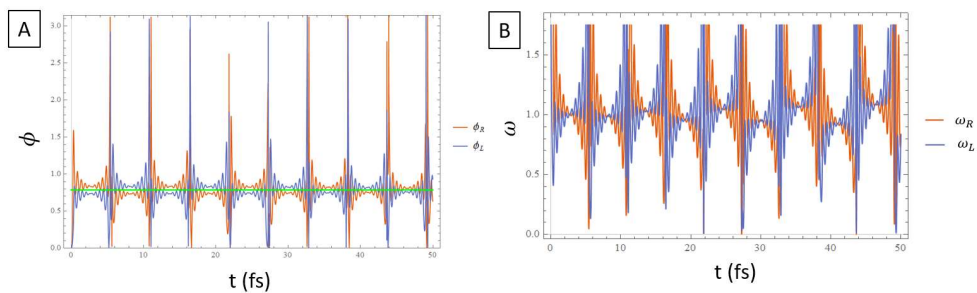


Figure D4 (A) phase and (B) electron density ratio under CPL excitation with angle between transition dipole moment $\pi/4$. Donor excitation transition dipoles are $(4.58, 0, 0)$ a.u. and $(3.24, 3.24, 0)$ a.u.

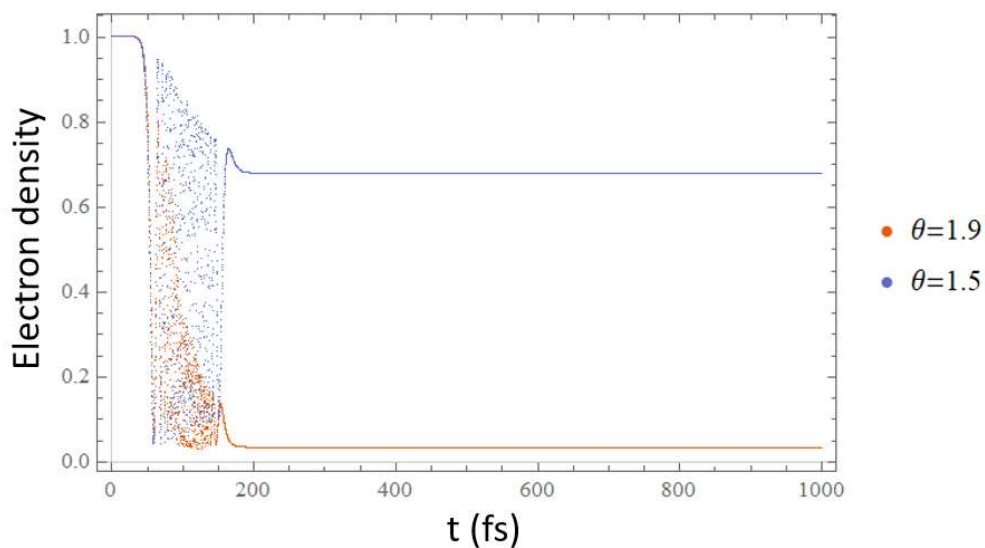


Figure D5 electron density of the donor ground state with donor-acceptor coupling 0.34 and 0.1 eV with 100 fs dephasing time excited by LPL with $\theta = 1.5$ and $\theta = 1.9$ respectively.

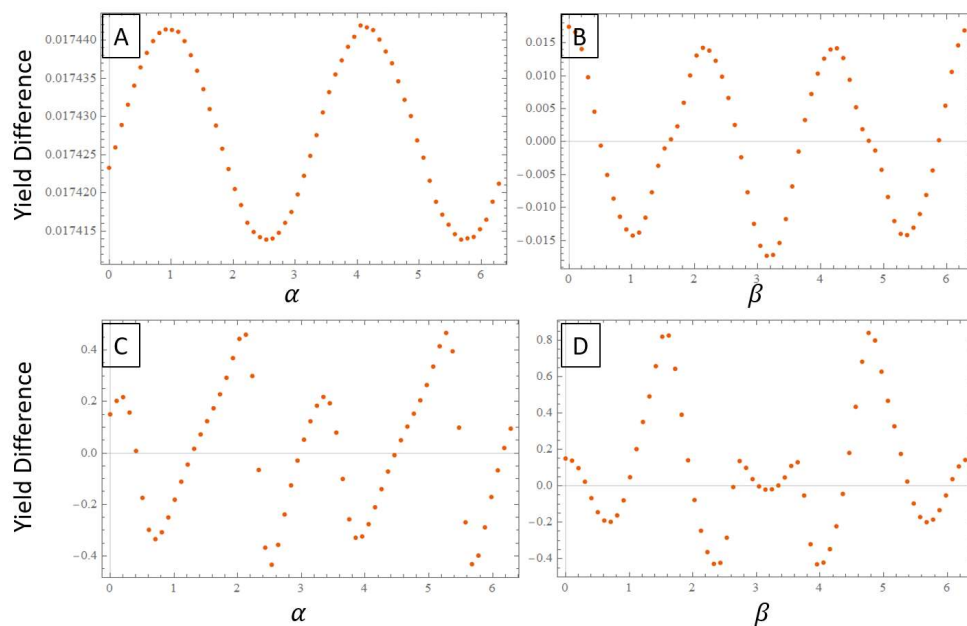


Figure D6 Yield difference under CPL and LPL excitation with respect to the orientation of the donor molecule with in-plane rotation angle α and out-of-plane rotation angle β . (A)-(B): CPL; (C)-(D): LPL.

References

- (1) Wasielewski, M. R. Photoinduced Electron Transfer in Supramolecular Systems for Artificial Photosynthesis. *Chem. Rev.* **1992**, *92*, 435–461.
- (2) Fleming, G. R.; Martin, J. L.; Breton, J. Rates of Primary Electron Transfer in Photosynthetic Reaction Centres and Their Mechanistic Implications. *Nature* **1988**, *333*, 190–192.
- (3) Zinth, W.; Wachtveitl, J. The First Picoseconds in Bacterial Photosynthesis - Ultrafast Electron Transfer for the Efficient Conversion of Light Energy. *ChemPhysChem* **2005**, *6*, 871–880.
- (4) Gray, H. B.; Winkler, J. R. Electron Transfer in Proteins. *Annu. Rev. Biochem.* 1996, pp 537–561.
- (5) Huang, L.; Regan, J. M.; Quan, X. Electron Transfer Mechanisms, New Applications, and Performance of Biocathode Microbial Fuel Cells. *Bioresour. Technol.* **2011**, *102*, 316–323.
- (6) Cave, R. J.; Newton, M. D. Calculation of Electronic Coupling Matrix Elements for Ground and Excited State Electron Transfer Reactions: Comparison of the Generalized Mulliken-Hush and Block Diagonalization Methods. *J. Chem. Phys.* **1997**, *106*, 9213–9226.
- (7) Difley, S.; Van Voorhis, T. Exciton/Charge-Transfer Electronic Couplings in Organic Semiconductors. *J. Chem. Theory Comput.* **2011**, *7*, 594–601.
- (8) Voityuk, A. A.; Rösch, N. Fragment Charge Difference Method for Estimating Donor-Acceptor Electronic Coupling: Application to DNA π -Stacks. *J. Chem. Phys.* **2002**, *117*, 5607–5616.
- (9) Marcus, R. A.; Sutin, N. Electron Transfers in Chemistry and Biology. *BBA Rev. Bioenerg.* 1985, pp 265–322.
- (10) De Mello Donegá, C. *Nanoparticles: Workhorses of Nanoscience*; 2014; Vol. 9783662448.
- (11) Bratschitsch, R.; Leitenstorfer, A. Quantum Dots: Artificial Atoms for Quantum Optics. *Nat. Mater.* **2006**, *5*, 855.
- (12) Harrison, P. *Quantum Wells, Wires and Dots*; 2016.

- (13) Kagan, C. R.; Lifshitz, E.; Sargent, E. H.; Talapin, D. V. Building Devices from Colloidal Quantum Dots. *Science* **2016**, 353.
- (14) Gong, X.; Yang, Z.; Walters, G.; Comin, R.; Ning, Z.; Beauregard, E.; Adinolfi, V.; Voznyy, O.; Sargent, E. H. Highly Efficient Quantum Dot Near-Infrared Light-Emitting Diodes. *Nat. Photonics* **2016**, 10, 253–257.
- (15) Yuan, M.; Liu, M.; Sargent, E. H. Colloidal Quantum Dot Solids for Solution-Processed Solar Cells. *Nat. Energy* **2016**, 1.
- (16) Kamat, P. V. Quantum Dot Solar Cells. Semiconductor Nanocrystals as Light Harvesters. *J. Phys. Chem. C* **2008**, 112, 18737–18753.
- (17) Sogabe, T.; Shen, Q.; Yamaguchi, K. Recent Progress on Quantum Dot Solar Cells: A Review. *J. Photonics Energy* **2016**, 6, 040901.
- (18) Xu, Y.-F.; Yang, M.-Z.; Chen, B.-X.; Wang, X.-D.; Chen, H.-Y.; Kuang, D.-B.; Su, C.-Y. A CsPbBr₃ Perovskite Quantum Dot/Graphene Oxide Composite for Photocatalytic CO₂ Reduction. *J. Am. Chem. Soc.* **2017**, 139, 5660–5663.
- (19) Carey, G. H.; Abdelhady, A. L.; Ning, Z.; Thon, S. M.; Bakr, O. M.; Sargent, E. H. Colloidal Quantum Dot Solar Cells. *Chem. Rev.* **2015**, 115, 12732–12763.
- (20) Bloom, B. P.; Liu, R.; Zhang, P.; Ghosh, S.; Naaman, R.; Beratan, D. N.; Waldeck, D. H. Directing Charge Transfer in Quantum Dot Assemblies. *Acc. Chem. Res.* **2018**, 51, 2565–2573.
- (21) Vokhmintcev, K. V.; Samokhvalov, P. S.; Nabiev, I. Charge Transfer and Separation in Photoexcited Quantum Dot-Based Systems. *Nano Today* **2016**, 11, 189–211.
- (22) Zhu, H.; Yang, Y.; Wu, K.; Lian, T. Charge Transfer Dynamics from Photoexcited Semiconductor Quantum Dots. *Annu. Rev. Phys. Chem.* **2016**, 67, 259–281.
- (23) Beratan, D. N. Why Are DNA and Protein Electron Transfer so Different? *Annual Review of Physical Chemistry*. 2019, pp 71–97.
- (24) Ponce, A.; Gray, H. B.; Winkler, J. R. Electron Tunneling through Water: Oxidative Quenching of Electronically Excited Ru(Tpy)₂²⁺ (Tpy) 2,2':6,2''-Terpyridine) by Ferric Ions in Aqueous Glasses at 77 K. **2000**.
- (25) Wenger, O. S.; Leigh, B. S.; Villahermosa, R. M.; Gray, H. B.; Winkler, J. R.

- Electron Tunneling through Organic Molecules in Frozen Glasses. *Science* **2005**, *307*, 99–102.
- (26) Graff, B. M.; Bloom, B. P.; Wierzbinski, E.; Waldeck, D. H. Electron Transfer in Nanoparticle Dyads Assembled on a Colloidal Template. *J. Am. Chem. Soc.* **2016**, *138*, 13260–13270.
- (27) Wang, H.; McNellis, E. R.; Kinge, S.; Bonn, M.; Cánovas, E. Tuning Electron Transfer Rates through Molecular Bridges in Quantum Dot Sensitized Oxides. *Nano Lett.* **2013**, *13*, 5311–5315.
- (28) Kaledin, A. L.; Lian, T.; Hill, C. L.; Musaev, D. G. An Infinite Order Discrete Variable Representation of an Effective Mass Hamiltonian: Application to Exciton Wave Functions in Quantum Confined Nanostructures. *J. Chem. Theory Comput.* **2014**, *10*, 3409–3416.
- (29) Zhu, H.; Song, N.; Lian, T. Controlling Charge Separation and Recombination Rates in CdSe/ZnS Type I Core–Shell Quantum Dots by Shell Thicknesses. *J. Am. Chem. Soc.* **2010**, *132*, 15038–15045.
- (30) Jackson, K. A.; Schröter, W. *Handbook of Semiconductor Technology: Electronic Structure and Properties of Semiconductors*; 2008; Vol. 1.
- (31) Gaiduk, A. P.; Pham, T. A.; Govoni, M.; Paesani, F.; Galli, G. Electron Affinity of Liquid Water. *Nat. Commun.* **2018**, *9*, 247.
- (32) Wu, Y. R.; Lin, Y. Y.; Huang, H. H.; Singh, J. Electronic and Optical Properties of InGaN Quantum Dot Based Light Emitters for Solid State Lighting. *J. Appl. Phys.* **2009**, *105*.
- (33) Yuan, S.; Chen, D.; Li, X.; Zhong, J.; Xu, X. In Situ Crystallization Synthesis of CsPbBr₃ Perovskite Quantum Dot-Embedded Glasses with Improved Stability for Solid-State Lighting and Random Upconverted Lasing. *ACS Appl. Mater. Interfaces* **2018**, *10*, 18918–18926.
- (34) Kibrıslı, O.; Erol, E.; Çelıkbilek Ersundu, M.; Ersundu, A. E. Robust CsPbBr₃ and CdSe / Dy³⁺/CdSe Quantum Dot Doped Glass Nanocomposite Hybrid Coupling as Color Converter for Solid-State Lighting Applications. *Chem. Eng. J.* **2021**, *420*, 130542.
- (35) Younis, M. R.; He, G.; Lin, J.; Huang, P. Recent Advances on Graphene Quantum Dots for Bioimaging Applications. *Frontiers in Chemistry*. 2020, p 530391.

- (36) Byers, R. J.; Hitchman, E. R. Quantum Dots Brighten Biological Imaging. *Progress in Histochemistry and Cytochemistry*. 2011, pp 201–237.
- (37) Kramer, I. J.; Sargent, E. H. Colloidal Quantum Dot Photovoltaics: A Path Forward. *ACS Nano*. 2011, pp 8506–8514.
- (38) Kovalenko, M. V. Opportunities and Challenges for Quantum Dot Photovoltaics. *Nature Nanotechnology*. 2015, pp 994–997.
- (39) Kamat, P. V. Quantum Dot Solar Cells. The next Big Thing in Photovoltaics. *Journal of Physical Chemistry Letters*. 2013, pp 908–918.
- (40) Pan, Z.; Mora-Seró, I.; Shen, Q.; Zhang, H.; Li, Y.; Zhao, K.; Wang, J.; Zhong, X.; Bisquert, J. High-Efficiency “Green” Quantum Dot Solar Cells. *J. Am. Chem. Soc.* **2014**, *136*, 9203–9210.
- (41) Mongin, C.; Garakyaraghi, S.; Razgoniaeva, N.; Zamkov, M.; Castellano, F. N. Direct Observation of Triplet Energy Transfer from Semiconductor Nanocrystals. *Science* **2016**, *351*, 369–372.
- (42) Gray, V.; Xia, P.; Huang, Z.; Moses, E.; Fast, A.; Fishman, D. A.; Vullev, V. I.; Abrahamsson, M.; Moth-Poulsen, K.; Lee Tang, M. CdS/ZnS Core-Shell Nanocrystal Photosensitizers for Visible to UV Upconversion. *Chem. Sci.* **2017**, *8*, 5488–5496.
- (43) Huang, Z.; Xu, Z.; Mahboub, M.; Li, X.; Taylor, J. W.; Harman, W. H.; Lian, T.; Tang, M. L. PbS/CdS Core-Shell Quantum Dots Suppress Charge Transfer and Enhance Triplet Transfer. *Angew. Chemie - Int. Ed.* **2017**, *56*, 16583–16587.
- (44) Luo, X.; Lai, R.; Li, Y.; Han, Y.; Liang, G.; Liu, X.; Ding, T.; Wang, J.; Wu, K. Triplet Energy Transfer from CsPbBr₃ Nanocrystals Enabled by Quantum Confinement. *J. Am. Chem. Soc.* **2019**, *141*, 4186–4190.
- (45) Piland, G. B.; Huang, Z.; Lee Tang, M.; Bardeen, C. J. Dynamics of Energy Transfer from CdSe Nanocrystals to Triplet States of Anthracene Ligand Molecules. *J. Phys. Chem. C* **2016**, *120*, 5883–5889.
- (46) Dexter, D. L. A Theory of Sensitized Luminescence in Solids. *J. Chem. Phys.* **1953**, *21*, 836–850.
- (47) Bai, S.; Zhang, P.; Beratan, D. N. Predicting Dexter Energy Transfer Interactions from Molecular Orbital Overlaps. *J. Phys. Chem. C* **2020**, *124*, 18956–18960.

- (48) Zhu, H.; Song, N.; Rodríguez-Córdoba, W.; Lian, T. Wave Function Engineering for Efficient Extraction of up to Nineteen Electrons from One CdSe/CdS Quasi-Type II Quantum Dot. *J. Am. Chem. Soc.* **2012**, *134*, 4250–4257.
- (49) Huang, J.; Huang, Z.; Jin, S.; Lian, T. Exciton Dissociation in CdSe Quantum Dots by Hole Transfer to Phenothiazine. *J. Phys. Chem. C* **2008**, *112*, 19734–19738.
- (50) Jia, Y.; Chen, J.; Wu, K.; Kaledin, A.; Musaev, D. G.; Xie, Z.; Lian, T. Enhancing Photo-Reduction Quantum Efficiency Using Quasi-Type II Core/Shell Quantum Dots. *Chem. Sci.* **2016**, *7*, 4125–4133.
- (51) Dworak, L.; Matylitsky, V. V.; Breus, V. V.; Braun, M.; Basché, T.; Wachtveitl, J. Ultrafast Charge Separation at the CdSe/CdS Core/Shell Quantum Dot/Methylviologen Interface: Implications for Nanocrystal Solar Cells. *J. Phys. Chem. C* **2011**, *115*, 3949–3955.
- (52) Zeng, P.; Kirkwood, N.; Mulvaney, P.; Boldt, K.; Smith, T. A. Shell Effects on Hole-Coupled Electron Transfer Dynamics from CdSe/CdS Quantum Dots to Methyl Viologen. *Nanoscale* **2016**, *8*, 10380–10387.
- (53) Jiang, Z. J.; Leppert, V.; Kelley, D. F. Static and Dynamic Emission Quenching in Core/Shell Nanorod Quantum Dots with Hole Acceptors. *J. Phys. Chem. C* **2009**, *113*, 19161–19171.
- (54) Chu, I. H.; Radulaski, M.; Vukmirovic, N.; Cheng, H. P.; Wang, L. W. Charge Transport in a Quantum Dot Supercrystal. *J. Phys. Chem. C* **2011**, *115*, 21409–21415.
- (55) Weidman, M. C.; Seitz, M.; Stranks, S. D.; Tisdale, W. A. Highly Tunable Colloidal Perovskite Nanoplatelets through Variable Cation, Metal, and Halide Composition. *ACS Nano* **2016**, *10*, 7830–7839.
- (56) Tyagi, P.; Arveson, S. M.; Tisdale, W. A. Colloidal Organohalide Perovskite Nanoplatelets Exhibiting Quantum Confinement. *J. Phys. Chem. Lett* **2015**, *6*, 41.
- (57) Stranks, S. D.; Eperon, G. E.; Grancini, G.; Menelaou, C.; Alcocer, M. J. P.; Leijtens, T.; Herz, L. M.; Petrozza, A.; Snaith, H. J. Electron-Hole Diffusion Lengths Exceeding 1 Micrometer in an Organometal Trihalide Perovskite Absorber. *Science* **2013**, *342*, 341–344.
- (58) Dong, Q.; Fang, Y.; Shao, Y.; Mulligan, P.; Qiu, J.; Cao, L.; Huang, J. Electron-Hole Diffusion Lengths > 175 Mm in Solution-Grown CH₃NH₃PbI₃ Single Crystals. *Science* **2015**, *347*, 967–970.

- (59) Dequillettes, D. W.; Koch, S.; Burke, S.; Paranj, R. K.; Shropshire, A. J.; Ziffer, M. E.; Ginger, D. S. Photoluminescence Lifetimes Exceeding 8 Ms and Quantum Yields Exceeding 30% in Hybrid Perovskite Thin Films by Ligand Passivation. *ACS Energy Lett.* **2016**, *1*, 438–444.
- (60) Xing, G.; Mathews, N.; Sun, S.; Lim, S. S.; Lam, Y. M.; Grätzel, M.; Mhaisalkar, S.; Sum, T. C. Long-Range Balanced Electron-and Hole-Transport Lengths in Organic-Inorganic CH₃NH₃PbI₃. *Science* **2013**, *342*, 344–347.
- (61) Yang, S.; Fu, W.; Zhang, Z.; Chen, H.; Li, C. Z. Recent Advances in Perovskite Solar Cells: Efficiency, Stability and Lead-Free Perovskite. *Journal of Materials Chemistry A*. 2017, pp 11462–11482.
- (62) NREL.Gov, Best Research-Cell Efficiency Chart, 2022.
<https://www.nrel.gov/pv/cell-efficiency.html>
- (63) Ochsenbein, S. T.; Krieg, F.; Shynkarenko, Y.; Rainò, G.; Kovalenko, M. V. Engineering Color-Stable Blue Light-Emitting Diodes with Lead Halide Perovskite Nanocrystals. *ACS Appl. Mater. Interfaces* **2019**, *11*, 21655–21660.
- (64) Lin, K.; Xing, J.; Quan, L. N.; de Arquer, F. P. G.; Gong, X.; Lu, J.; Xie, L.; Zhao, W.; Zhang, D.; Yan, C.; Li, W.; Liu, X.; Lu, Y.; Kirman, J.; Sargent, E. H.; Xiong, Q.; Wei, Z. Perovskite Light-Emitting Diodes with External Quantum Efficiency Exceeding 20 per Cent. *Nature* **2018**, *562*, 245–248.
- (65) Zhou, H.; Yuan, S.; Wang, X.; Xu, T.; Wang, X.; Li, H.; Zheng, W.; Fan, P.; Li, Y.; Sun, L.; Pan, A. Vapor Growth and Tunable Lasing of Band Gap Engineered Cesium Lead Halide Perovskite Micro/Nanorods with Triangular Cross Section. *ACS Nano* **2017**, *11*, 1189–1195.
- (66) Shi, Z. F.; Sun, X. G.; Wu, D.; Xu, T. T.; Tian, Y. T.; Zhang, Y. T.; Li, X. J.; Du, G. T. Near-Infrared Random Lasing Realized in a Perovskite CH₃NH₃PbI₃ Thin Film. *J. Mater. Chem. C* **2016**, *4*, 8373–8379.
- (67) Tang, B.; Dong, H.; Sun, L.; Zheng, W.; Wang, Q.; Sun, F.; Jiang, X.; Pan, A.; Zhang, L. Single-Mode Lasers Based on Cesium Lead Halide Perovskite Submicron Spheres. *ACS Nano* **2017**, *11*, 10681–10688.
- (68) George, J.; Halali, V. V.; Sanjayan, C. G.; Suvina, V.; Sakar, M.; Balakrishna, R. G. Perovskite Nanomaterials as Optical and Electrochemical Sensors. *Inorganic Chemistry Frontiers*. 2020, pp 2702–2725.

- (69) Ai, B.; Fan, Z.; Wong, Z. J. Plasmonic–Perovskite Solar Cells, Light Emitters, and Sensors. *Microsystems and Nanoengineering*. 2022, pp 1–28.
- (70) Billing, D. G.; Lemmerer, A. Synthesis and Crystal Structures of Inorganic–Organic Hybrids Incorporating an Aromatic Amine with a Chiral Functional Group. *CrystEngComm* **2006**, *8*, 686–695.
- (71) Ahn, J.; Lee, E.; Tan, J.; Yang, W.; Kim, B.; Moon, J. A New Class of Chiral Semiconductors: Chiral–Organic–Molecule–Incorporating Organic–Inorganic Hybrid Perovskites. *Mater. Horizons* **2017**, *4*, 851–856.
- (72) Chen, W.; Zhang, S.; Zhou, M.; Zhao, T.; Qin, X.; Liu, X.; Liu, M.; Duan, P. Two-Photon Absorption-Based Upconverted Circularly Polarized Luminescence Generated in Chiral Perovskite Nanocrystals. *J. Phys. Chem. Lett.* **2019**, *10*, 3290–3295.
- (73) Peng, Y.; Yao, Y.; Li, L.; Liu, X.; Zhang, X.; Wu, Z.; Wang, S.; Ji, C.; Zhang, W.; Luo, J. Exploration of Chiral Organic–Inorganic Hybrid Semiconducting Lead Halides. *Chem. - An Asian J.* **2019**, *14*, 2273–2277.
- (74) Chen, C.; Gao, L.; Gao, W.; Ge, C.; Du, X.; Li, Z.; Yang, Y.; Niu, G.; Tang, J. Circularly Polarized Light Detection Using Chiral Hybrid Perovskite. *Nat. Commun.* **2019**, *10*, 1–7.
- (75) Peng, Y.; Yao, Y.; Li, L.; Wu, Z.; Wang, S.; Luo, J. White-Light Emission in a Chiral One-Dimensional Organic–Inorganic Hybrid Perovskite. *J. Mater. Chem. C* **2018**, *6*, 6033–6037.
- (76) Yuan, C.; Li, X.; Semin, S.; Feng, Y.; Rasing, T.; Xu, J. Chiral Lead Halide Perovskite Nanowires for Second-Order Nonlinear Optics. *Nano Lett.* **2018**, *18*, 5411–5417.
- (77) Ma, J.; Fang, C.; Chen, C.; Jin, L.; Wang, J.; Wang, S.; Tang, J.; Li, D. Chiral 2D Perovskites with a High Degree of Circularly Polarized Photoluminescence. *ACS Nano* **2019**, *13*, 3659–3665.
- (78) Shi, Y.; Duan, P.; Huo, S.; Li, Y.; Liu, M. Endowing Perovskite Nanocrystals with Circularly Polarized Luminescence. *Adv. Mater.* **2018**, *30*, 1705011.
- (79) Georgieva, Z. N.; Bloom, B. P.; Ghosh, S.; Waldeck, D. H. Imprinting Chirality onto the Electronic States of Colloidal Perovskite Nanoplatelets. *Adv. Mater.* **2018**, *30*, 1800097.

- (80) Long, G.; Jiang, C.; Sabatini, R.; Yang, Z.; Wei, M.; Quan, L. N.; Liang, Q.; Rasmita, A.; Askerka, M.; Walters, G.; Gong, X.; Xing, J.; Wen, X.; Quintero-Bermudez, R.; Yuan, H.; Xing, G.; Wang, X. R.; Song, D.; Voznyy, O.; Zhang, M.; Hoogland, S.; Gao, W.; Xiong, Q.; Sargent, E. H. Spin Control in Reduced-Dimensional Chiral Perovskites. *Nature Photonics*. 2018, pp 528–533.
- (81) Kim, Y. H.; Zhai, Y.; Gauldin, E. A.; Habisreutinger, S. N.; Moot, T.; Rosales, B. A.; Lu, H.; Hazarika, A.; Brunecky, R.; Wheeler, L. M.; Berry, J. J.; Beard, M. C.; Luther, J. M. Strategies to Achieve High Circularly Polarized Luminescence from Colloidal Organic-Inorganic Hybrid Perovskite Nanocrystals. *ACS Nano* **2020**, *14*, 8816–8825.
- (82) Seo, I. C.; Lim, Y.; An, S. C.; Woo, B. H.; Kim, S.; Son, J. G.; Yoo, S.; Park, Q. H.; Kim, J. Y.; Jun, Y. C. Circularly Polarized Emission from Organic-Inorganic Hybrid Perovskites via Chiral Fano Resonances. *ACS Nano* **2021**, *15*, 13781–13793.
- (83) Zhao, Y.; Li, X.; Feng, J.; Zhao, J.; Guo, Y.; Yuan, M.; Chen, G.; Gao, H.; Jiang, L.; Wu, Y. Chiral 1D Perovskite Microwire Arrays for Circularly Polarized Light Detection. *Giant* **2022**, *9*, 100086.
- (84) Debnath, G. H.; Georgieva, Z. N.; Bloom, B. P.; Tan, S.; Waldeck, D. H. Using Post-Synthetic Ligand Modification to Imprint Chirality onto the Electronic States of Cesium Lead Bromide (CsPbBr₃) Perovskite Nanoparticles. *Nanoscale* **2021**, *13*, 15248–15256.
- (85) Bloom, B. P.; Graff, B. M.; Ghosh, S.; Beratan, D. N.; Waldeck, D. H. Chirality Control of Electron Transfer in Quantum Dot Assemblies. *J. Am. Chem. Soc.* **2017**, *139*, 9038–9043.
- (86) Mukhopadhyay, P.; Zuber, G.; Wipf, P.; Beratan, D. N. Contribution of a Solute's Chiral Solvent Imprint to Optical Rotation. *Angew. Chemie - Int. Ed.* **2007**, *46*, 6450–6452.
- (87) Goldsmith, M.-R.; George, C. B.; Zuber, G.; Naaman, R.; Waldeck, D. H.; Wipf, P.; Beratan, D. N. The Chiroptical Signature of Achiral Metal Clusters Induced by Dissymmetric Adsorbates. *Phys. Chem. Chem. Phys.* **2006**, *8*, 63–67.
- (88) Goldsmith, M. R.; Jayasuriya, N.; Beratan, D. N.; Wipf, P. Optical Rotation of Noncovalent Aggregates. *J. Am. Chem. Soc.* **2003**, *125*, 15696–15697.
- (89) Mukhopadhyay, P.; Wipf, P.; Beratan, D. N. Optical Signatures of Molecular Dissymmetry: Combining Theory with Experiment Sestereochemical Puzzles. *Acc.*

Chem. Res. **2009**, *42*, 809–819.

- (90) De Wergifosse, M.; Grimme, S. A Unified Strategy for the Chemically Intuitive Interpretation of Molecular Optical Response Properties. *J. Chem. Theory Comput.* **2020**, *16*, 7709–7720.
- (91) Kondru, R. K.; Wipf, P.; Beratan, D. N. Atomic Contributions to the Optical Rotation Angle as a Quantitative Probe of Molecular Chirality. *Science* **1998**, *282*, 2247–2250.
- (92) Moloney, M. P.; Gun'ko, Y. K.; Kelly, J. M. Chiral Highly Luminescent CdS Quantum Dots. *Chem. Commun.* **2007**, No. 38, 3900–3902.
- (93) Mukhina, M. V; Maslov, V. G.; Baranov, A. V; Fedorov, A. V; Orlova, A. O.; Purcell-Milton, F.; Govan, J.; Gun'ko, Y. K. Intrinsic Chirality of CdSe/ZnS Quantum Dots and Quantum Rods. *Nano Lett.* **2015**, *15*, 2844–2851.
- (94) Nakashima, T.; Kobayashi, Y.; Kawai, T. Optical Activity and Chiral Memory of Thiol-Capped CdTe Nanocrystals. *J. Am. Chem. Soc.* **2009**, *131*, 10342–10343.
- (95) Elliott, S. D.; Moloney, M. P.; Gun'ko, Y. K. Chiral Shells and Achiral Cores in CdS Quantum Dots. *Nano Lett.* **2008**, *8*, 2452–2457.
- (96) Choi, J. K.; Haynie, B. E.; Tohgha, U.; Pap, L.; Elliott, K. W.; Leonard, B. M.; Dzyuba, S. V; Varga, K.; Kubelka, J.; Balaz, M. Chirality Inversion of CdSe and CdS Quantum Dots without Changing the Stereochemistry of the Capping Ligand. *ACS Nano* **2016**, *10*, 3809–3815.
- (97) Zhou, R.; Wei, K. Y.; Zhao, J. S.; Jiang, Y. B. Alternative Chiral Thiols for Preparation of Chiral CdS Quantum Dots Covered Immediately by Achiral Thiols. *Chem. Commun.* **2011**, *47*, 6362–6364.
- (98) Zhou, Y.; Marson, R. L.; Van Anders, G.; Zhu, J.; Ma, G.; Ercius, P.; Sun, K.; Yeom, B.; Glotzer, S. C.; Kotov, N. A. Biomimetic Hierarchical Assembly of Helical Supraparticles from Chiral Nanoparticles. *ACS Nano* **2016**, *10*, 3248–3256.
- (99) Gao, X.; Zhang, X.; Deng, K.; Han, B.; Zhao, L.; Wu, M.; Shi, L.; Lv, J.; Tang, Z. Excitonic Circular Dichroism of Chiral Quantum Rods. *J. Am. Chem. Soc.* **2017**, *139*.
- (100) Kuznetsova, V.; Gromova, Y.; Martinez-Carmona, M.; Purcell-Milton, F.; Ushakova, E.; Cherevkov, S.; Maslov, V.; Gun'ko, Y. K. Ligand-Induced Chirality and Optical Activity in Semiconductor Nanocrystals: Theory and Applications.

Nanophotonics **2020**, *10*, 797–824.

- (101) Ben-Moshe, A.; Teitelboim, A.; Oron, D.; Markovich, G. Probing the Interaction of Quantum Dots with Chiral Capping Molecules Using Circular Dichroism Spectroscopy. *Nano Lett.* **2016**, *16*, 7467–7473.
- (102) Tohgha, U.; Deol, K. K.; Porter, A. G.; Bartko, S. G.; Choi, J. K.; Leonard, B. M.; Varga, K.; Kubelka, J.; Muller, G.; Balaz, M. Ligand Induced Circular Dichroism and Circularly Polarized Luminescence in CdSe Quantum Dots. *ACS Nano* **2013**, *7*, 11094–11102.
- (103) Gao, X.; Zhang, X.; Zhao, L.; Huang, P.; Han, B.; Lv, J.; Qiu, X.; Wei, S. H.; Tang, Z. Distinct Excitonic Circular Dichroism between Wurtzite and Zinblende CdSe Nanoplatelets. *Nano Lett.* **2018**, *18*, 6665–6671.
- (104) Varga, K.; Tannir, S.; Haynie, B. E.; Leonard, B. M.; Dzyuba, S. V.; Kubelka, J.; Balaz, M. CdSe Quantum Dots Functionalized with Chiral, Thiol-Free Carboxylic Acids: Unraveling Structural Requirements for Ligand-Induced Chirality. *ACS Nano* **2017**, *11*, 9846–9853.
- (105) Kuznetsova, V. A.; Mates-Torres, E.; Prochukhan, N.; Marcastel, M.; Purcell-Milton, F.; O'Brien, J.; Visheratina, A. K.; Martinez-Carmona, M.; Gromova, Y.; Garcia-Melchor, M.; Gun'Ko, Y. K. Effect of Chiral Ligand Concentration and Binding Mode on Chiroptical Activity of CdSe/CdS Quantum Dots. *ACS Nano* **2019**, *13*, 13560–13572.
- (106) Yan, L.; Jana, M. K.; Sercel, P. C.; Mitzi, D. B.; You, W. Alkyl-Aryl Cation Mixing in Chiral 2D Perovskites. *J. Am. Chem. Soc.* **2021**, *143*, 18114–18120.
- (107) Hassan, Y.; Park, J. H.; Crawford, M. L.; Sadhanala, A.; Lee, J.; Sadighian, J. C.; Mosconi, E.; Shivanna, R.; Radicchi, E.; Jeong, M.; Yang, C.; Choi, H.; Park, S. H.; Song, M. H.; De Angelis, F.; Wong, C. Y.; Friend, R. H.; Lee, B. R.; Snaith, H. J. Ligand-Engineered Bandgap Stability in Mixed-Halide Perovskite LEDs. *Nature* **2021**, *591*, 72–77.
- (108) Stelmakh, A.; Aebli, M.; Baumketner, A.; Kovalenko, M. V. On the Mechanism of Alkylammonium Ligands Binding to the Surface of CsPbBr₃ Nanocrystals. *Chem. Mater.* **2021**, *33*, 5962–5973.
- (109) Quarta, D.; Imran, M.; Capodilupo, A. L.; Petralanda, U.; Van Beek, B.; De Angelis, F.; Manna, L.; Infante, I.; De Trizio, L.; Giansante, C. Stable Ligand Coordination at the Surface of Colloidal CsPbBr₃ Nanocrystals. *J. Phys. Chem. Lett.*

2019, 10, 3715–3726.

- (110) Balan, A. D.; Olshansky, J. H.; Horowitz, Y.; Han, H. L.; O'Brien, E. A.; Tang, L.; Somorjai, G. A.; Alivisatos, A. P. Unsaturated Ligands Seed an Order to Disorder Transition in Mixed Ligand Shells of CdSe/CdS Quantum Dots. *ACS Nano* **2019**, *13*, 13784–13796.
- (111) Widmer-Cooper, A.; Geissler, P. L. Ligand-Mediated Interactions between Nanoscale Surfaces Depend Sensitively and Nonlinearly on Temperature, Facet Dimensions, and Ligand Coverage. *ACS Nano* **2016**, *10*, 1877–1887.
- (112) Baranowski, M.; Galkowski, K.; Surrente, A.; Urban, J.; Kłopotowski, Ł.; Mac, S.; Kennedy Maude, D.; Ben Aich, R.; Boujdaria, K.; Chamarro, M.; Testelin, C.; Nayak, P. K.; Dollmann, M.; James Snaith, H.; John Nicholas, R.; Plochocka, P. Giant Fine Structure Splitting of the Bright Exciton in a Bulk MAPbBr₃ Single Crystal. **2019**.
- (113) Droseros, N.; Longo, G.; Brauer, J. C.; Sessolo, M.; Bolink, H. J.; Banerji, N. Origin of the Enhanced Photoluminescence Quantum Yield in MAPbBr₃ Perovskite with Reduced Crystal Size. *ACS Energy Lett.* **2018**, *3*, 1458–1466.
- (114) Chan, W. L.; Tritsch, J. R.; Zhu, X. Y. Harvesting Singlet Fission for Solar Energy Conversion: One- Versus Two-Electron Transfer from the Quantum Mechanical Superposition. *J. Am. Chem. Soc.* **2012**, *134*, 18295–18302.
- (115) Gray, H. B.; Winkler, J. R. Hole Hopping through Tyrosine/Tryptophan Chains Protects Proteins from Oxidative Damage. *Proc. Natl. Acad. Sci. U. S. A.* **2015**, *112*, 10920–10925.
- (116) Cailliez, F.; Müller, P.; Gallois, M.; De La Lande, A. ATP Binding and Aspartate Protonation Enhance Photoinduced Electron Transfer in Plant Cryptochrome. *J. Am. Chem. Soc.* **2014**, *136*, 12974–12986.
- (117) Teo, R. D.; Rousseau, B. J. G.; Smithwick, E. R.; Di Felice, R.; Beratan, D. N.; Migliore, A. Charge Transfer between [4Fe4S] Proteins and DNA Is Unidirectional: Implications for Biomolecular Signaling. *Chem* **2019**, *5*, 122–137.
- (118) Teo, R. D.; Wang, R.; Smithwick, E. R.; Migliore, A.; Therien, M. J.; Beratan, D. N. Mapping Hole Hopping Escape Routes in Proteins. *Proc. Natl. Acad. Sci. U. S. A.* **2019**, *116*, 15811–15816.
- (119) Bertini G, Gray HB, Gray H, Valentine JS, Stiefel EI, S. E. *Biological Inorganic*

Chemistry: Structure and Reactivity; 2007.

- (120) Beratan, D. N. Multiple Hops Move Electrons from Bacteria to Rocks. *Proc. Natl. Acad. Sci. U. S. A.* **2021**, *118*, e2115620118.
- (121) Lambert, C.; Nöll, G.; Schelter, J. Bridge-Mediated Hopping or Superexchange Electron-Transfer Processes in Bis(Triarylamine) Systems. *Nat. Mater.* **2002**, *1*, 69–73.
- (122) Zhang, Y.; Liu, C.; Balaeff, A.; Skourtis, S. S.; Beratan, D. N. Biological Charge Transfer via Flickering Resonance. *Proc. Natl. Acad. Sci. U. S. A.* **2014**, *111*, 10049–10054.
- (123) Beratan, D. N.; Waldeck, D. H. Hot Holes Break the Speed Limit. *Nat. Chem.* **2016**, *8*, 992–993.
- (124) Beratan, D. N.; Liu, C.; Migliore, A.; Polizzi, N. F.; Skourtis, S. S.; Zhang, P.; Zhang, Y. Charge Transfer in Dynamical Biosystems, or the Treachery of (Static) Images. *Acc. Chem. Res.* **2015**, *48*, 474–481.
- (125) Chowdhury, S. N.; Zhang, P.; Beratan, D. N. Interference between Molecular and Photon Field-Mediated Electron Transfer Coupling Pathways in Cavities. *J. Phys. Chem. Lett.* **2022**, *13*, 9822–9828.
- (126) Beratan, D. N.; Onuchic, J. N.; Hopfield, J. J. Electron Tunneling through Covalent and Noncovalent Pathways in Proteins. *J. Chem. Phys.* **1998**, *86*, 4488.
- (127) Balabin, I. A.; Onuchic, J. N. Dynamically Controlled Protein Tunneling Paths in Photosynthetic Reaction Centers. *Science* **2000**, *290*, 114–117.
- (128) Beratan, D. N.; Skourtis, S. S.; Balabin, I. A.; Balaeff, A.; Keinan, S.; Venkatramani, R.; Xiao, D. Steering Electrons on Moving Pathways. *Acc. Chem. Res.* **2009**, *42*, 1669–1678.
- (129) Prytkova, T. R.; Kurnikov, I. V.; Beratan, D. N. Coupling Coherence Distinguishes Structure Sensitivity in Protein Electron Transfer. *Science* **2007**, *315*, 622–625.
- (130) Ben-Moshe, V.; Nitzan, A.; Skourtis, S. S.; Beratan, D. N. Steady-State Theory of Current Transfer. *J. Phys. Chem. C* **2010**, *114*, 8005–8013.
- (131) Skourtis, S. S.; Beratan, D. N.; Naaman, R.; Nitzan, A.; Waldeck, D. H. Chiral Control of Electron Transmission through Molecules. *Phys. Rev. Lett.* **2008**, *101*.

- (132) Skourtis, S.; Nitzan, A. Effects of Initial State Preparation on the Distance Dependence of Electron Transfer through Molecular Bridges and Wires. *J. Chem. Phys.* **2003**, *119*, 6271.
- (133) Zhu, X. Y. Electron Transfer at Molecule-Metal Interfaces: A Two-Photon Photoemission Study. *Annu. Rev. Phys. Chem.* **2002**, *53*, 221–247.
- (134) Scholes, G. D.; Fleming, G. R.; Olaya-Castro, A.; Van Grondelle, R. Lessons from Nature about Solar Light Harvesting. *Nature Chemistry*. 2011, pp 763–774.
- (135) Bakulin, A. A.; Rao, A.; Pavelyev, V. G.; Van Loosdrecht, P. H. M.; Pshenichnikov, M. S.; Niedzialek, D.; Cornil, J.; Beljonne, D.; Friend, R. H. The Role of Driving Energy and Delocalized States for Charge Separation in Organic Semiconductors. *Science* **2012**, *335*, 1340–1344.
- (136) Scholes, G. D.; Fleming, G. R.; Chen, L. X.; Aspuru-Guzik, A.; Buchleitner, A.; Coker, D. F.; Engel, G. S.; Van Grondelle, R.; Ishizaki, A.; Jonas, D. M.; Lundeen, J. S.; McCusker, J. K.; Mukamel, S.; Ogilvie, J. P.; Olaya-Castro, A.; Ratner, M. A.; Spano, F. C.; Whaley, K. B.; Zhu, X. Using Coherence to Enhance Function in Chemical and Biophysical Systems. *Nature*. 2017, pp 647–656.
- (137) Pineider, F.; De Julián Fernández, C.; Videtta, V.; Carlino, E.; Al Hourani, A.; Wilhelm, F.; Rogalev, A.; Cozzoli, P. D.; Ghigna, P.; Sangregorio, C. Spin-Polarization Transfer in Colloidal Magnetic-Plasmonic Au/Iron Oxide Hetero-Nanocrystals. *ACS Nano* **2013**, *7*, 857–866.
- (138) Tang, C. W. Two-Layer Organic Photovoltaic Cell. *Appl. Phys. Lett.* **1986**, *48*, 183–185.
- (139) Li, G.; Zhu, R.; Yang, Y. Polymer Solar Cells. *Nature Photonics*. 2012, pp 153–161.
- (140) Yao, H.; Ye, L.; Zhang, H.; Li, S.; Zhang, S.; Hou, J. Molecular Design of Benzodithiophene-Based Organic Photovoltaic Materials. *Chemical Reviews*. 2016, pp 7397–7457.
- (141) Ray, K.; Ananthavel, S. P.; Waldeck, D. H.; Naaman, R. Asymmetric Scattering of Polarized Electrons by Organized Organic Films of Chiral Molecules. *Science* **1999**, *283*, 814–816.
- (142) Chen, S. H.; Katsis, D.; Schmid, A. W.; Mastrangelo, J. C.; Tsutsui, T.; Blanton, T. N. Circularly Polarized Light Generated by Photoexcitation of Luminophores in Glassy Liquid-Crystal Films. *Nature* **1999**, *397*, 506–508.

- (143) Li, W.; Coppens, Z. J.; Besteiro, L. V.; Wang, W.; Govorov, A. O.; Valentine, J. Circularly Polarized Light Detection with Hot Electrons in Chiral Plasmonic Metamaterials. *Nat. Commun.* **2015**, *6*.
- (144) Naaman, R.; Waldeck, D. H. Spintronics and Chirality: Spin Selectivity in Electron Transport Through Chiral Molecules. *Annu. Rev. Phys. Chem.* **2015**, *66*, 263–281.
- (145) Yang, Y.; Da Costa, R. C.; Fuchter, M. J.; Campbell, A. J. Circularly Polarized Light Detection by a Chiral Organic Semiconductor Transistor. *Nat. Photonics* **2013**, *7*, 634–638.
- (146) Aiello, C. D.; Abendroth, J. M.; Abbas, M.; Afanasev, A.; Agarwal, S.; Banerjee, A. S.; Beratan, D. N.; Belling, J. N.; Berche, B.; Botana, A.; Caram, J. R.; Celardo, G. L.; Cuniberti, G.; Garcia-Etxarri, A.; Dianat, A.; Diez-Perez, I.; Guo, Y.; Gutierrez, R.; Herrmann, C.; Hihath, J.; Kale, S.; Kurian, P.; Lai, Y. C.; Liu, T.; Lopez, A.; Medina, E.; Mujica, V.; Naaman, R.; Noormandipour, M.; Palma, J. L.; Paltiel, Y.; Petuskey, W.; Ribeiro-Silva, J. C.; Saenz, J. J.; Santos, E. J. G.; Solyanik-Gorgone, M.; Sorger, V. J.; Stemer, D. M.; Ugalde, J. M.; Valdes-Curiel, A.; Varela, S.; Waldeck, D. H.; Wasielewski, M. R.; Weiss, P. S.; Zacharias, H.; Wang, Q. H. A Chirality-Based Quantum Leap. *ACS Nano* **2022**, *16*, 4989–5035.
- (147) Beratan, D. N.; Naaman, R.; Waldeck, D. H. Charge and Spin Transport through Nucleic Acids. *Curr. Opin. Electrochem.* **2017**, *4*, 175–181.
- (148) Shao, Y.; Gan, Z.; Epifanovsky, E.; Gilbert, A. T. B.; Wormit, M.; Kussmann, J.; Lange, A. W.; Behn, A.; Deng, J.; Feng, X.; Ghosh, D.; Goldey, M.; Horn, P. R.; Jacobson, L. D.; Kaliman, I.; Khaliullin, R. Z.; Kus, T.; Landau, A.; Liu, J.; Proynov, E. I.; Rhee, Y. M.; Richard, R. M.; Rohrdanz, M. A.; Steele, R. P.; Sundstrom, E. J.; Woodcock, H. L.; Zimmerman, P. M.; Zuev, D.; Albrecht, B.; Alguire, E.; Austin, B.; Beran, G. J. O.; Bernard, Y. A.; Berquist, E.; Brandhorst, K.; Bravaya, K. B.; Brown, S. T.; Casanova, D.; Chang, C. M.; Chen, Y.; Chien, S. H.; Closser, K. D.; Crittenden, D. L.; Diedenhofen, M.; Distasio, R. A.; Do, H.; Dutoi, A. D.; Edgar, R. G.; Fatehi, S.; Fusti-Molnar, L.; Ghysels, A.; Golubeva-Zadorozhnaya, A.; Gomes, J.; Hanson-Heine, M. W. D.; Harbach, P. H. P.; Hauser, A. W.; Hohenstein, E. G.; Holden, Z. C.; Jagau, T. C.; Ji, H.; Kaduk, B.; Khistyayev, K.; Kim, J.; Kim, J.; King, R. A.; Klunzinger, P.; Kosenkov, D.; Kowalczyk, T.; Krauter, C. M.; Lao, K. U.; Laurent, A. D.; Lawler, K. V.; Levchenko, S. V.; Lin, C. Y.; Liu, F.; Livshits, E.; Lochan, R. C.; Luenser, A.; Manohar, P.; Manzer, S. F.; Mao, S. P.; Mardirossian, N.; Marenich, A. V.; Maurer, S. A.; Mayhall, N. J.; Neuscamman, E.; Oana, C. M.; Olivares-Amaya, R.; Oneill, D. P.; Parkhill, J. A.; Perrine, T. M.; Peverati, R.; Prociuk, A.; Rehn, D. R.; Rosta, E.; Russ, N. J.; Sharada, S. M.; Sharma, S.; Small, D.

W.; Sodt, A.; Stein, T.; Stück, D.; Su, Y. C.; Thom, A. J. W.; Tsuchimochi, T.; Vanovschi, V.; Vogt, L.; Vydrov, O.; Wang, T.; Watson, M. A.; Wenzel, J.; White, A.; Williams, C. F.; Yang, J.; Yeganeh, S.; Yost, S. R.; You, Z. Q.; Zhang, I. Y.; Zhang, X.; Zhao, Y.; Brooks, B. R.; Chan, G. K. L.; Chipman, D. M.; Cramer, C. J.; Goddard, W. A.; Gordon, M. S.; Hehre, W. J.; Klamt, A.; Schaefer, H. F.; Schmidt, M. W.; Sherrill, C. D.; Truhlar, D. G.; Warshel, A.; Xu, X.; Aspuru-Guzik, A.; Baer, R.; Bell, A. T.; Besley, N. A.; Chai, J. Da; Dreuw, A.; Dunietz, B. D.; Furlani, T. R.; Gwaltney, S. R.; Hsu, C. P.; Jung, Y.; Kong, J.; Lambrecht, D. S.; Liang, W.; Ochsenfeld, C.; Rassolov, V. A.; Slipchenko, L. V.; Subotnik, J. E.; Van Voorhis, T.; Herbert, J. M.; Krylov, A. I.; Gill, P. M. W.; Head-Gordon, M. Advances in Molecular Quantum Chemistry Contained in the Q-Chem 4 Program Package. <https://doi.org/10.1080/00268976.2014.952696> **2014**, *113*, 184–215.

- (149) Zheng, J.; Kang, Y. K.; Therien, M. J.; Beratan, D. N. Generalized Mulliken-Hush Analysis of Electronic Coupling Interactions in Compressed π -Stacked Porphyrin-Bridge-Quinone Systems. **2005**.
- (150) Chen, H.-C.; Hsu, C.-P. Ab Initio Characterization of Electron Transfer Coupling in Photoinduced Systems: Generalized Mulliken-Hush with Configuration-Interaction Singles. **2005**.
- (151) Prezhdo, O. V.; Rossky, P. J. Relationship between Quantum Decoherence Times and Solvation Dynamics in Condensed Phase Chemical Systems. *Phys. Rev. Lett.* **1998**, *81*, 5294.
- (152) Gu, B.; Franco, I. Generalized Theory for the Timescale of Molecular Electronic Decoherence in the Condensed Phase. *J. Phys. Chem. Lett.* **2018**, *9*, 773–778.
- (153) Lindblad, G. Mathematical Physics On the Generators of Quantum Dynamical Semigroups. *Commun. math. Phys.* **1976**, *48*, 119–130.
- (154) Weiss, E. A.; Katz, G.; Goldsmith, R. H.; Wasielewski, M. R.; Ratner, M. A.; Kosloff, R.; Nitzan, A. Electron Transfer Mechanism and the Locality of the System-Bath Interaction: A Comparison of Local, Semilocal, and Pure Dephasing Models. *J. Chem. Phys.* **2006**, *124*, 64504.
- (155) Saalfrank, P.; Baer, R.; Kosloff, R. Density Matrix Description of Laser-Induced Hot Electron Mediated Photodesorption of NO from Pt(111). *Chem. Phys. Lett.* **1994**, *230*, 463–472.
- (156) Wolfram Research, I. Mathematica. 2021.

- (157) Brown, K. E.; Salamant, W. A.; Shoer, L. E.; Young, R. M.; Wasielewski, M. R. Direct Observation of Ultrafast Excimer Formation in Covalent Perylenediimide Dimers Using Near-Infrared Transient Absorption Spectroscopy. **2014**.
- (158) BenDaniel, D. J.; Duke, C. B. Space-Charge Effects on Electron Tunneling. *Phys. Rev.* **1966**, *152*, 683–692.
- (159) Harrison, W. A. Tunneling from an Independent-Particle Point of View. *Phys. Rev.* **1961**, *123*, 85–89.

Biography

Zhendian Zhang obtained B.S. in applied chemistry from Shanghai Jiao Tong University in 2017. At Shanghai Jiao Tong University, he was mentored by Prof. Huai Sun with research interest in molecular dynamics simulation of inorganic materials. He started his PhD study in chemistry at Duke University in 2017 under mentorship of Prof. David Beratan. His research focused on the modeling of quantum dot system and electron transfer dynamics. A list of his publication is as follows:

1. Zhang, Z., Jin, Y., Zhang, P., Beratan, D.N.,. Control of Photoinduced Electron Transfer Yield with Polarized Light, in preparation
2. Zhang, Z., Zhang P., Waldeck, D. H., Beratan, D.N.. Size Determines the balance of Through-bond and Through-solvent Coupling Between Linked Quantum Dots, in preparation.
3. Jin, T., Zhang, Z., Kaledin, A., Xu, Z., Liu, Y., Zhang, P., Beratan, D.N., Lian T., On the Coupling Strength of Core-shell Quantum Dot Sensitized Triplet Energy Transfer, in preparation.
4. Sun, K., Fang, C., Kang, M., Zhang, Z., Zhang, P., Beratan, D. N., ... & Kim, J. (2023). Quantum simulation of polarized light-induced electron transfer with a trapped-ion qutrit system. *The Journal of Physical Chemistry Letters*, 14, 6071-6077.
5. Georgieva, Z. N., Zhang, Z., Zhang, P., Bloom, B. P., Beratan, D. N., & Waldeck, D. H. (2022). Ligand coverage and exciton delocalization control chiral imprinting in perovskite nanoplatelets. *The Journal of Physical Chemistry C*, 126(37), 15986-15995.
6. Ma, J., Zhang, Z., Xiang, Y., Cao, F., & Sun, H. (2017). On the prediction of transport properties of ionic liquid using 1-n-butylmethylpyridinium tetrafluoroborate as an example. *Molecular Simulation*, 43(18), 1502-1512.